VLÁKNA A TEXTIL

FIBRES AND TEXTILES

4

Volume **30**
October
2023

TECHNICAL UNIVERSITY OF LIBEREC

STU FCHPT

Trenčianska univerzita Alexandra Dubčeka v Trenčíne, Fakulta priemyselných technológií v Púchove

VUTCH
RESEARCH INSTITUTE OF TEXTILE CHEMISTRY
VÝSKUMNÝ ÚSTAV TEXTILNEJ CHÉMIE

CHEMOSVIT FIBROCHEM

VÚCHV

ZSVTS

VLÁKNA A TEXTIL
http://www.vat.ft.tul.cz

VLÁKNA A TEXTIL

Volume 30, Issue 4, October 2023

CONTENT

PROPERTIES OF PARACHUTE FABRICS FROM POLYAMIDE AND POLYESTER MATERIALS

MILITKÝ, JIŘÍ[1*]; WIENER, JAKUB[1]; KŘEMENÁKOVÁ, DANA[1] AND MISHRA, RAJESH[2]

[1]   Technical University of Liberec, Faculty of Textile Engineering, Studentska 2, 461 17, Liberec, Czech Republic
[2]   Czech University of Live Sciences Prague, Faculty of Engineering, Kamýcká 129, 165 00, Praha, Czech Republic

ABSTRACT

Traditional parachute fabrics are composed from PA 66 (nylon type) multifilament yarns. They are resistant against high frequency repeat deformation but they are able to absorb water which is not optimal for use in different climatic conditions. Challenge is to create parachute fabrics made of PES multifilament yarns which are more versatile. Main aim of this work is to investigate influence of parachute fabric composition and construction characteristics on real end use properties. The relationships based on the prediction of bulk densities were used to calculate the volume porosity. The morphology of the parachute fabrics was evaluated using scanning electron microscopy. Mechanical and dynamic mechanical properties of parachute fabric Ortex made from multifilament PA 66 and PES yarns by Sky Paragliders company are compared.

KEYWORDS

Parachute fabrics; Morphology; Porosity; Mechanical properties; Calendering.

INTRODUCTION

Parachute textiles are during use exposed to a series of rapid events during the opening of the parachute and handling during descent, which can lead to their frictional and thermal damages which at limit cause to catastrophic failure [1- 4]. In addition to standard textile tests, which are standardized, it is also necessary to develop or to modify tests that better characterize dynamic manifestations, surface structure and resistance to air flow in conditions simulating real conditions during use [5- 6]. The construction of fabrics largely affects the behavior of parachutes, especially with regard to their porosity and resistance to thermal shocks [7].

One of main challenge is the replacement of polyamide (PA 66) multifilament by polyester (PES) one. The problem is that no suitable company was found that produces polyester multifilament of the necessary parameters for other than polyethylene terephthalate (PET) polymers. The produced PET multifilament is therefore not primarily intended for parachute textiles.

A comprehensive evaluation of the structure and properties of polyamide fibers [8] and polyester fibers [9] was published e.g. in the chapters of the book "Handbook of Properties of Textile and Technical Fibers". PA 66 fibers generally have the following advantages compared to PET fibers:

-   higher resistance to cyclic stress (better recovery),
-   high flexibility (lower stiffness - modulus),
-   higher toughness (energy required to break),
-   high abrasion resistance,
-   lower tendency to accumulate electrostatic charge (higher electrical conductivity),
-   lower specific weight (but somewhat larger volume with the same geometry).

These advantages were the main reason for using PA 66 fibers for parachute fabrics. On the other hand, PA 66 are more sensitive to higher humidity (water content 4-5% under standard conditions), have lower resistance to torsion and less resistance to UV radiation than PET fibers. Also, the glass transition temperature and mechanical properties at elevated temperatures are lower. The problem is that the mechanical properties of the fibers vary over a relatively wide range depending on the length of the macromolecular chains, but especially on the conditions of fibers drawing and heat treatment. It is therefore difficult to evaluate the differences between parachute fabrics produced from multifilament prepared specifically for industrial parachute fabrics (PA 66) and parachute fabrics from multifilament produced primarily for other applications (PET).

The research activities described in this contribution are mainly focused on comparing and modifying the properties of parachute textiles made of PA 66

---
[*] **Corresponding author:** Militký J., e-mail: *jiri.militky@tul.cz*

Figure 1. Sample 1: (a) front side, (b) reverse side, (c) cross section (magnification 500x).

Figure 2. Sample 2: (a) front side, (b) reverse side, (c) cross section (magnification 500x).
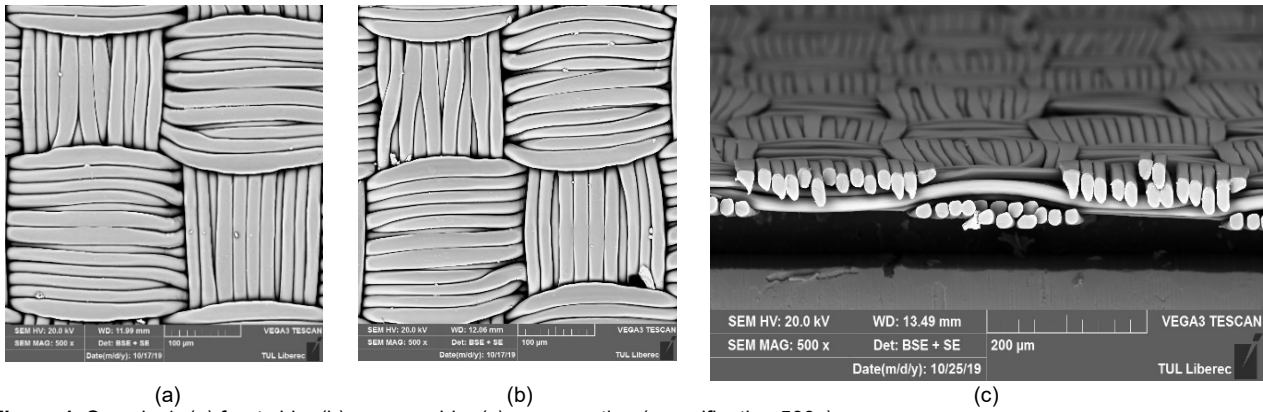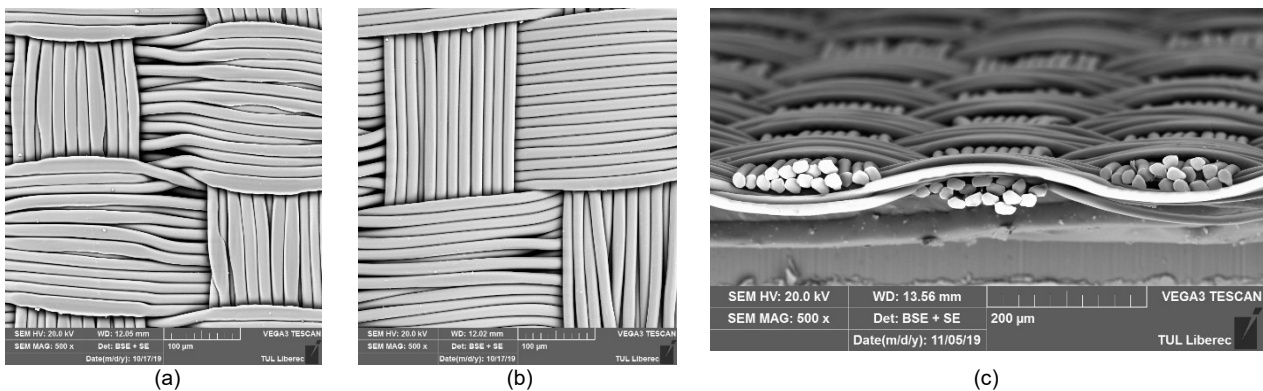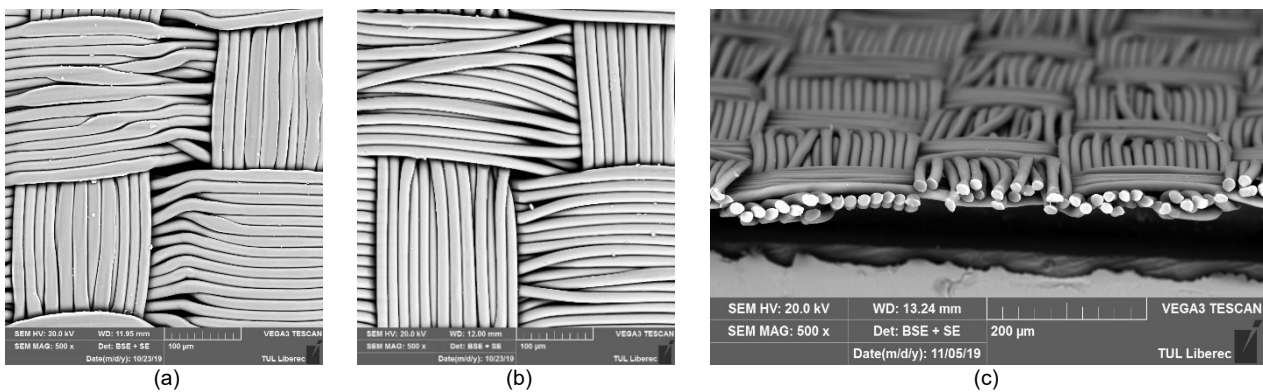

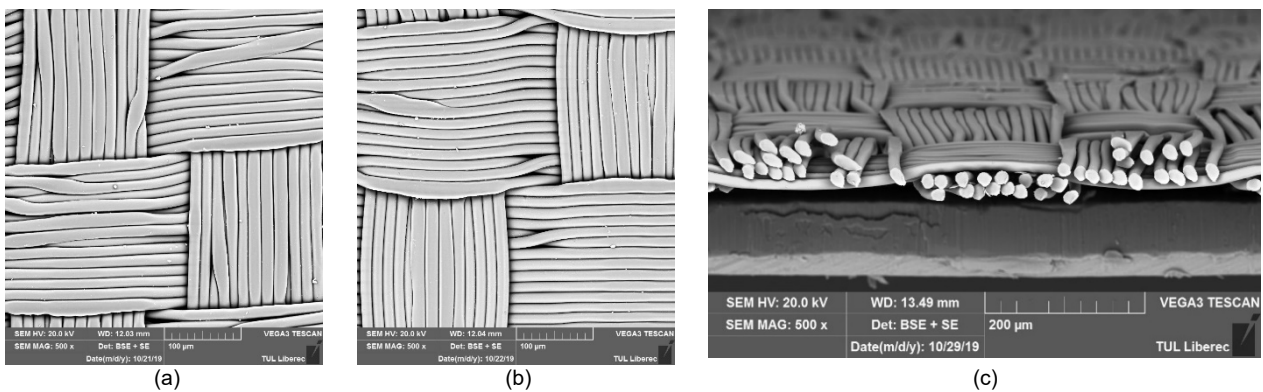**Figure 3.** Sample 3: (a) front side, (b) reverse side, (c) cross section (magnification 500x).

Figure 4. Sample 4: (a) front side, (b) reverse side, (c) cross section (magnification 500x).

Table 1. List of Ortex parachute fabrics (Sky paragliders).

Sample	Composition	Treatment	Ends/cm	Picks/cm
1	PA 66 33dtex/14 fibers	Final fabric	31	30
2	PES 33dtex/16 fibers	Unfinished fabric	45	43
3	PES 33dtex/ 16 fibers	1st calendering (185 ºC, 24m/min, 2500 N)	43	42
4	PES 33dtex/16 fibers	2nd calendering (185 ºC, 24 m/min, 2500 N)	42	41

Table 2. Morphology of parachute fabrics.

Sample	Areal mass [gm^{-2}]	Thickness [mm]	Density [kgm^{-3}]	Porosity [-]
1	39.2	0.05	784	0.31
2	34.9	0.05	698	0.49
3	34.9	0.05	698	0.49
4	34.7	0.05	694	0.49

(sample 1) and polyester – PET (sample 2: raw, sample 3: after single calendering and sample 4: after two times calendering). The construction of these textiles was examined in more detail.

PARACHUTE FABRICS GEOMETRY AND VOLUMETRIC POROSITY

Ortex parachute fabrics made of PES and PAD multifils were supplied by company Sky Paragliders, see Tab. 1.

Microscopic images of fabric samples were prepared on a Vega Tescan electron microscope. From the microscopic images, the Ripstop weave was identified. Selected images of parachute fabric samples no. 1 to 4 are shown in Fig. 1 to 4.

It is visible that PA 66 fabric was calendered during preparation because the surface filaments are flat. Calendering of PET filaments had very low effect on fabrics surface geometry.

The thickness and areal weight (gsm) of the parachute fabrics were measured and their density (the ratio of areal weight to thickness) was calculated. The ratio of the density of the parachute fabric to the density of the fibers from which it is made is equal to the volume fraction of the fibers in the fabric. The PA 66 fiber density of 1130 kgm-3 and the PES fiber density of 1360 kgm-3 were used for the calculation. The volume porosity of the parachute fabrics was calculated as one minus volume traction. The results are shown in Tab. 2.

According to volume porosity, samples can be divided into 2 groups, sample no. 1from PA 66 has a significantly lower porosity value from 0.31. Samples from PET have porosity value of 0.49 independently of the first and second calendering. In sample from PA 66 are the fibers distributed relatively evenly at the binding points. In the case of PES fabrics, even after the second calendering, it was not possible to evenly distribute the weft fibers, which were apparently clogged under a lower tension. Air pores have been created in the edges of the attachment points, which increase the porosity of PES fabrics.

It was found that volume porosity correlates well with air permeability of parachute fabrics [4].

MECHANICAL CHARACTERISTICS OF PARACHUTE FABRICS

The mechanical properties of these fabrics were evaluated in terms of tensile, bending, tear, bursting strength and dynamical mechanical analysis. Further, the drape coefficient was also evaluated.

Tensile test

Tensile properties of all fabric samples in warp and weft direction were measured on a TIRA 2300 (LaborTech s.r.o., Opava,Czech Republic) universal testing machine. This test was performed according to standard EN ISO 13934-1 (sample size 5x3 cm rate of deformation 100 mm/min). The tensile strength and elongation at break were measured both in warp and weft directions. The results are given in Tab. 3 and in Fig. 5. The values are average of 5 measurements. In sequel errors bars are equal to end points of 95% confidence intervals.

The breaking strength is higher for sample of PA 66 compared to the PES samples. There is a slight increase of PES fabric strength after 1st calendering. A slight increase in strength after 1st calendering can be due to fusing of filaments which might cause an increase in cohesion and thus slightly higher load bearing capacity. However, after 2nd calendering again the strength decreases. This may be attributed to the degradation/weakening of PES filaments under the thermal treatment and calendering conditions. Overall it can be observed that the tensile strength of PES original fabric as well as calendered fabric is lower than the PA 66 fabric. Warp way strength is always higher than weft way strength due to consolidation of warp yarns and higher weaving tension, which might have caused better orientation of filaments and thus improved mechanical performance. Breaking elongation are given in Fig. 5(b).

Table 3. Tensile properties.

Samples	Breaking strength [N]				Breaking elongation [%]			
	warp		weft		warp		weft	
	Mean	SD*)	Mean	SD*)	Mean	SD*)	Mean	SD*)
1	435.54	19.43	421.64	21.23	26.55	1.19	28.71	0.89
2	422.85	17.23	416.23	18.30	23.63	0.87	26.20	1.02
3	426.51	16.83	419.28	18.33	22.11	1.32	23.23	1.12
4	421.55	17.92	417.82	15.32	23.42	1.09	22.39	1.32

*) SD is abbreviation of standard deviation

(a)

(b)
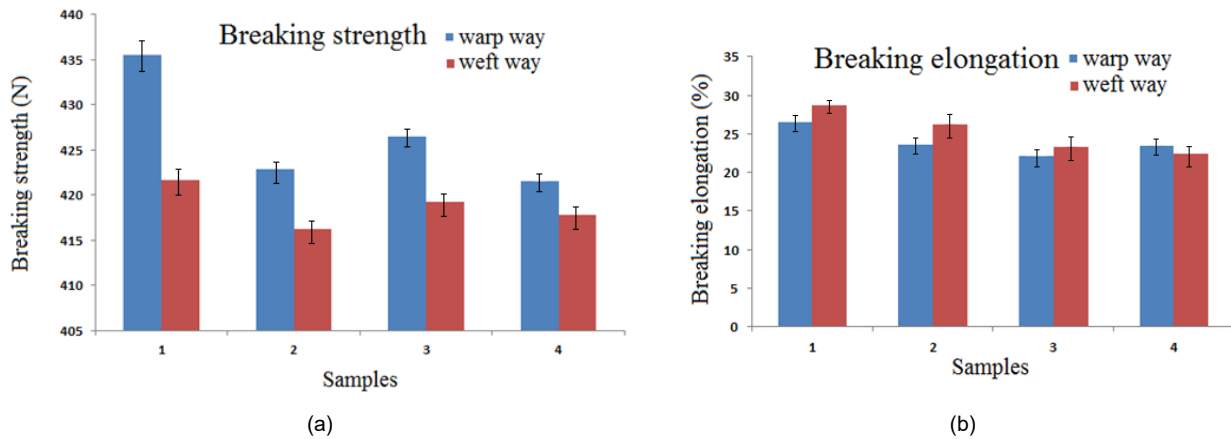
Figure 5. (a) fabric breaking strength [N], (b) fabric breaking elongation [%].

Table 4. Tearing strength.

Samples	Tearing strength [N]			
	warp		weft	
	Mean	SD	Mean	SD
1	32.37	1.37	33.63	1.49
2	26.22	1.27	25.72	1.42
3	22.26	1.32	25.06	1.34
4	23.42	1.09	25.33	1.14

The breaking elongation for PA 66 fabric is higher than PES fabric. The thermal treatment during calendering causes fusing and increased cohesion between filaments, which restricts the tensile deformation. Moreover, the weakening of individual filaments leads to a lower elongation at break. Elongation in the weft direction is slightly higher than elongation in the warp direction. It is due to lower weft tension and higher residual elongation, which is retained in the weft filaments as compared to the warp way filaments.

Tear test

A parachute fabric tears when it is snagged by a sharp object and the immediate small puncture is converted into a long rip by what may be a very small extra effort. It is probably the most common type of strength failure of parachute fabrics in use. It is particularly important in industrial fabrics that are exposed to rough handling in use such as tents and sacks and those where propagation of a tear would be catastrophic such as parachutes. For measurement of tear strength, EN ISO 13937-2 standard is used (rate of deformation 100 mm/min). The tear strength in warp and weft direction is given

in Tab. 4. The values are average of 5 measurements.

The tearing strength is a measure of the inter-yarn cohesiveness and friction between adjacent yarns. Tearing warp way needs to break the weft yarns and split them from forming bundles. Similarly tearing in the weft direction involves breakage and rupture of warp filaments. It is observed that the weft way tear strength is higher than warp way tear strength. It is due to relatively stronger warp yarns as compared to weft yarns as well as higher wrap sett compared to weft sett. The PA 66 sample shows higher tearing strength, which is mainly due to stronger filaments as compared to PES filaments. Moreover, the inter-fiber and inter-yarn frictional forces are higher. The calendering rather weakens the PES filaments in the weft and there is slight decrease in the tear strength in warp direction. Weft way tear strength remains almost unchanged.

Bursting strength test

Bursting strength is an alternative method of measuring strength in which the material is stressed in all directions at the same time and is therefore more

Table 5. Bursting strength.

Samples	Bursting strength [kPa]	
	Mean	SD
1	329.12	17.20
2	330.72	13.67
3	326.24	13.23
4	322.30	16.53

Table 6. Drape coefficient.

Samples	Drape coefficient
1	32.37
2	33.79
3	32.82
4	33.19

suitable for parachute materials. These are fabrics, which are simultaneously stressed in all directions during service where it may be important to stress them in a realistic manner. The EN ISO 13938-2 standard is used for measurement of bursting strength. The fabric bursting strength is given in Tab. 5. The values are average of 5 measurements.

The bursting strength shows no significant difference. There is a slight decrease in bursting strength after calendering of PES fabric which may be due to thermal degradation of the filaments.

Drape measurement

Fabric drape can be defined as a description of the deformation of a fabric produced by gravity when only part of it is directly supported. The drape ability of a fabric is quantified into a dimensionless value called 'drape coefficient', which is defined as the percentage of the area from an annular ring of the fabric covered by a vertical projection of the draped fabric. The ISO 9073-9:2008 standard is followed for such

measurements. Results of drape coefficient calculation are shown in Tab. 6.

There is no significant difference in drape ability of the fabrics. However, the drape coefficient of PES parachute fabrics is slightly higher than the PA 66 fabric. It can be due to higher stiffness of fabrics resulting from stiffer yarns and higher fabric sett. The yarns of PES could be stiffer as they are composed from 16 filaments as compared to 14 filaments in case of PAD yarns. Moreover, the PES fabrics have much higher sett in both warp and weft direction which increases the fabric stiffness. The calendaring does not change the drape too much.

Bending rigidity

The bending rigidity is related to the tensile modulus for a simple body, as in the case of a single fiber; however, this relationship is not so straightforward in the case of a fabric. To measure the fabric bending stiffness, the cantilever method is widely used in practice. The fabric bending length is measured by using cantilever stiffness measurement equipment. The bending rigidity was measured by the standard ASTM test method D-1388.

Bending rigidity or stiffness depends on the rigidity of yarns as well as the fabric sett. The results of stiffness measured in warp and weft direction are given in Tab. 7 and Fig. 6.

The bending rigidity of fabric is dependent on fiber/filament diameter, yarn fineness, number of filaments, the inter-fiber and inter-yarn friction etc. Friction between individual filaments in a yarn is caused by different mechanisms. The filaments on the outer perimeter of the yarn interact with filaments

Table 7. Bending rigidity of fabrics.

Samples	Bending rigidity (N.m^2) x 10^{-6}			
	warp		weft	
	Mean	SD	Mean	SD
1	10.62	0.63	10.53	0.45
2	10.83	0.67	10.78	0.52
3	10.97	0.83	10.88	0.66
4	10.84	0.72	10.68	0.62
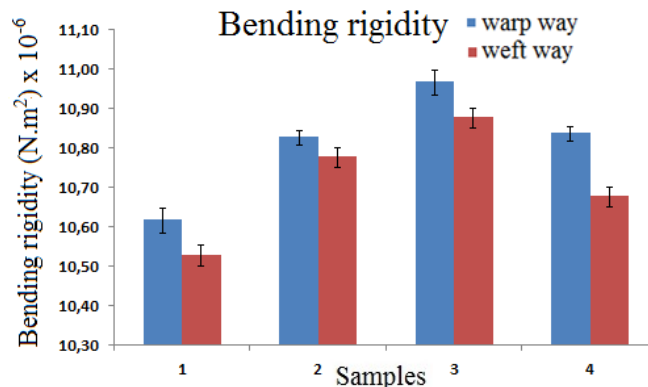
Figure 6. Fabric bending rigidity.
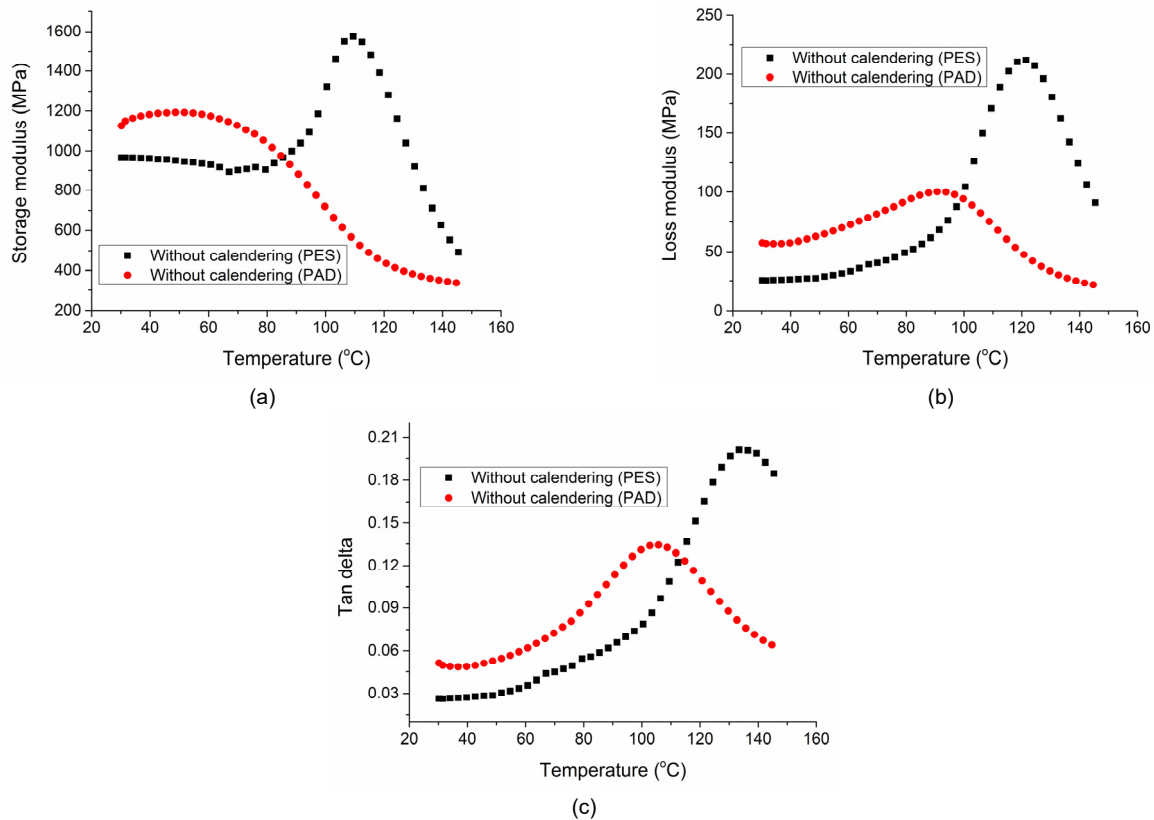
Figure 7. Dynamic mechanical properties of polyester and polyamide parachute fabrics: (a) storage modulus, (b) loss modulus, (c) tan delta.

from other yarns due to undulation in fabrics. Filaments within the yarns are often entangled because of fiber migration and length differences due to deformations. A fiber sizing is often applied during production to protect the yarn material and/or improve fiber-matrix bonding. Another factor plays a role in the intra- as well as inter-yarn friction behavior. The effects mentioned above all have influence on the deflection behavior of yarns based on friction mechanisms.

It is clearly visible that warp way rigidity is higher than weft way bending rigidity as the warp yarns are stiffer and there is a higher sett in warp direction. The PES samples have higher rigidity as compared to the PA 66 fabric. It can be due to inherent higher rigidity of the PES filaments as compared to PA 66 filaments. There are higher number of filaments in each yarn thus causing increase in yarn bending rigidity. Further, the sett of the PES fabrics is much higher than the PA 66 fabric. Therefore, the bending stiffness is increased. After 1st calendering, there is probably stiffening and partial sticking of the PES filaments and thus a further increase in stiffness is observed. During 2nd calendering, there is a possibility of filament/fiber weakening which results in a deterioration of mechanical properties. It might cause a loss of rigidity as well. The deterioration of weft yarn seems more severe as compared to the warp yarn.

Dynamic mechanical analysis

The dynamic mechanical properties of PA 66 and PES parachute fabrics were measured in tensile mode using Q800 Dynamic mechanical thermal analysis (DMTA) instrument of TA instruments (New Castle DL, USA). The testing conditions were controlled in the temperature range of 30–150 °C, with a heating rate of 3 °C/min, at frequency of 1 Hz, preload of 0.01 N, amplitude of 15 µm, and force track of 125%. The test was carried out with gauge length and sample width of 30 mm and 10 mm respectively.

The effect of calendaring treatments on change in dynamic mechanical properties of was studied. The storage modulus results depicted the load bearing capacity whereas the tan delta results showed the damping properties of parachute fabrics (see Fig. 7). The PA 66 fabric showed higher storage modulus (i.e.1124 MPa) than the storage modulus of polyester fabric (i.e. 965 MPa) at 30 °C. This increase in storage modulus value can be attributed to the higher stiffness of polyamide fabric structure However, the storage modulus of polyamide fabric dropped at faster rate than polyester fabric with the increase in temperature. At 100 °C, the storage modulus of 713 MPa was observed in case of PA 66 fabric as compared to the storage modulus of 1300 MPa for PES fabric. The significant drop in storage modulus of PA 66 fabric was due to the softening of structure and easier movement of polymeric chains.
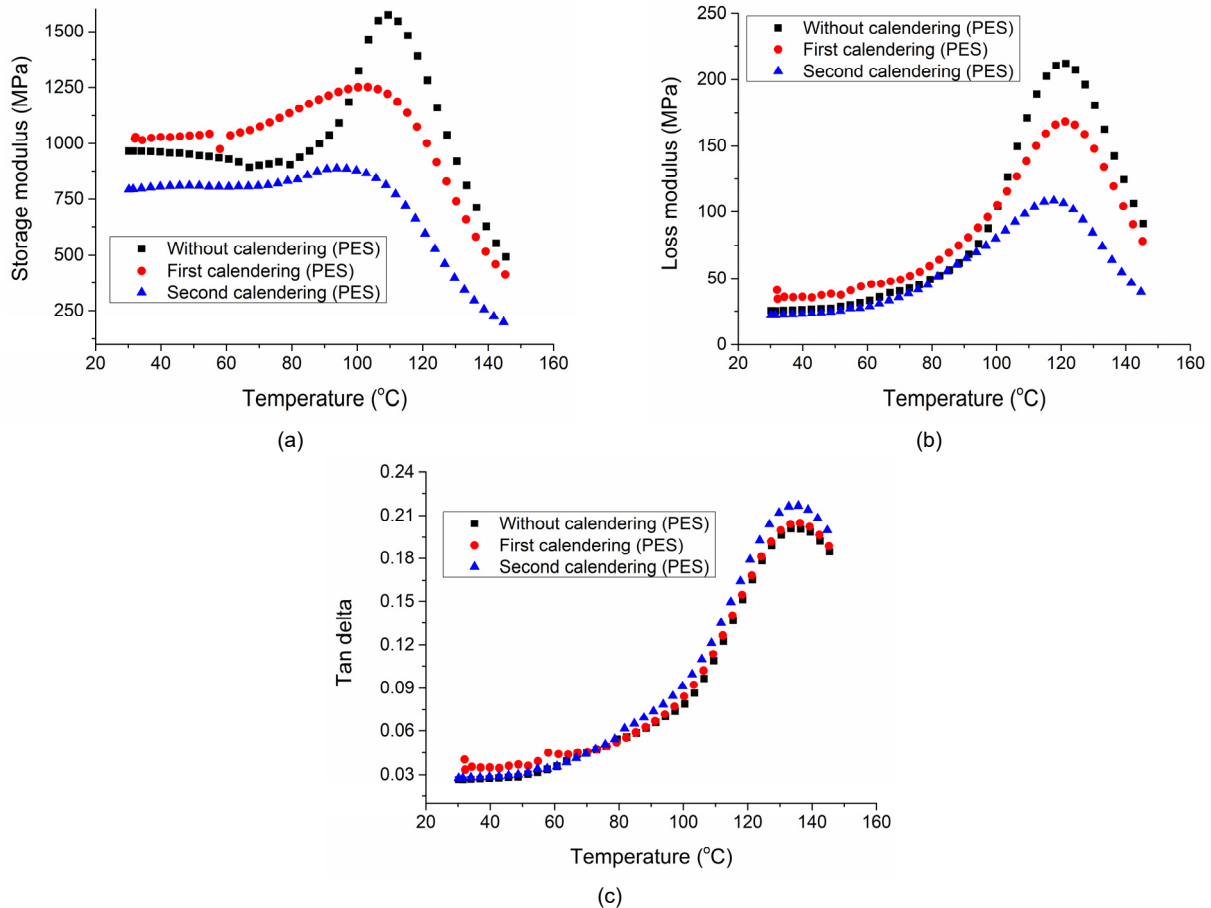
Figure 8. Effect of calendaring on dynamic mechanical properties of polyester parachute fabrics: (a) storage modulus, (b) loss modulus, (c) tan delta.

On the other hand, the relatively smaller drop in case of PES fabric was attributed to their restricted segmental motion at higher temperatures. The damping properties of the material give the balance between the elastic phase and viscous phase in a polymeric structure. The ratio of loss modulus to storage modulus is defined as mechanical loss factor or damping factor or tan delta. The damping factor expresses an ability of converting the mechanical energy into heat energy when the material is subjected to an external loading. It was observed that the PA 66 fabric has lower damping factor as compared to PES fabric, which indicates their increment of the loss of energy due to macromolecular friction. Furthermore, the tan delta peak of PES fabric was located at higher temperature (i.e. at 135 °C) as compared to the PA 66 fabric (i.e. at 103 °C).

The curves confirmed that all the properties of the parachute fabrics were greatly affected by calendering treatments across all temperature ranges (see Fig. 8). At 30 °C, the PES fabric with no calendaring treatment showed higher storage modulus (i.e. 965 MPa) than second calendared polyester fabrics (792 MPa). The marginal improvement in storage modulus was shown by first calendared PES fabric (1020 MPa) over non-

calendared fabric. This change in load bearing capacity under different calendaring actions is attributed to partial softening of polyester fabrics due to segmental mobility of polymeric chains. With further increase in temperature, the storage modulus of calendered PES fabrics was dropped heavily as compared to non-calendered PES fabrics. The storage moduli of 1135 MPa, 889 MPa and 498 MPa were depicted by PES fabrics of without calendaring, first calendaring and second calendaring actions respectively at 125 °C. The significant drop in storage modulus of polyester fabric at higher temperature was attributed to even higher segmental mobility of polymeric chains than observed at 30 °C. Furthermore, no significant change in damping factor was observed after the calendaring actions on the polyester fabrics.

CONCLUSION

It has been shown that when using PET multifilament of the same fineness and number of fibers as PA 66 multifilament, the PET multifilament has a smaller diameter, and the filaments diameter is also smaller. For these reasons, it is necessary to use a slightly higher level of PET fabric sett than the sett of PA 66 fabric. In calendered parachute fabrics, the multifilament fibers are usually spread evenly so that

the flattening is near to one. Due to the higher value of fiber density, PET multifilament fabric achieves slightly higher values of areal weight and total density than PA 66 multifilaments.

It was clearly shown that differences between parachute fabrics from PA 66 (especially prepared for parachutes) and PES (prepared for general use) are not very different. In many cases are common PES fabrics over special PA 66 fabrics. This is great challenge for preparation of special PES fabrics for parachutes with enhanced mechanical properties by use higher polymerization degree higher drawing ratio and proper thermal treatment [2]. It was confirmed that prototype PET fabric gets the similar morphology, mechanical properties and surface behavior than actual PA 66 parachute fabric

REFERENCES

1. Johari H., Desabrais K.J.: Stiffness scaling for solid cloth parachutes, Journal of Aircraft, 40(4), 2003, pp. 631-638. https://doi.org/10.2514/2.3166
2. Cockrell D.J.: The Aerodynamics of Parachutes, Cambridge: AGARD, 1987.
3. Ericksen R.H.., et al.: Deflection-force measurements and observations on Kevlar 29 parachute fabrics, Textile Research Journal, 62(11), 1992, pp. 628-638. https://doi.org/10.1177/004051759206201102
4. Shi Q., et al.: On the verification and validation of a spring fabric for modeling parachute inflation, Journal of Fluids and Structures, 58, 2015, pp. 20–39. https://doi.org/10.1016/j.jfluidstructs.2015.06.014
5. Kiryukhin S.M., Lazunina Yu.N.: Assessment of strength reliability of polyamide parachute fabrics, Fibre Chemistry, 46, 2014, pp. 56-58. https://doi.org/10.1007/s10692-014-9560-2
6. Citoglu F., Esi B.: Parachute fabric and its manufacturing process, International Journal of Science, Environment and Technology, 6(5), 2017, pp. 3214 – 3224.
7. Baker A., Swallow J. E.: Light transmission and air flow through nylon parachute fabrics, Journal of the Textile Institute Transactions, 47, 1956, T102-T109. https://doi.org/10.1080/19447027.1956.10750380
8. Militký J., Venkataraman M., Mishra R.: The chemistry, manufacture, and tensile behavior of polyamide fibers, In Bunsell A. R. ed.: Handbook of Properties of Textile and Technical Fibres, Elsevier, 2018.
9. Militký J.: Tensile failure of polyester fibers, In Bunsell A. R. ed.: Handbook of Properties of Textile and Technical Fibres, Elsevier, 2018.
10. Kaynak H.K., Babaarslan O.: Polyester microfilament woven fabrics, In Han-Yong J. ed.: Woven Fabrics, Rjeka, 2012.
11. Křemenáková, D. et al.: Air permeability of parachute fabrics, In Preparation.

This work is dedicated to prof. Izabella Krucińska from TU Lodz, who was not only a prominent scientific personality but also our close friend. A tribute to her memory.

STUDY THE SELF-CLEANING ABILITY OF ZNO CONTAINED COTTON FABRICS

DUY-NAM, PHAN[1*]; THI THAN THUONG, VU[1]; NGUYEN NHAT, TRINH[1], NGUYEN MINH[1], TUAN; CAO HONG, HA[2] AND MINH THANG, LE[2]

1   School of Textile – Leather and Fashion, Hanoi University of Science and Technology, Hanoi, Vietnam
2   School of Chemical Engineering, Hanoi University of Science and Technology, Hanoi, Vietnam

ABSTRACT

In this study, ZnO nanoparticles were successfully synthesized by the precipitation method, then immobilized onto cotton fabric. The metal oxide nanoparticle-contained fabric exhibits a self-cleaning effect under ultraviolet (UV) illumination. The nanostructure of the prepared samples was detected using Scanning Electron Microscopy (SEM) analysis. The chemical composition changes of the fabrics before and after the modification were detected using The Fourier transform infrared (FT-IR) and Energy Dispersive X-ray Spectroscopy (EDS). After modification with ZnO nanoparticles, the cotton fabric exerted adsorption and decomposition properties again various chemical compounds. Stains of methylene blue (MB), and methylene orange (MO) were introduced into cotton fabric, under UV light, the dyes were faded and ultimately discolored. The degradation of pigments in the solution happened faster and was expressed by the concentration of dyes decreasing over time through UV-vis measurement results. The self-cleaning ability for MB and MO stained cotton fabrics is evaluated quantitatively over time through the K/S value, which showed a good self-cleaning effect.

KEYWORDS

ZnO; Precipitation method; Photocatalysis; Compound decomposition.

INTRODUCTION

The photocatalysis process of semiconductors used in self-cleaning and environmental applications has shown great potential as a sustainable, environmentally friendly, and cost-effective technology. These semiconductor materials have also been used to functionalize various textile fabrics to give them self-cleaning properties. Functional fabrics are capable of oxidizing dyes in the form of solutions and stains. The application of ZnO as a decomposition material for environmental pollutants has also been extensively studied. ZnO is a widely used semiconductor, which not only has numerous applications for stain decomposition and self-cleaning, but is also used in many other fields such as gas sensors, photovoltaic cells, and photodiodes due to its non-toxic properties, low cost, and good optical and photochemical properties [1-3].

The band gap width of ZnO nanoparticles is determined to be 3.37 eV, so they mainly absorb light in the ultraviolet region with an absorption capacity in the range of 200 nm - 400 nm. Nano-ZnO has such an absorption band, so it is widely used as a material for absorbing ultraviolet rays in industry, cosmetics and sunscreens, and ZnO is an important component of drugs for external use. In addition, the fluorescence of ZnO nanoparticles is also of interest in the study of their optical properties [4, 5].

The need for textile items with medical treatment, sanitation, and hygiene is growing as the ecological environment slowly deteriorates. Cotton fabric is a common material that is used extensively in all types of clothing [6]. In the field of garment, 100% cotton fabric is frequently used to create slim-fit clothes, outerwear, and other items because it is a soft natural fabric that is friendly to users' health, has good color dyeing capacity, and has a high biodegradability. However, due to its high moisture absorption and water retention capacity (up to 65% by weight), 100% cotton fabric items are prone to yellow stains and the growth of bacteria and fungi that are dangerous to human health [7-9].

Numerous cutting-edge nanotechnology solar cell applications make use of zinc oxide. Recently, fabrics that can clean themselves have been created using zinc oxide's photocatalytic properties. When a ZnO semiconductor layer is exposed to light,
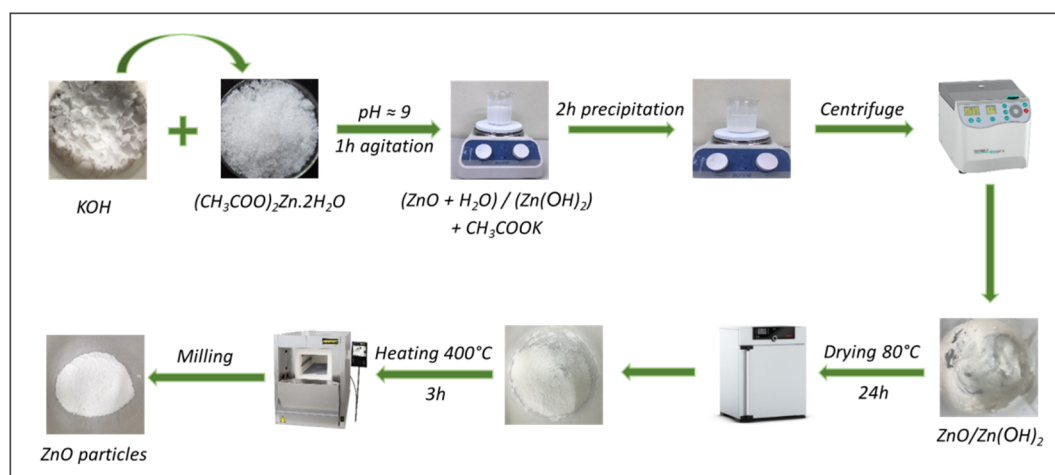
Figure 1. Schematic diagram of the ZnO nanoparticle synthesizing process.

photons with energies equal to or higher than the band gap energy of ZnO will stimulate electrons to the conduction band. Excited electrons on the surface of the material can interact with oxygen atoms in the atmosphere to form reactive oxygen species. These oxygen species are strong oxidizers that can degrade various organic substances in an oxidation-reduction reaction. These processes transform organic substances like dirt, pollutants into things like water and carbon dioxide. ZnO just acts as a catalyst, hence there is no loss in the degradation processes. As a result, the coating layer can play the role of self-cleaning layer [10, 11]. Cotton fabric containing ZnO was reported to expand the traditional applications of textile to various new ways of uses including anti-bacterial and radiation barrier properties against S. aureus and E. coli [12], The ZnO also presented synergistic activities when combined with other materials such as starch, silver nanoparticles, and curcumin. The starch from corn could play the role of adhesive materials for avoiding the leaching disadvantage of nanoparticles [13]. ZnO was well known as the self-cleaning material, particularly when fabricated into hierarchical hybrid nanostructures on cotton fabric. The combination of the Ti3C2Tx MXene/Ni chain/ZnO array hybrid nanostructures endowed the cotton fabric outstanding liquid repellency and durable self-cleaning ability [14].

In this work, ZnO nanoparticles were effectively produced and applied to cotton fabric, the morphology of synthesized ZnO is usually difficult to control due to multiple factors in the reaction process. By controlling the concentrations and time of reaction between chemicals, the grow of ZnO nanoparticles was studied. The resultant materials are investigated using SEM, FT-IR, Tensile testing, and water contact angle meter. The pigment concentration reduction over time using UV-vis testing results reflects the effectiveness of color deterioration in solution. For further photocatalytic assessment, the self-cleaning capacity of ZnO against MB and MO pigments on cotton fabric was quantitatively assessed using the K/S ratio. This discoloration of stains was evaluated

using Ci4200 Spectrophotometric colorimeter after exposing samples to UV light.

METHOD

Material

Zinc acetate ((CH$_3$COO)$_2$Zn) and Potassium hydroxide (KOH) were purchased from Shanghai Yuanye Biotechnology Co., Ltd. All the chemicals used in this study were of analytical grade, and deionized water was utilized when needed.

Methods

Synthesis of ZnO nanoparticles

Utilizing the precipitation procedure, ZnO nanoparticles were synthesized successfully. In the beginning, 100 ml of 0.2 M (CH$_3$COO)$_2$Zn solution and 120 ml of 0.4 M KOH solution were prepared. Under continuous stirring, the KOH solution was steadily added to the zinc salt solution. When the mixture's pH reached the value of 9, the process of addition ceased and the solution was continuously agitated for one hour. After settling for two hours, the precipitate was collected by centrifuging the particles with alcohol and distilled water. The solid particulates were dried at 80°C for 10 hours, then crushed and calcined at 400°C for 3 hours, with a 10°C/min heating rate. The ZnO nanoparticle synthesis was summarized in Figure 1.

The proces of creating ZnO nanoparticle-coated cotton fabrics

The cotton fabric used in this research is treated fabric, purchased in Vietnam, with the main characteristics as follows: single weave, 201.6 g/m^2 weight, 0.54 mm of thickness, and breathability of 220 l/m2/s. 3x3 cm cotton specimens were prepared at room temperature and pressure, and the mass of the fabric samples were ascertained at moisture saturation. In 5 mL of ethanol, one tenth mass of ZnO by the mass of the cotton sample were dissolved. Under the conditions of continuous ultrasonic vibration, the prepared cotton samples were
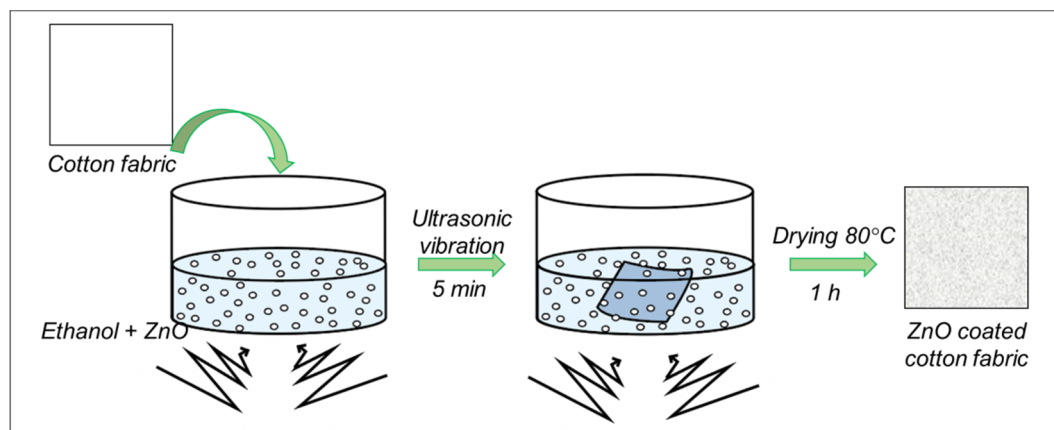
Figure 2. Schematic diagram of ZnO nanoparticle coated fabric.

immersed in a ZnO/ethanol solution for five minutes while maintaining ultrasonic vibration. The fabric sample was then dried at 80°C for one hour to acquire cotton fabric nanocoated with ZnO. The whole proces was summarized as illustrated in Figure 2.

Analytical methods

The morphology and elemental composition of the ZnO-incorporated cotton samples were analyzed using Scanning Electron Microscopy - Energy-Dispersive X-ray Spectroscopy (SEM-EDS) on a Hitachi TM4000 Plus instrument at Hanoi University of Science and Technology with an accelerating voltage of 15 kV. Fourier transforms infrared spectroscopy (FT-IR) spectra were collected using Nicolet iS 50 (Thermo, Waltham, MA, USA) in the range of 4000 to 400 cm−1 with accumulation over 20 scans. Ultraviolet-visible (UV–vis) spectroscopy (Agilent 8453, USA) at the RoHan Research Laboratory, School of Chemical Engineering, Hanoi University of Science and Technology was used for detecting discoloration effects.

The UV-vis measurement method is based on the Bouger - Lambert - Beer law, the optical absorbance of a color-absorbing solution is proportional to the layer's thickness and color temperature [15, 16]:

$$A = \varepsilon c d = \log\left(\frac{l_0}{l}\right) = -\log(T), \qquad (1)$$

in which: A – degree of optical absorption; ε – molecular absorption coefficient; c – solution concentration (mol/l); d – light transmission thickness (cm); l_0 – initial intensity of the light source; l – intensity after passing through the solution; T – transmission.

In qualitative analysis, a common absorbance is a characteristic number for each substance; therefore, by determining the common absorbance, it is possible to determine the qualitative composition of the analytical solution. Absorption spectroscopy is used in quantitative analysis to select the wavelength for measuring optical absorbance.

Photosensitive self-cleaning fabrics are capable of self-cleaning when exposed to light; furthermore, they are resistant to antibiotics and block UV rays. A number of test methodologies can be utilized to evaluate the photoinductive performance of functionalized fabrics. The photocatalytic efficacy of functionalized fabrics is frequently determined by the decomposition of organic pollutants, such as natural colorants or synthetic pharmaceuticals, which are frequently employed as sample pollutants. The optical degradation of pigments is determined by two categories of pigment decomposition activities, including color change in solution and stain decomposition. For the solution's color change, functionalized fabrics were immersed in the dye solution and exposed to UV light. The concentrations of the dye solutions were measured using a UV-Vis spectrophotometer after periodic collection of the solutions over a specified time period [17, 18].

In this investigation, the color value (K/S) of the Ci4200 Spectrophotometric colorimeter was used to evaluate the color loss of stains exposed to UV light for a specified period of time. A decrease in the K/S ratio indicates the disappearance of stains. Self-cleaning can be determined by comparing the K/S values of exposed and unexposed sections of the same stain, as shown below [19]:

$$\frac{K}{S} = \frac{(1-R)^2}{2R}, \qquad (2)$$

in which: K - absorption coefficient; S - scattering coefficient; R - reflectance of the dyed cotton fabric; K/S represents the color fastness of the dye on the surface and is proportional to the amount of pigment present on the surface.

(a)   (b)
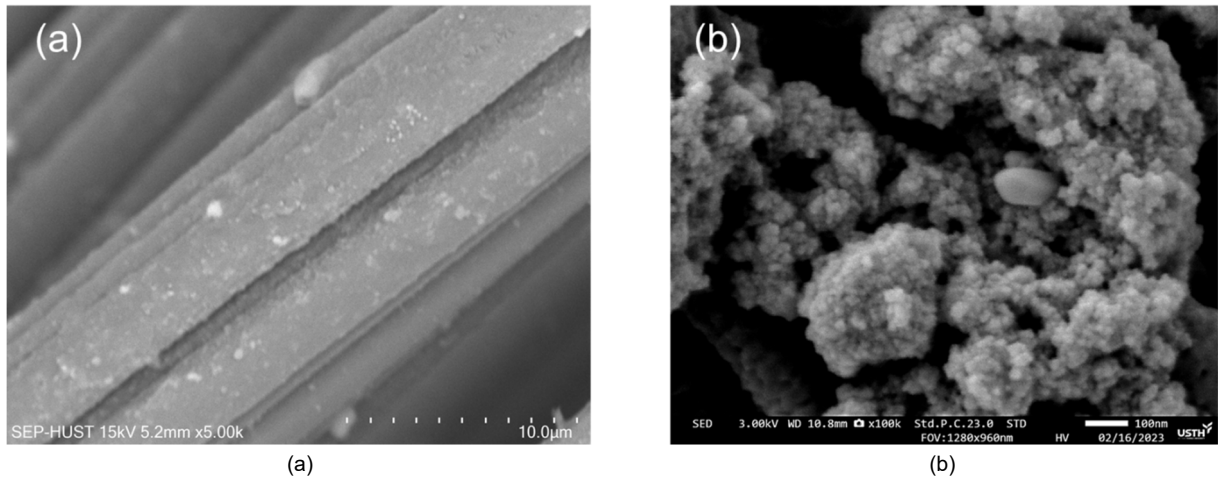
Figure 3. (a) SEM image of ZnO on cotton fabric, (b) SEM image of ZnO nanoparticles.
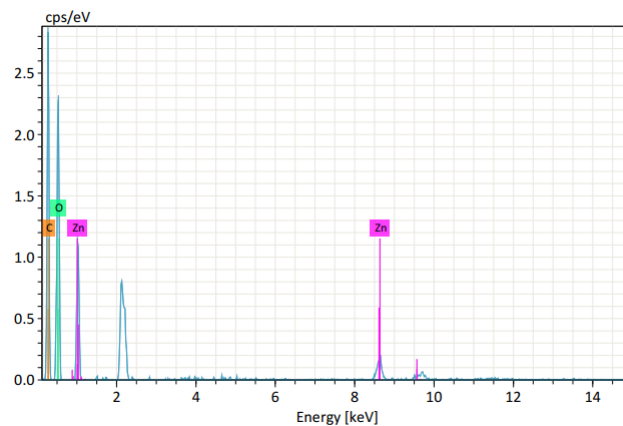
Figure 4. EDS results of cotton fabric coated with ZnO.
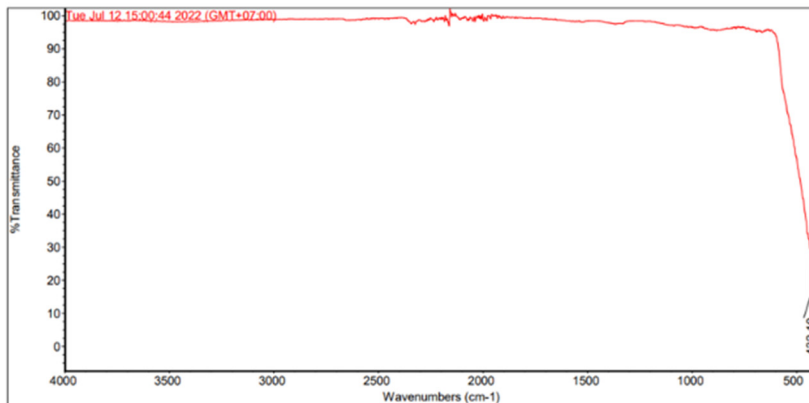
Figure 5. FTIR spectrum with attenuated total reflectance (ATR) of synthesized ZnO nanoparticles.

RESULTS AND DISCUSSION

Characterization of ZnO catalyst

SEM, EDS, FTIR analysis

ZnO nanoparticle catalyst was analyzed by SEM-EDS, which is shown in Figures 3 and 4. The results show that the ZnO particles are distributed on the fabric surface, Figure 3 (a). In Figure 3 (b), ZnO nanoparticles were observed to be less than 50 nm for each particle, however, without the scattering liquid environment, the ZnO nanoparticles tend to aggregate extensively. On the surface of the cotton fiber, the white dots were ZnO nanoparticles that immobilized uniformly on the surface of the fibers.

Cotton fabrics containing ZnO with a mass ratio of 10:1, corresponding to an elemental composition ratio of 42.33 percent carbon, 47.97 percent oxygen, and 3.82 percent zinc. Figure 4 depicts the outcome of EDS analysis. According to the results, the ZnO-containing fabric has a ZnO content comparable to theoretical calculations, and the quantity of ZnO successfully coated on cotton is lost in a negligible amount. Due to the fact that the EDS measurement is a surface measurement and the working range is on the surface and in a small area, as well as the fact

(a)

(b)
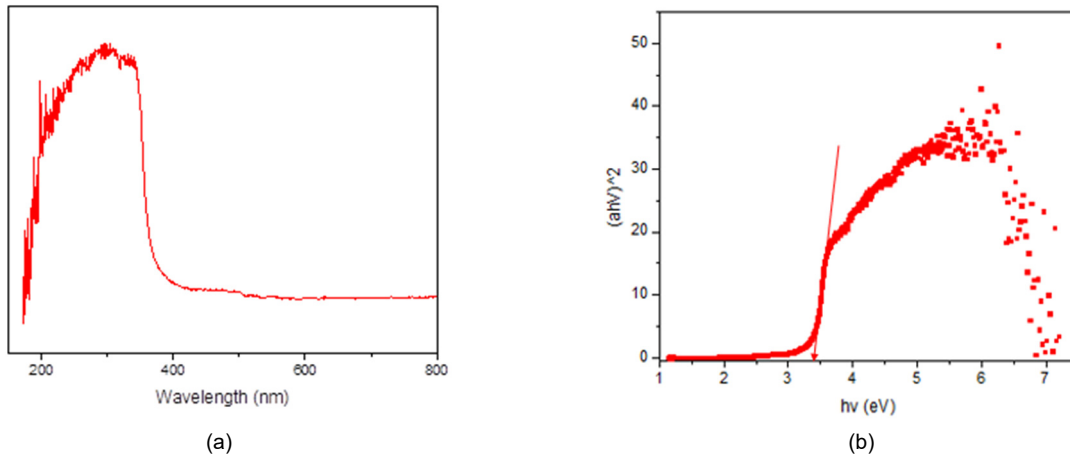
Figure 6. (a) UV-Vis DRS Absorption Spectral Range, and (b) UV-Vis Diffuse Emission Spectroscopy (UV-Vis DRS).

Table 1. Tensile strength of cotton fabric before and after treatment with ZnO nanoparticles.

	Sample size	Mean tensile strength with standard deviation [N]	Mean comparison (Student's t test)
Warp of cotton fabric	5	647.36±8.74	Warp of cotton fabric and warp of ZnO coated cotton fabric t* (p=0.05) = 6.95 t = 2.36
Warp of ZnO nanoparticle coated cotton fabric	5	595.38±12.14	
Weft of cotton fabric	5	433.61±6.85	Weft of cotton fabric and weft of ZnO coated cotton fabric t* (p=0.05) = 9.5 t = 2.31
Weft of ZnO nanoparticle coated cotton fabric	5	388.62±6.54	

t = Student's test value; t* = minimum t value for rejecting the null hypothesis with a 95% significance.

that the measured material surface is not perfectly flat and the ZnO coverage is not ideal, there is a discrepancy between the measurement and the theoretical calculation.

Figure 5 depicts the FTIR spectrum of ZnO nanoparticles; a broad band observed at approximately 400 cm-1 is zinc oxide's absorption band. There are additional insignificant bands in the spectrum at 1400 cm-1, 1300 cm-1, and 800 cm-1. These adsorption bands are presumably due to airborne CO_2 absorption and can be disregarded [20, 21].

UV-Vis Diffuse Reflectance Spectroscopy (UV-Vis DRS)

UV-DRS is a technique used to investigate the optical properties of semiconductor materials. The wavelength range of the absorption spectrum shown in Figure 6 (a) is 200 nm to 800 nm. Using the graph of Tauc Figure 6 (b) and the UV-DRS spectrum, the optical transition energy of the ZnO nanoparticle samples was calculated as follows [22]:

$$(\alpha h v)^n = A(h v - E_g), \qquad (3)$$

where: hv – photon energy; E_g – optical band gap; A – is constant; α – absorption coefficient, n can take the values 2 or 1/2, for direct or indirect optical transitions, respectively.

The E_g values are deduced from the graph of $(\alpha h v)^n$ relative to hv and extrapolated a line to the hv axis. Usually, ZnO is a material with a direct band gap. Accordingly, for n = 2 the highest optical transition is attributed to the difference between the valence and conduction bands, creating a functional band gap. ZnO excitation can occur through indirect optical conversion due to defect generation and/or complex phases. The energy band gap of nano ZnO is found in the range of 3.2–3.7 eV and from the graph the value was calculated to be 3.4 eV. The results show that the absorption of ZnO nanoparticles is in the UV region and therefore all irradiation experiments were performed using a UV light source [23].

Features of ZnO nanoparticles-coated cotton fabric

Tensile strength

According to national standard TCVN 1754:1986 (Woven fabrics - Method for determining tensile strength and extension at break), the experiments were conducted at the Laboratory of Textile Materials, School of Textile - Leather and Fashion, Hanoi University of Science and Technology. In particular, the dimensions of the test samples are 350x50 mm with a functional dimension of 200x50 mm. In a dried state, the external tensile force of cotton fabric was measured before and after surface treatment with
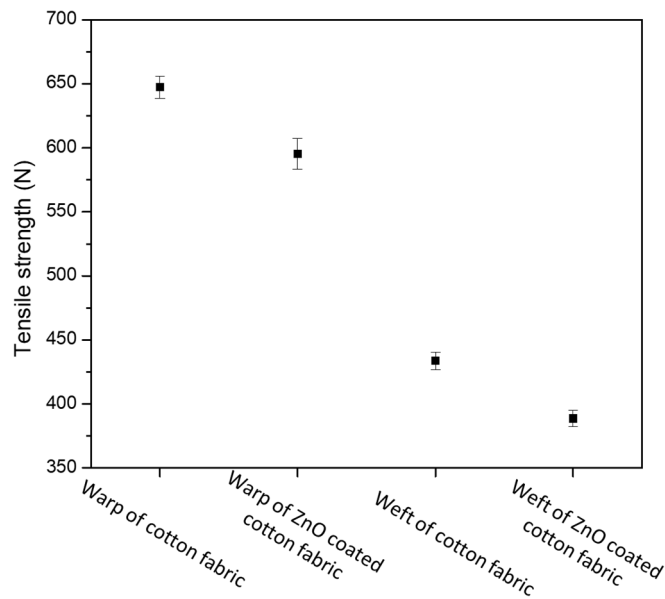
Figure 7. Mean tensile strength at break of warp of cotton fabric, warp of ZnO nanoparticle coated cotton fabric, weft of cotton fabric, and weft of ZnO nanoparticle coated cotton fabric with standard deviation.
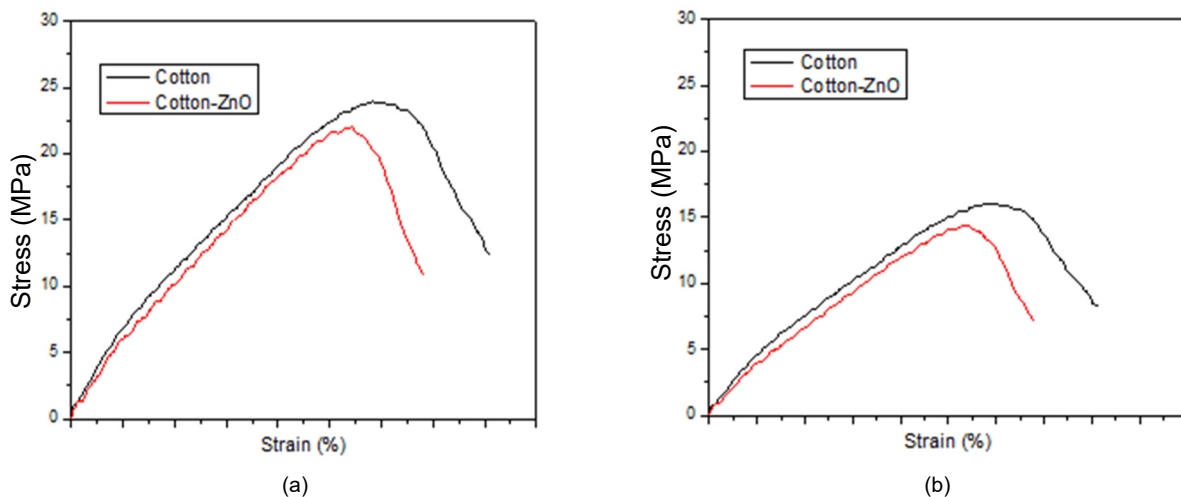
Figure 8. Representative stress–strain diagram of cotton fabric before and after ZnO nanoparticle coating treatment a) in the longitudinal direction and b) in the horizontal direction.

ZnO in vertical and horizontal positions. The resulting mean tensile strength at break with standard deviation is depicted in Table 1 and Figure 7.

From the recorded results, it can be seen that, after immersing the cotton fabric in ethanol containing ZnO nanoparticles to create self-cleaning fabric, the breaking strength of the fabric was reduced, specifically about 8.03% in the longitudinal direction and about 10.38% horizontally, Figure 7. The explanation for the strength reduction of cotton fabric after ZnO nanocoating is due to the fact that the nanometer-sized semiconductor molecules penetrate and form bonds with the fiber structure, leading to the weakening of hydrogen bonding and intermolecular bonds within the molecular network of the fiber.

The representative graphs of contton fabrics after treatment with ZnO showed a decrease compared to the original cotton samples in terms of stress. The details are illustrated in Figure 8.

Fabric breathability

From Table 2 and Figure 9, the ZnO nanoparticle-coated fabric is less breathable than the original cotton fabric. Particularly, there is an 8.35% reduction in permeability compared to pristine fabrics. The decline in the breathability of the fabric following ZnO coating treatment can be explained by the nanometer-sized ZnO particles adhering to the surface around the fibers, thereby decreasing the pore size.

Moisture absorption

In this study, experiments were carried out with an ordinary oven with fabric samples prepared according to National Standard TCVN 1749:1986 with dimensions of 8x8 cm (weight about 8-10 g). The actual moisture content of the test sample - W in % according to the formula:

Table 2. Fabric breathability [l.m⁻².s⁻¹]

	Sample size	Fabric breathability with standard deviation [l.m⁻².s⁻¹]	Mean comparison (Student's t test)
Cotton fabric	10	221.3±2.89	t* (p=0.05) = 13.73
ZnO nanoparticles coated cotton fabric	10	202.8±3.13	t = 2.09

t = Student's test value; *t** = minimum t value for rejecting the null hypothesis with a 95% significance.
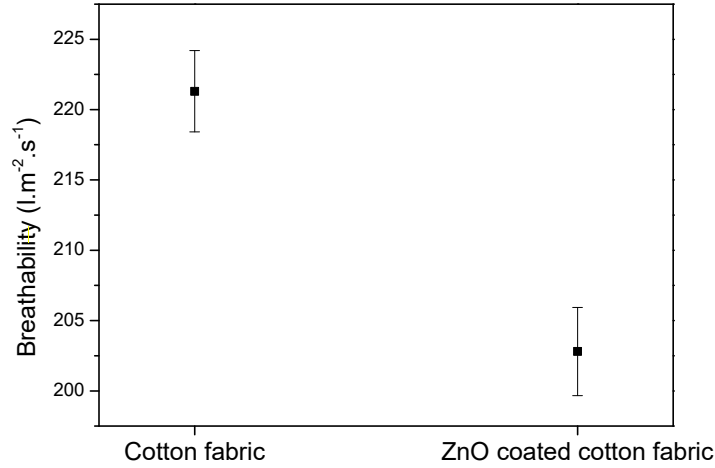
Figure 9. Breathability of cotton fabric and ZnO coated cotton fabric.

Table 3. Results of measuring moisture absorption and liquid absorption of cotton fabric compared to ZnO nanoparticle coated cotton fabric.

	Sample size	Cotton fabric	ZnO coated cotton fabric	Mean comparison (Student's t test)
Saturation state *m* [g]	5	10.31±0.02	10.94±0.03	t* (p=0.05) = -30.69, t = 2.36
Dry state m_k [g]	5	8.22±0.02	8.88±0.04	t* (p=0.05) = -28.14, t = 2.45
Wet state m_n [g]	5	11.65±0.08	11.79±0.16	t* (p=0.05) = -1.47, t = 2.45
Water absorption capacity *LAC* [%]	5	41.74±0.63	32.73±1.37	t* (p=0.05) = 11.96, t = 2.45
Hygroscopicity *W* [%]	5	25.37±0.11	23.29±0.22	t* (p=0.05) = 17.17, t = 2.45

t = Student's test value; *t** = minimum *t* value for rejecting the null hypothesis with a 95% significance.

$$W = (m - m_k)/m_k, \qquad (4)$$

where: *m* is the mass of the test piece before drying [g], m_k is the mass of the test piece after drying [g]. The resulting liquid absorptive capacity (*LAC*) of each sample is presented in percentage:

$$LAC = \left(\frac{m_n - m_k}{m_k}\right)100, \qquad (5)$$

where:m_k [g] is the mass of the dry fiber, m_n [g] is the mass of the fiber and liquid (distilled water) absorbed at the end of the test.

From the survey results in Table 3, it can be seen that the liquid absorption capacity of cotton fabric is relatively good (more than 41.74%) and the moisture absorption is 25.36%. This result is due to the influence of hydrophilic groups in the structure of cotton fibers (the main components are cellulose molecules). In this case, there is an interaction between the water molecules and the structure of the fiber, because natural fibers (including regenerated fibers of natural origin) with hydrophilic groups interacting with OH- group containing liquid will absorb a large amount of water. During the first interaction between the fabric and water, the water will attach to the hydrophilic groups of the fabric. Then, water molecules either attach to hydrophilic groups or attach to previously attached water molecules to form a new layer. Water molecules directly bonded to hydrophilic groups are tightly bound and have limited movement. The water molecules are indirectly connected to each other, have a looser structure, and move more easily.

Liquid absorption ability (water absorption) of cotton fabric coated with ZnO nanoparticles by volume ratio of fabric: ZnO = 10:1 was experimentally recorded as 32.73% and the moisture absorption rate reached 23.28%. Values tend to decrease compared to untreated cotton samples. The reason given to reduce the hygroscopic value of the fabric is that the ZnO oxide nanoparticles tend to enter the gaps between the fabrics, capturing the localization of water molecules that can be held on the fabric. At the nanoscale, these catalytic particles are insoluble in
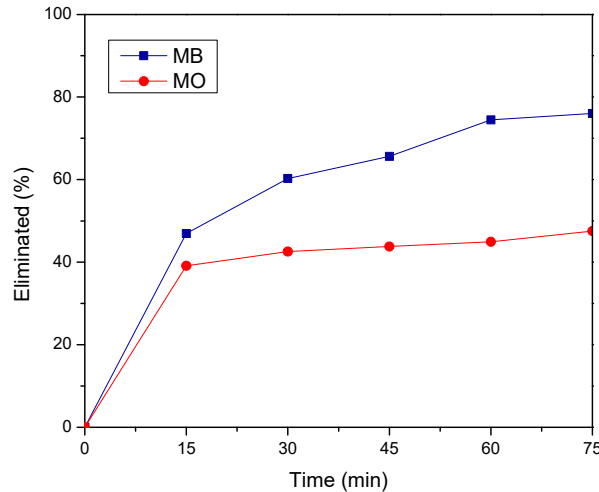
Figure 10. The ability (a) to absorb MB, (b) MO of ZnO nanoparticles, and (c) MB, MO colorant conversion chart of ZnO nanoparticles.

(a)   (b)
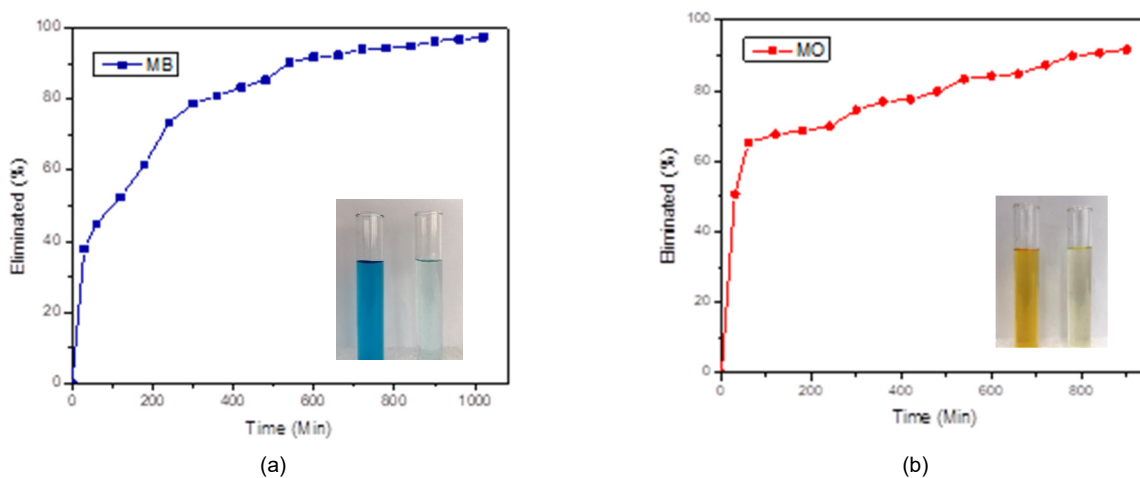
Figure 11. (a) MB and (b) MO decomposition by photodegradation effect utilized ZnO nanoparticles under UV light irradiation.

water but dispersed and suspended in water as a suspension. Therefore, the fabric coated with ZnO nanoparticles has lower hygroscopicity and water absorption capacity than ordinary cotton fabrics. In addition, the bond between the ZnO nanoparticles and the cotton fabric is mechanical bonding, with the demonstration of affinity and attraction between the molecules (Van der Waals attraction) making it possible for them to fall off the fabric.

The absorption and degradability of ZnO nanoparticles

MB, MO adsorption capacity of ZnO nanoparticles

The adsorption of pigments onto ZnO takes place due to the interaction between ZnO molecules in equilibrium state with small pigment molecules. On the surface of the ZnO molecules, the attraction happens because of various functional present groups. As a result, the pigment is adsorbed on the surface of ZnO decreasing the dye concentrations. In the practice of this experiment, the amount of ZnO used was 0.005 grams per 10 ml against 10 ppm MB and 10 ppm MO solutions. The experiment was completely done within 30 min in the dynamic state using HY4 horizontal shaker in the absence of light.

According to the results from Figure 10 ZnO effectively absorbs the dye color in the first 15 min (estimated at 46.92% against MB) and slows down for the next 15 min. At the end of the adsorption process, which lasted for about 75 minutes, the MB concentration reduction over time reached 76.01%. For MO, in the first 30 minutes of the adsorption process, the amount of MO decrease reached about 42.56% and ended after about 75 minutes with the dye conversion rate in the range of 47.56%.

The ability to decompose MB, MO under UV light condition

The pigment solutions, after undergoing adsorption in the dark chamber, continue to be assessed for color reduction using the photodegradation effect using ZnO under the effect of 60W UV lamp under continuous agitation.

From Figure 11, the MB and MO dye solutions lost color quickly in the first 30 minutes (MB reached 38%, MO reached 51%), and gradually decreased in the following times. After 17 hours, the discoloration of MB ended with a result of 97%, and that of MO was 92%.

Table 4. Mass of cotton and cotton fabric coated with ZnO nanoparticles.

	Cotton fabric [g]	ZnO nanoparticles coated cotton fabric [g]
Sample 1	1.19	1.29
Sample 2	1.21	1.31
Sample 3	1.21	1.32
Sample 4	1.19	1.31
Sample 5	1.18	1.29
Average	1.20	1.30
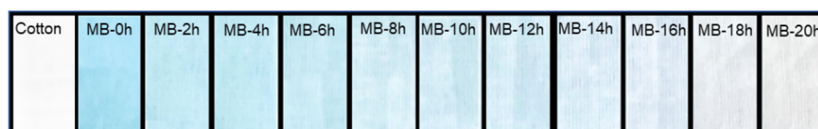
(a)
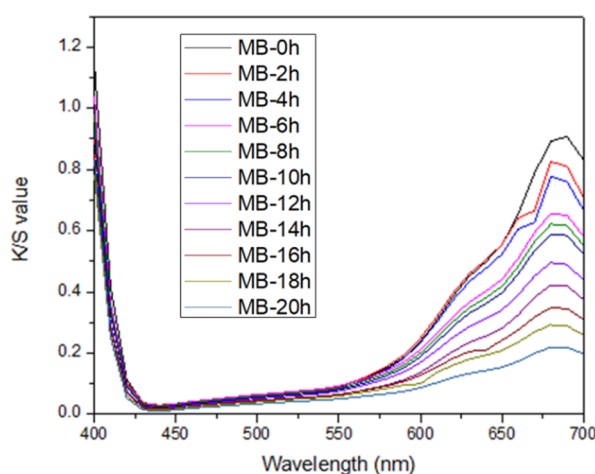
(b)

Figure 12. (a) The color change of MB on ZnO coated cotton fabric every 2 hours and (b) The graph of color intensity change of MB on cotton fabric containing ZnO under the effect of UV light.

The self-cleaning ability of ZnO nanoparticles-coated cotton fabric

By impregnation method, the cotton-ZnO fabric samples used in the self-cleaning experiment has a mass of ZnO equal to one tenth the mass of cotton fabric. According to calculations, the amount of ZnO nanoparticles on the fabric is about 10% with the average weight value of the cotton fabric sample using the same size of 3x3cm given in the Table 4.

In this study, a catalyst-coated fabric sample containing ZnO nanoparticles was stained with 10 ml of colorant. After each period of time under UV irradiation, the color of the fabric samples was recorded on the colorimeter Ci4200 Spectrophotometer at the material testing laboratory, Hanoi University of Science and Technology.

Self-cleaning ability of cotton fabric containing nano ZnO for MB pigment

Under UV irradiation with a 60W UV lamp, the K/S values of MB tinted ZnO coated cotton samples can be displayed in Figure 12(b). After 20 h of UV irradiation, the color of the untreated cotton sample is not changed during the test, while the color of the ZnO-coated fabric faded, the Figure 12(a) illustrates the changing color photos of MB stained ZnO-coated samples over time. The fading of the blue color of MB on the fabric can also be clearly seen with the naked eye as shown in Figure 12(a).

The color change of fabrics containing MB is well-observed at the wavelength ranges above 630 nm. The experiment stops when the K/S value does not change or changes are small, or insignificant. Because the process of photodecomposition is a one-way reaction process.

The self-cleaning ability of cotton fabric containing nano ZnO for MO pigment

Similar to MB, the color change of MO-stained ZnO/cotton fabric can also be seen clearly and quantified through the K/S value histogram at the wavelength range of 420 – 500 nm. The color of the fabric samples changed with MO decomposed through time, and the differences were depicted in Figure 13 (a) and (b).

(a)

(b)
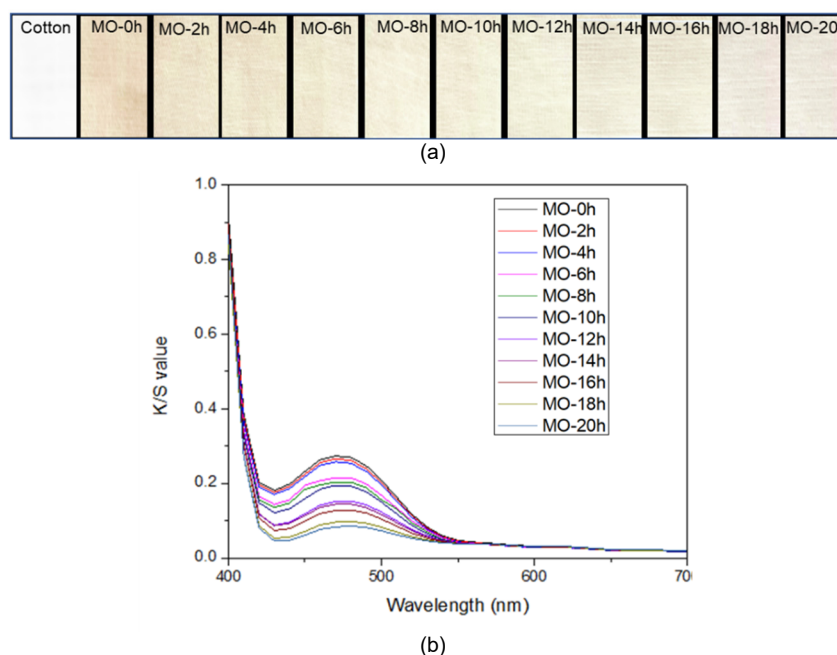
Figure 13. (a) The color change of MO stained ZnO coated cotton fabric every 2 hours and (b) The graph of color intensity change of MO on cotton fabric containing ZnO under the effect of UV light over time every 2 hours.

CONCLUSION

In this study, ZnO metal oxide nanoparticles were successfully synthesized and immobilized onto cotton fabrics, creating a self-cleaning fabric. The properties of ZnO nanoparticles were analyzed through SEM, FTIR, EDS, and UV-Vis characteristics. The self-cleaning ability of the ZnO coated cotton fabric was evaluated and quantified through K/S values. The results showed that under continuous UV illumination, MB and MO pigments stained cotton fabric coated with ZnO nanoparticles were faded after about 20 hours, the decoloration can be observed clearly through time. The findings of this study can be considered as a development basis for self-cleaning fabric under the effect of actual sunlight (including visible and invisible light). It is also the premise for the development of self-cleaning fashion products with high applicability.

REFERENCES

1. Basnet P., Samanta D., Chanu T.I., et al.: Visible light facilitated degradation of alternate dye solutions by highly reusable Mn-ZnO nano-photocatalyst, Journal of Alloys and Compounds 867, 2021, 158870.
https://doi.org/10.1016/j.jallcom.2021.158870
2. Kaliraj L., Ahn J.C., Rupa E.J., et al.: Synthesis of panos extract mediated ZnO nano-flowers as photocatalyst for industrial dye degradation by UV illumination, Journal of Photochemistry and Photobiology B: Biology 199, 2019, 111588.
https://doi.org/10.1016/j.jphotobiol.2019.111588
3. Sharma P., Kumar N., Chauhan R., Singh V., Srivastava V.C., Bhatnagar R.: Growth of hierarchical ZnO nano flower on large functionalized rGO sheet for superior photocatalytic mineralization of antibiotic, Chemical Engineering Journal 392, 2020, 123746.
https://doi.org/10.1016/j.cej.2019.123746
4. Sarkar C., Basu J.K., Samanta A.N.: Synthesis of novel ZnO/Geopolymer nanocomposite photocatalyst for degradation of congo red dye under visible light, Environmental Nanotechnology, Monitoring & Management 16, 2021, 100521.
https://doi.org/10.1016/j.enmm.2021.100521
5. Batra V., Kaur I., Pathania D., et al.: Efficient dye degradation strategies using green synthesized ZnO-based nanoplatforms: A review, Applied Surface Science Advances 11, 2022, 100314.
https://doi.org/10.1016/j.apsadv.2022.100314
6. Alagarasan D., Harikrishnan A., Surendiran M., et al.: Synthesis and characterization of CuO nanoparticles and evaluation of their bactericidal and fungicidal activities in cotton fabrics, Applied Nanoscience, 2021, pp. 1-10.
https://doi.org/10.1007/s13204-021-02054-5
7. Wei D.W., Wei H., Gauthier A.C., et al.: Superhydrophobic modification of cellulose and cotton textiles: Methodologies and applications, Journal of Bioresources and Bioproducts, 5(1), 2020, pp. 1-15.
https://doi.org/10.1016/j.jobab.2020.03.001
8. Román L.E., Gomez E.D., Solís J.L., et al.: Antibacterial cotton fabric functionalized with copper oxide nanoparticles, Molecules, 25(24), 2020, 5802.
https://doi.org/10.3390/molecules25245802
9. Qian J., Dong Q., Chun K., et al.: Highly stable, antiviral, antibacterial cotton textiles via molecular engineering, Nature Nanotechnology, 18(2), 2023, pp. 168-176.
https://doi.org/10.1038/s41565-022-01278-y
10. Karagoz S., Kiremitler N.B., Sarp G., et al..: Antibacterial, antiviral, and self-cleaning mats with sensing capabilities based on electrospun nanofibers decorated with ZnO nanorods and Ag nanoparticles for protective clothing applications, ACS Applied Materials & Interfaces 13(4), 2021, pp. 5678-5690.
https://doi.org/10.1021/acsami.0c15606

11. Milionis A., Tripathy A., Donati M., et al.: Water-based scalable methods for self-cleaning antibacterial ZnO-nanostructured surfaces, Industrial & Engineering Chemistry Research, 59(32), 2020, pp. 14323-14333.
https://doi.org/10.1021/acs.iecr.0c01998

12. Sezgin E., Esen Keçeci M., Akmaz S., et al.: Heterogeneous Cr-zeolites (USY and Beta) for the conversion of glucose and cellulose to 5-hydroxymethylfurfural (HMF), Cellulose 26, 2019, pp. 9035-9043.
https://doi.org/10.1007/s10570-019-02702-8

13. [El-Nahhal I.M., Salem J., Anbar R., et al.: Preparation and antimicrobial activity of ZnO-NPs coated cotton/starch and their functionalized ZnO-Ag/cotton and Zn(II) curcumin/cotton materials, Scientific Reports, 10(1), 2020, 5410.
https://doi.org/10.1038/s41598-020-61306-6

14. Wang S., Li D., Zhou Y., Jiang L.: Hierarchical Ti3C2T x MXene/Ni chain/ZnO array hybrid nanostructures on cotton fabric for durable self-cleaning and enhanced microwave absorption, ACS nano, 14(7), 2020, pp. 8634-8645.
https://doi.org/10.1021/acsnano.0c03013

15. Mayerhöfer T.G., Pahlow S., Popp J.: The bouguer-beer-Lambert law: Shining light on the obscure, ChemPhysChem 21(18), 2020, pp. 2029-2046.
https://doi.org/10.1002/cphc.202000464

16. Mäntele W., Deniz E.: UV–VIS absorption spectroscopy: Lambert-Beer reloaded, Spectrochimica Acta Part A: Molecular and Biomolecular Spectroscopy, 173, 2017, pp. 965-968.
https://doi.org/10.1016/j.saa.2016.09.037

17. Dalawai S.P., Aly M.A.S., Latthe S.S., et al.: Recent advances in durability of superhydrophobic self-cleaning technology: a critical review, Progress in Organic Coatings, 138, 2020, 105381.
https://doi.org/10.1016/j.porgcoat.2019.105381

18. Nguyen-Tri P., Tran H.N., Plamondon C.O., et al.: Recent progress in the preparation, properties and applications of superhydrophobic nano-based coatings and surfaces: A review, Progress in organic coatings, 132, 2019, pp. 235-256.
https://doi.org/10.1016/j.porgcoat.2019.03.042

19. Hossain I., Moniruzzaman M., Maniruzzaman M., et al.: Investigation of the effect of different process variables on color and physical properties of viscose and cotton knitted fabrics, Heliyon, 7(8), 2021, e07735.
https://doi.org/10.1016/j.heliyon.2021.e07735

20. Estrada-Urbina J., Cruz-Alonso A., Santander-González M., et al.: Nanoscale zinc oxide particles for improving the physiological and sanitary quality of a Mexican landrace of red maize, Nanomaterials, 8(4), 2018, 247.
https://doi.org/10.3390/nano8040247

21. Zak A.K., Abrishami M.E., Majid W.A., et al.: Effects of annealing temperature on some structural and optical properties of ZnO nanoparticles prepared by a modified sol–gel combustion method, Ceramics International, 37(1), 2011, pp. 393-398.
https://doi.org/10.1016/j.ceramint.2010.08.017

22. Khan S.A., Sahani R., Tripathi R.P., et al..: Influence of gamma-irradiation on the optical and structural properties of Se85Te15-xBix nano-thin chalcogenide films, Radiation Physics and Chemistry, 188, 2021, 109659.
https://doi.org/10.1016/j.radphyschem.2021.109659

23. Boulahlib S., Dib K., Özacar M., et al.: Optical, dielectric, and transport properties of Ag-doped ZnO prepared by Aloe Vera assisted method, Optical Materials 113, 2021, 110889.
https://doi.org/10.1016/j.optmat.2021.110889

VIRUSES AND THEIR PENETRATION THROUGH FIBROUS STRUCTURES: A REVIEW

MILITKÝ, JIŘÍ[*]; WIENER, JAKUB AND KŘEMENÁKOVÁ, DANA

Department of Material Engineering, Faculty of Textile Engineering, Technical University of Liberec, Liberec, Czech Republic

ABSTRACT

In the first part of this review the necessary information about structure and chemical composition of viruses are briefly discussed on the basic level. Main types of interaction of viruses with human cells are briefly described. The basic method of suppressing the spread of viruses from the surroundings of a healthy person and into the surroundings of an infected person is the use of protective equipment, especially face masks and respirators, where the active element is a fibrous structure. The protective functions of these structures depend on their composition (usually hydrophobic materials), construction (fabrics, knitted fabrics, non-woven fabrics, nano-meshes), morphology (porosity, thickness, pore distribution), the form of virus propagation (usually in water droplets as a type of aerosol), interaction conditions with the surface of the protective layer (speed of impact, conditions of capture on the surface of the fibrous phase, speed of penetration) and the method of virus inactivation (usually contact or very short-range interaction). It is therefore a very complicated problem that is often solved using a combination of mathematical modeling and simulation. The purpose is to present some methods of solving problems related to the protective function of fiber structures, which allow the specification of the suitability of these structures for real use.

KEYWORDS

SARS 2 virus structure; Viral attack; Filtration of droplets; Spreading on porous structures; Protective layers; Distribution of pore radii.

INTRODUCTION

The viruses are tiny organisms composed from many structural components influencing their penetration through fibrous materials and entering to human cells where it replicates. Especially the coronavirus SARS-CoV-2 is important because it is responsible for COVID pandemic. Coronavirus SARS-CoV-2 is composed from four types of structural proteins with different chemical composition and functionalities. Information about composition of this and similar viruses and modes of their interactions with human cells is advantageous for the creation of antiviral fibrous layers in face masks and antiviral clothing [1].

The wearing of face masks made of textile fabrics (generally referred to as "cloth masks") is likely to be a simple means of mitigating the transmission of Covid-19 (by preventing the transmission of contaminated droplets by an infected person) [2, 3]. Wearing a mask in public places and in the working environment is becoming part of everyday life. Face masks of type ″Protecting your″ are designed to provide sufficient filtration efficiency to stop the transfer of microdroplets ($\geq$ 5 μm) from an infected person to the environment [2]. Masks of the type "I protect myself" type are primarily intended for protection against the penetration of viruses and contaminated droplets from the environment [2]. In order to ensure the success of the functions of masks, the impact of various factors and influences that can avoid increase in the self-infection of an infected individual or create a path for secondary infection of uninfected subjects should be specified [3, 5]. There is no doubt that effective filtering ability and permeability of virus-containing droplets is a priority. The transparency of masks is also related to the loss of heat in the facial area, which plays an important role in the thermoregulation of the whole body [4]. Due to the high concentration of thermoreceptors, 20% of the total heat loss is cooling the skin [4].

The main aim of this review is to discuss problems related to the protective function of porous fibrous structures, and their interaction with water droplets transporting viruses. The structure of SARS 2 virus, basic mechanisms of interaction with human cells and spread by respiration into atmosphere are briefly discussed. Capture of droplets and particles by a fibrous layer (filtration) and their interaction with porous surfaces is predicted. Protective fibrous layers

---
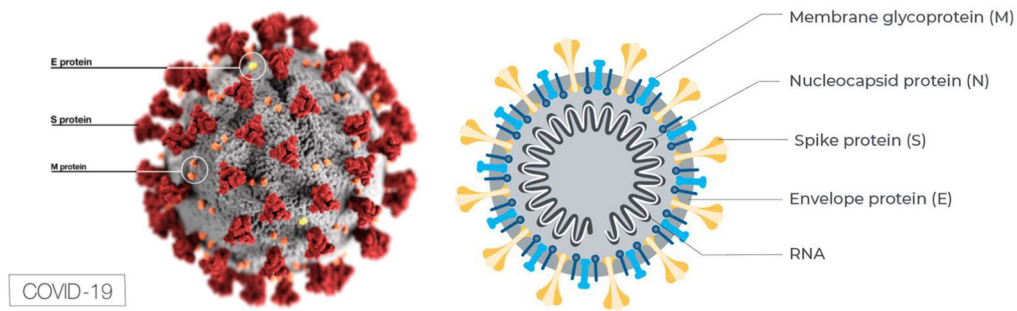
Figure 1. SARS-CoV-2 coronavirus (size 50–200 nanometers) (modified from [31, 32]).

(a)	(b)
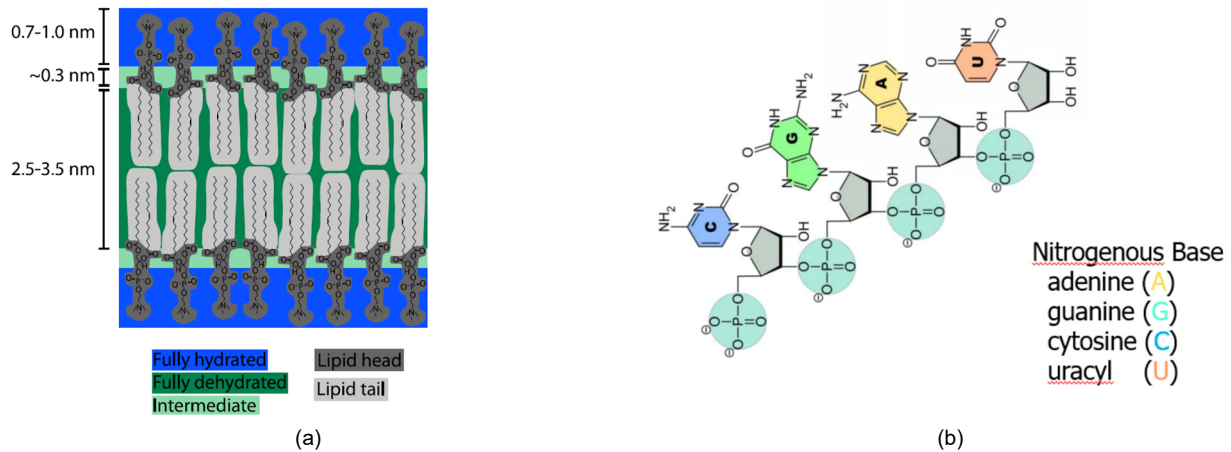
Figure 2. (a) Phospholipid bilayer (modified from [32, 33]), (b) Composition of RNA viruses (modified from [34]).

that are prepared for trapping viruses shown. There are mostly nano/micro assemblies prepared by electrospinning or non-woven textiles created by a combination of melt blown and electrospinning techniques. The pore size of these layers as tool for improvement of filtration characteristics active part of face masks are predicted.

SARS-COV-2 VIRUS

SARS-CoV-2 is a 50–200 nm globular RNA virus with an approximately spherical envelope and spikes (S-type proteins) that allow it to enter human cells where it replicates (Fig.1). It belongs to single-stranded RNA viruses with positive polarity. The coating, which is formed by a phospholipid bilayer (Fig. 2(a)), can be removed with alcohol or soap. The SARS-CoV-2 coronavirus (hereafter NKS, see Fig. 1) contains four structural proteins, known as S (tip), E (envelope), M (membrane) and N (nucleocapsid) [31].

The N-protein holds the RNA genome and the S, E and M proteins together form the envelope of the virus body. The S-protein is responsible for allowing the virus to attach to the host cell membrane. Chemically, they are primarily glycoproteins containing oligosaccharides covalently bound to the side groups of polypeptide chains. Bonds with glycoproteins of the virus are formed mainly by copper ions and the resulting complexes can prevent or strongly limit NKS replication in human cells [32, 35].

The RNA of coronaviruses is terminated at one end by a so-called "cap", which protects the viral RNA from the natural immunity of cells and degradation by cellular enzymes. At the other end, the viral RNA is terminated by a sequence of adjacent adenosine nucleotides (the so-called polyadenylate group). These modifications at both ends enable translation and increase RNA stability in cells. RNA is composed of ribose, which is a phosphate-type polysaccharide containing adenine, guanine, cytosine and uracil in the main chain (Fig. 2(b)). The O-H bond in RNA ribose makes the molecule more reactive. RNA is not stable under alkaline conditions and is susceptible to enzymatic degradation. RNA is constantly being produced, used, degraded and recycled. RNA is relatively resistant to UV damage.

It is highly desirable to solve the problem of masks preventing the penetration of NCS into the mouth and nose area of healthy persons (masks for prevention - RP) and masks preventing the spread of NCS from the mouth and nose area of infected persons (masks for the protection of the environment - RO).

INTERACTION OF VIRUSES WITH CELLS

Viruses are completely dependent on the cells they infect. These provide them with energy, metabolic intermediates and most (in some cases all) of the enzymes needed for their replication [35]). Viruses affect cells in a number of ways that can be divided into three partially overlapping categories:
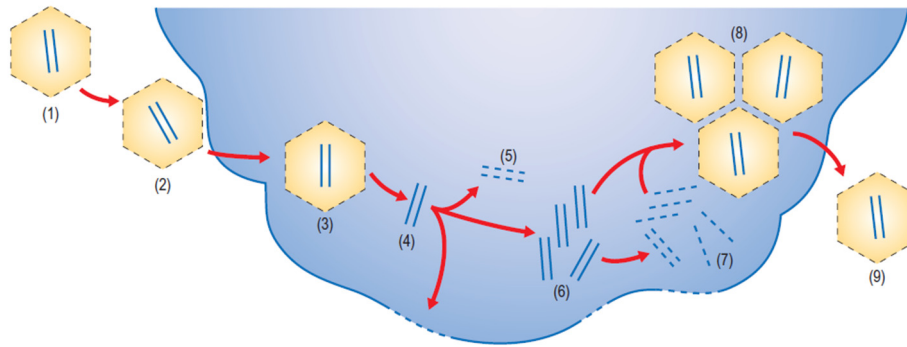
Figure 3. A simplified cycle of viral action where a hypothetical viral particle (1) attaches to the cell surface (2), enters the cell (3), is uncoated (4), undergoes temporal transcription and translation (5), then replicates the viral nucleic acid (6), final transcription and translation (7) and finally the assembly of new viral particles (8) and their release from the cell (modified from [35]).

1. Viruses that infect cells replicate within them and produce new virions that are released. This is the cytolytic cycle where the infection is productive and the cell culture exhibits cytopathic effects that are often characteristic of the infecting virus. In some cases, viruses are produced from infected cells, but the cells are not completely destroyed by the infection, so it is a non-cytolytic process that can become long-term.

2. Viruses that infect cells but do not complete the replication cycle. The infection is thus called abortive or non-productive. An abortive infection can be caused by a mutation of the virus, so that some basic function is lost, or defective interfering particles are produced, or interferons act. This may be possible in a steady state where infected and uninfected cells coexist and there is only limited virus production.

3. Viruses that do enter cells but are not produced by infected cells. The virus is maintained inside the cell in the form of DNA, which replicates in association with the DNA of the host cell. The host cell is called non-permissive and the infection is non-productive. Occasionally, this type of interaction leads to transformation, where the cell exhibits many of the characteristics of a tumor. In other cases, a latent infection follows, where the virus does not replicate and the cell retains its normal properties. First, there is contact and capture of viruses (adsorption) on the cell surface. The virus then enters the host cell and begins to replicate. The newly created virus particles are clustered and released (the diagram is in Fig. 3).

The basic parts of this cycle related to the possibilities of passivating the action of viruses by external means are their capture, penetration and release by replication.

Virus capture (adsorption)

The initial virus-cell interaction is a random collision and depends on the relative concentration of the virus. Under in vitro conditions, the ionic composition of the culture medium is important, when both viruses and cells are negatively charged and tend to repel each other at neutral pH. The presence of cations such as Mg^{2+} helps promote contact. Adsorption then takes place via specific binding sites and receptors on the plasma membrane of the cell. It is largely a heat- and energy-independent process. Viruses vary greatly in the type of cells they can adsorb to, depending on the nature of the sites they can attach to. The presence of receptors determines whether the cell will be susceptible to the virus, but the cells must also be permissive: that is, for the successful production of new virions, they must contain a number of intracellular components that the virus needs for its replication. The ability of a virus to enter and replicate in a particular type of cell is called tissue or cell tropism. Many cell receptors are proteinaceous in nature, but they can also be composed of carbohydrates or lipids. The identification of receptors for specific viruses is very important because it facilitates antiviral therapy. The presence of a receptor molecule is required for most viruses to complete the entry phase of the replication cycle. There is probably a complex of interactions between different functional regions of viruses and receptors. These interactions often induce conformational changes in the surface proteins of the virus and form regions that are necessary for their penetration. Thus, the binding receptor may not be the only cause of tropism and the adsorption process may be influenced by factors such as virus strain, cell type, and even multiplicity of infection.

Entry of the virus into the cell (penetration)

Entry of the virus into the cell occurs immediately upon attachment and, unlike adsorption, requires energy and does not occur at 0°C. The speed of this phase of the replication cycle varies between different viruses, with some entering the cell in less than a second and others taking several minutes. Moreover, the efficiency of the process varies from roughly 50% of surface-attached viruses successfully entering the cell to less than 0.1%. In enveloped viruses, penetration occurs by membrane fusion catalyzed by fusion proteins in the viral envelope. Protein fusions that caused entry were divided into two categories.
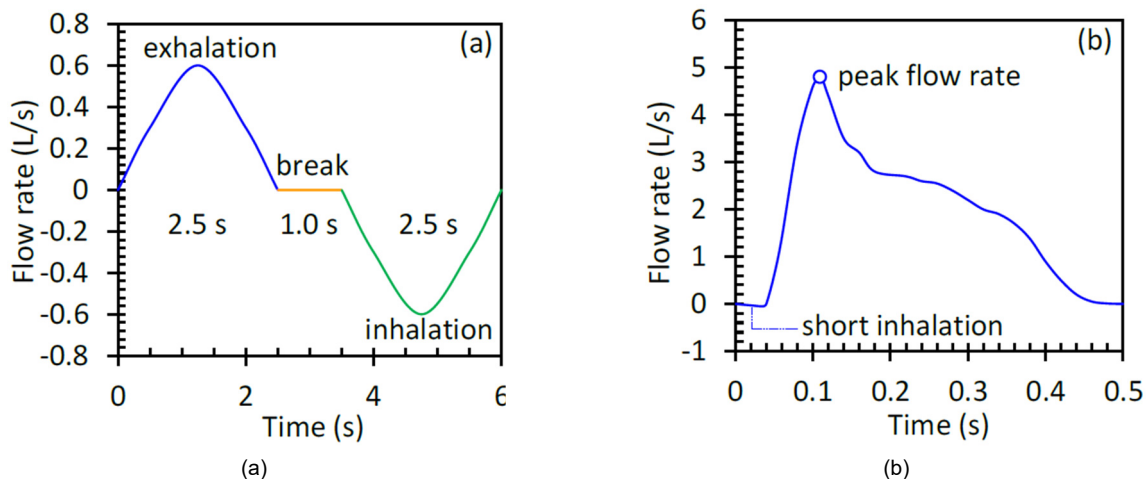
Figure 4. Accelerated breathing: (a) normal breathing process and (b) coughing process (modified from [18]).

Class I fusion proteins are trimeric spikes protruding from the surface of the viral particle and characteristically contain a fusion peptide composed of 20 hydrophobic amino acids. In some cases, such as HIV, fusion occurs in the cell at neutral pH with an activation energy ensuring receptor binding. In other cases, receptor-mediated endocytosis occurs.

Class II fusion proteins have distinct structural features and consist of heterodimers. Virus entry by endocytosis may be dependent on regions of the cell membrane that are rich in cholesterol and lipids. For many non-enveloped viruses, the mechanism of penetration through the host cell membrane in the absence of fusion is unclear. Recent findings suggest that such viruses can induce conformational changes in the membrane, resulting in the release of short membrane-interacting peptides. These break the membrane, allowing the virus to enter the cell.

Clustering and releasing replications

After the synthesis of viral proteins and viral nucleic acid, there is a replication assembly phase called morphogenesis. In general, the components that will form new virions are produced in large quantities and the assembly process is likely to be quite inefficient. This is followed by the release of replicated viral particles, i.e. the product of infection. Release is either through cell membrane rupture, as is typical of many non-enveloped viruses, or by penetration without cell destruction, as is typical of many enveloped viruses. Recently, some non-enveloped DNA viruses encoding a small basic regulatory protein (agnoprotein) whose function is to cause membrane permeabilization and subsequent release of newly synthesized viral particles have also been demonstrated. In some cases, viruses can be transferred directly from an infected cell to a neighboring cell, thereby avoiding any influence from the host's extracellular environment. Release without destruction of the cell membrane takes place by fusion of the viruses with the plasma membrane. The envelope of glycoproteins given by the type of virus is synthesized by essentially the same mechanism as the cell membrane. The viral proteins to become the envelope contain a sequence of 15–30 hydrophobic amino acids known as the signal sequence. This sequence allows the virus to pass through the cell membrane. Up to several thousand replicating virus particles can be produced in a single infected cell, although this number varies widely with the type of virus and the type of host cell. The virus release process requiring membrane destruction is significantly faster. In general, few of the newly formed virus particles are infectious. Most probably they do not have the right composition of proteins, enzymes and nucleic acids, or are defective.

SPREAD OF VIRUSES

Viruses are generally spread by direct contact of people, animals and birds or indirectly by contact with contaminated surfaces, water, food and inhalation of contaminated air. Viral cores of respiratory droplets can remain suspended in the air for longer periods of time and be transported over longer distances by air currents. The mean free path of air molecules $\lambda = 72$ nm is very similar to the diameter of a virus, which increases the probability of molecular collisions. It is usually appropriate to also specify whether the spread of droplets occurs by breathing or coughing, as both processes have different kinetics (Fig. 4) [18].

Human breathing processes are highly dynamic (see Fig. 4). A typical breathing cycle includes a 2.5 s inhale, a 2.5 s exhale, and a 1 s hold. Within the respiratory cycle of an infectious airflow from an infected individual, only 2.5 s are exhaled during a 6 s cycle, while for an exposed individual there is still only 2.5 s inhalation of infectious airflows after a cleaning phase of 2.5 s exhalation and 1 s delay [18]. Lindsley et al. [11] measured the incidence of influenza virus in droplet nuclei produced by a coughing patient and reported that 42% of detected viruses were found in droplet nuclei <1 μm, 23% in droplet nuclei 1-4 μm, and 35% in droplet nuclei >4 μm. These dimensions determine the amount of
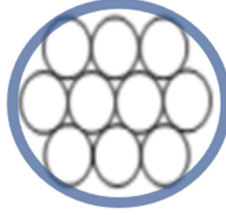
Figure 5. Idealized maximal honeycomb arrangement of a virus in a water droplet (blue envelope).

Table 1. Physical properties of water (see https://www.britannica.com/science/water/Physical-properties).

Dipole moment	2.95 ± 0.2 Debye
Boiling point	100°C at 101.325 kPa
Isothermal compressibility	0.4599 GPa^{-1}
Density	997.05 kg/m^3
Dielectric constant	78.4
Diffusion coefficient	2.27×10^{-9} m^2/s
Enthalpy of vaporization	40.657 kJ/mol (100°)
Electronic polarizability (liquid)	1.48 Å^3
Specific heat capacity (C_p)	75.327 J/mol/K
Specific heat capacity (C_v)	74.539 J/mol/K
Thermal conductivity	0.610 W/m/K
Dynamic viscosity	0.8909 mPa·s

viruses that can be contained in one droplet. The diameter of a droplet enveloping closely spaced circular cross-section viruses can be predicted from idealized structural arrangements. A simple idealized model assumes of a limiting honeycomb arrangement of viruses in the cross-section of a water droplet. In a tight honeycomb structure, the viruses are ideally arranged in hexagonal concentric layers (Fig. 5).

In the first concentric layer of this structure there is only one virus, in the second layer there are 6 viruses and in the i-th layer (i = 2,3,…) the number of viruses is equal to n_i = 6 (i - 1). The total number of ideally arranged viruses in l layers is equal to n = 3 l^2 - 3 l + 1. The number of layers l_n in a tight honeycomb structure is related to the total number of viruses n and the diameter of the aqueous envelope D_v. It holds that

$$l_n = 0.5 + \sqrt{\frac{n}{3} + \frac{1}{12}}, \qquad (1)$$

and

$$D_n = 2d\left[\sqrt{\frac{n}{3} + \frac{1}{12}} - 0.5 + 1/(2\cos 30°)\right]\sqrt{3\cos 30°/\pi}, \qquad (2)$$

where d is the diameter of the virus. From the knowledge of the size of the droplet and the diameter of the virus, it is possible to determine their theoretical maximum number in one droplet. In reality, the number of viruses will probably be much smaller. Most calculations and simulations apparently also use the idealized assumption that there is only one virus (diameter around 100 nm) in a spherical water droplet (diameter around 4 µm), so that the droplet behaves like normal water droplets without a virus. A summary of the physical properties of water is given in Tab. 1

For an isolated water molecule (e.g., water in the gas phase), the HOH bond lengths are 0.095718 nm and the HOH bond angles is 104.474°. In the liquid state, both of these values are slightly modified by water-water and water-virus interactions. The dipole moment of one water molecule in the liquid state at 300 K is 2.95±0.2 Debye (1 Debye = 3.336×10^{-30} Coulomb·m). The characteristics of respiratory flows, especially the speed and direction of exhalation flows, are strongly influenced by the geometry of the mouth and nose. The area of the mouth opening ranged from 100 mm^2 to 123 mm^2 during normal breathing, but exceeded 300 mm^2 during coughing. [12]. The total surface area of the nostrils during normal breathing varied widely, from 100 to 226 mm^2, and was predicted to be 330 mm^2 during coughing [12]. In real tests on humans, it was found that during coughing, the area of the mouth opening is 400 ± 95 mm^2 in men and 337 ± 140 mm^2 in women [13]. With regard to breathing mode, mouth-exhaled flow is important for both infected and exposed individuals [14]. Air flow exhaled through the mouth of an infected individual can easily penetrate the breathing area of a nearby individual. However, exhaled air flowing through the mouth of an exposed individual has a cleansing effect on the breathing area. Thus, the highest exposure is when the infected individual exhales through the mouth and the exposed individual exhales through the nose, while the lowest exposure is when the infected individual exhales through the nose and the exposed individual exhales through the mouth. Most computer fluid dynamics (CFD) studies simulate the "breath-only" mode for the

exposed individual and the "exhale-only" mode for the infected person [14, 15].

The well-known Wells-Riley model (see Eqn. 3) was developed to estimate the probability (*P*) of airborne transmission of an infectious agent in an indoor environment [16].

$$P = 1 - \exp\left(-\frac{Ipqt_0}{Q}\right)d, \qquad (3)$$

where *I* is the number of infected individuals, *p* is the respiration rate per person, *q* is the quantum rate of generation by the infected individual (quanta/s), that is the total exposure time t_0, and *Q* is the outdoor air supply rate. The quantum is equal to the infectious dose. This model has been widely used to assess the risk of airborne cross-infection. Another characteristic is the reproduction number (RAO), which is the number of secondary infections that arise when there is one infected individual in a population in a shared indoor environment [17]

$$R_{A0} = (n-1)\left[1 - \exp\left(-\frac{\bar{f}qt_0}{n}\right)\right], \qquad (4)$$

where *n* is the number of people in the ventilated space and $\bar{f}$ is the volume fraction of inhaled air that is exhaled by an infected person. The SARS-COV-2 virus primarily spreads through the air enveloped in water droplets [3]. It is mainly transmitted from infected persons by aerosol created by breathing and talking (up to 1.5 m), coughing (up to 2 m) or sneezing (up to 8 m). The droplet size ranges from 0.6 to 16 microns, but since it is a liquid, it can take any shape (the limit is the size of the virus) to allow penetration through porous hydrophobic materials. Air speed during inhalation and exhalation is around 80 km/h. When coughing and sneezing, it is up to 300 km/h. The volume of the lungs is about 5–6 liters [6]. Air consumption at different respiratory loads: at rest 8-10 l/min, walking 15-20 l/min, accelerated movement 20-30 l / min, medium load 30-40 l/min, high load 40-50 l/min, extreme load 50-120 l/min. It is therefore evident that the presence of aerosols containing viruses in the air leads to rapid infection without protection. Respiratory droplets can be of different sizes and are commonly classified as aerosols (droplets that are smaller than 5 μm) and droplets (that are larger than 5 μm). Although the behavior of these droplets largely depends on environmental factors such as humidity, temperature, etc., in general, larger droplets settle due to gravity and do not spread over distances greater than 1−2 m. However, aerosols remain in the air for a longer time (due to their small size) and play a key role in the spread of infection. Due to ambient conditions, the water phase may evaporate or interact with impurities in the air, viruses may settle on these impurities and further spread on a solid surface or independently. Standard types of dirt such as dust and exhalation products are increasingly supplemented by micro- and nano-plastics [7,10], which, due to their hydrophobicity, can form surfaces on which viruses can be deposited. Due to their size and mass, droplets and aerosols settle under the influence of gravitational forces. It is known that the ratio between the sedimentation rate (proportional to dp^2) and the Brownian motion (proportional to $dp^{-1/2}$) changes due to the influence of the particle size dp, as can be seen from Fig. 6.

If there is a situation where the viruses are alone in the air, they will settle down very slowly and therefore remain in the air for a long time. This situation occurs by removing the water phase either by evaporation (depending on the air temperature) or by contact with dirt in general and other surfaces. When evaluating the protective properties of fiber structures, a situation may arise when it is a liquid water particle containing a solid virus (the geometry changes easily) or when it is a solid particle with a surface-bound virus (the geometry does not change) with dimensions in the order of units of micrometers.

The virus is also transmitted by direct contact with the surfaces on which it is deposited. The virus can remain viable and infectious in aerosols for many hours and on surfaces (especially polymeric) for up to several days. So far, a practically unsolved problem is the limitation of virus attack from the surface of clothing textiles, especially due to direct infiltration by droplets spread from infected persons.
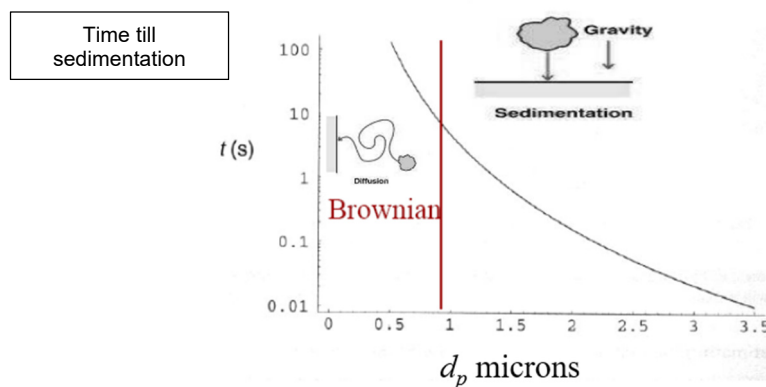

Figure 6. Effect of particle size on time to sedimentation.

Figure 7. Water droplets on the surface of (a) hydrophobic fiber layers, (b) hydrophilic fiber layers (modified from [20]).

CAPTURE OF PARTICLES BY A FIBROUS LAYER (FILTRATION)

A mechanical protective layer capable of stopping the spread of the virus should ideally have pores smaller than the minimum size of the virus (from 50 nm), especially in the case of its small thickness (for continuous electrospun nanofibrous layers on Nanospider device, it is approximately 2 micrometers thick). The required pore size cannot be achieved using standard nanofibrous layers, where the pore size distribution is usually from nano to micrometers with a broad maximum in the region of several tens of microns. By further layering individual nanofibrous layers, it is possible to create a system with a much narrower pore size distribution [19]. In the case of larger material thicknesses, the curvature of the pores will play an important role, because viruses penetrating through can be deposited on the walls of the pores. Hydrophobic polymers are usually used as the material of the protective layer, when in contact with a porous surface spherical droplet are formed, which are more difficult to penetrate the pores (Fig. 7(a)) and are removed by movement over the surface.

On the other hand, the presence of hydrophilic fibers enables surface spreading of the droplets (Fig. 7(b)). In work [20], a new reusable two-layer fiber filter consisting of electrospun superhydrophobic poly(methyl methacrylate)/polydimethylsiloxane as a barrier for moisture penetration and super hydrophilic chitosan fibers for effective deposition of particles with high filtration efficiency was proposed. Surface interactions with water droplets influence the separation processes of viruses, which then behave as solid nanoparticles during filtration. The main mechanisms of filtration are therefore based on the removal of the carrier medium, capture and deposition, or absorption of particles. The removal of particles depends on the structure of the protective layer (fiber diameter, pore size and spatial distribution of fibers), particle size, air flow parameters (at the nanoscale it is practically exclusively laminar flow), etc. The capture mechanisms are mainly influenced by the size of the filtered particles. The mechanical mechanisms of particle contact with the fibers act as deviations of the particle trajectory from the air currents around the fibers

Inertial shock (<u>impaction</u>) is caused by the inertia of the particles and is the dominant process for relatively large particles that are unable to quickly adjust their direction to changes in the direction of the streamlines. In this case, the particles hit the surface of the fiber directly. Entrapment (<u>interception</u>) can occur when the particles are not far enough from the fiber surface and the particle radius is greater than the distance between the streamlines and the fiber surface. When the particle changes its original path due to sufficient kinetic energy sufficient for Brownian motion, chaotic <u>diffusion</u> begins, increasing the probability of contact with the fiber surface. Capture also occurs through <u>electrostatic attraction</u> between the particles and the filter medium. The mesh deposition mechanism is only relevant for particles whose size is larger than the filter pore size. For particles below 100 nm in size, random Brownian motion can drive the trajectory and capture is a consequence of random collisions with fibers. The primary mechanism of particle deposition on the surface of fibers is physical sorption, where intermolecular interactions between fibers and particles occur, such as van der Waals interactions, London interactions, hydrogen bonds, etc. The filtration efficiency due to Brownian diffusion η_d can be expressed by the relation [21]:

$$\eta_d = 1.6 \left(\frac{1-\alpha}{K}\right)^{1/3} Pe^{-2/3}, \tag{5}$$

where $\alpha = 1 -$ porosity, is packing density of the fibrous structure and

$$K = -\frac{1}{2}\ln\alpha - \frac{3}{4} + \alpha - \frac{1}{4}\alpha^2. \tag{6}$$

The Pecelt number Pe is defined as

$$Pe = \frac{Ud_f}{D}, \tag{7}$$

where d_f is the fiber diameter, U is the air velocity and D is the diffusion coefficient

$$D = \frac{Tk_B C_S}{3\pi\mu d_p}, \tag{8}$$

k_B is the Boltzmann constant, T is the absolute air temperature, μ is the dynamic air viscosity, d_p diameter of the diffusing particles and C_s is the Cunningham correction factor defined as

$$C_S \approx 1 + 2.52\frac{\lambda}{d}, \tag{9}$$

where d is drop diameter and λ is the mean free path of the air (λ = 0.072 μm).

It can be seen that the filtration efficiency for capturing viruses (solid particles) is dependent on the, the diameters of the particles and the porosity of the protective fibrous layer.

INTERACTION OF PARTICLES WITH POROUS SURFACES

The physics of the impact of liquid droplets on surfaces depends on their type. There are two cases:

a) the impact and spread of droplets on an impermeable substrate,

b) impact and liquid penetration into the porous material due to impact energy and capillary forces.

When a drop hits a substrate, all of the drop's kinetic energy is converted to surface energy of the droplet deforming or dissipated by overcoming viscous forces. The relationship between the equilibrium contact angle θ_{eq} (formed by the droplet with the surface) and the surface tension is given by Young's equation $\gamma_{SV} = \gamma_{SL} + \gamma \cos(\theta)$, where γ_{SV} is the solid-gas surface tension (energy per unit area equivalent to force per unit length acting on the contact line), γ_{SL} is the solid-liquid surface tension and γ is the liquid-gas surface tension. Kinetic energy forces a liquid droplet to spread across a solid surface and also pushes it into pores in a permeable substrate. The droplet spreading kinetics can be expressed by the empirical Tanner model $R(t) = R_1 t^n$ where $R(t)$ is the radius of the droplet at time t, R_1 is the radius of the droplet at time t = 1 s and n is a parameter dependent on the quantities significantly affecting the spreading process (viscosity, buoyancy, gravity, surface tension). A value of n = 1/10 was found for viscous spreading of small droplets. When a drop of diameter d hits a solid surface (especially hydrophilic, with a sharp contact angle), it spreads radially until it reaches a maximum spread D_m (see Fig. 8).

If the droplet does not break up, the droplet/substrate interaction can be divided into three phases: expansion, contraction, and equilibrium. These processes are illustrated in Fig. 9, where the ratio D^* = D_m/d is plotted as a function of time.

The drop may shrink and after a few oscillations reach an equilibrium shape on the surface or it may spray and break up into small droplets or it may bounce off the surface. The final result of the drop impact depends on the impact speed of the drop, the size of the drop, the liquid and the properties of the surface including surface tension and surface roughness. To characterize the impact conditions, the Weber number is used:

$$W_e = \frac{\rho D V^2}{\gamma}, \qquad (10)$$

where ρ is the density of the liquid (water), V is the impact velocity, D is the diameter of the droplet, γ is the surface tension, and μ is the viscosity of the liquid. To calculate the droplet expansion ratio D_m^*, the following relation can be used:
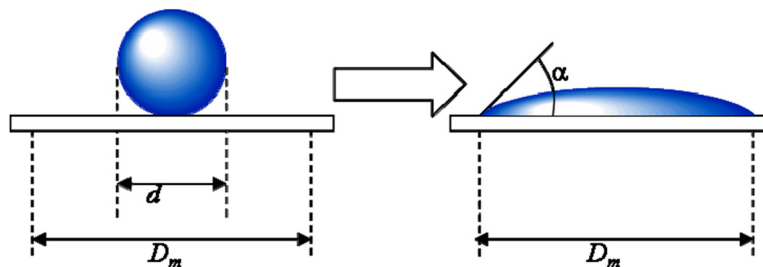
Figure 8. A drop of water on a hydrophilic surface (modified from [23]).
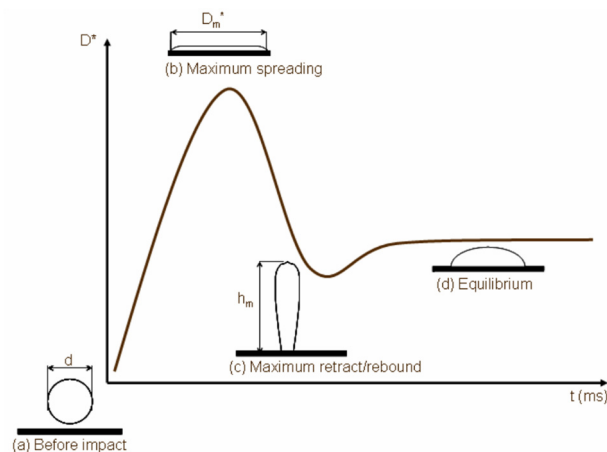
Figure 9. Phases of droplet interaction with a solid hydrophilic surface (modified from [23]).

Figure 10. Kinetics of spreading of water drops on polyester fabric: (a) time 2 s, (b) time 120 s and calculated contour.
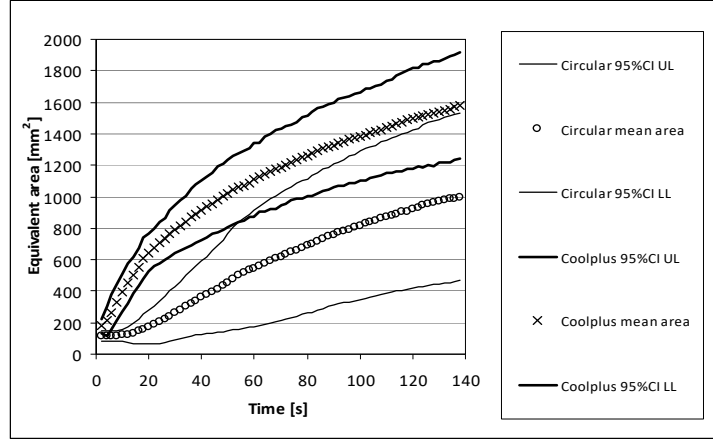
Figure 11. Dependence of equivalent areas on time, for "circular" and "Coolplus" samples.

$$D_m^* = 1 + 0.48 W_e^{0.5} exp\left[-1.48 W_e^{0.22} R_e^{-0.21}\right], \tag{11}$$

where R_e is Reynolds number defined as:

$$R_e = \frac{VD\rho}{\mu}. \tag{12}$$

Whether the drop bounces or not depends on the ratio D_m^* and the equilibrium contact angle θ. The resulting equation for predicting this phenomenon has the form:

$$E_{ERE}^* = \frac{1}{4}\left(\frac{D_m}{d}\right)^2 (1 - \cos\theta) - 0.12\left(\frac{D_m}{d}\right)^{2.3} (1 - \cos\theta)^{0.63} + \frac{2}{3}\left(\frac{D_m}{d}\right)^{-1} - 1. \tag{13}$$

The drop will bounce if E^*_{ERE} is greater than zero. At small R_e, the impact of a droplet on a solid surface results in its spreading (kinematic impact phase). The spreading radius of the droplet increases with time t according to the relation $R \sim t^{1/2}$ independently of the physical properties of the liquid and the surface. As R_e increases, droplet impact results in repeated reflections and especially splashing.

When studying the impact of drops on a porous substrate, its hydrophilicity, or hydrophobicity (characterized by $\cos\alpha$ or equilibrium contact angle θ) is manifested

As the porosity of the substrate increases, the liquid tends to penetrate more into the structure. An increase in porosity reduces the capillary pressure and reduces the force that draws liquid into the pores [22]. Increasing R_e increases the spreading rate of droplets on the substrate surface, thereby shortening the time scale for penetration. At the same time, the inertia of the fluid penetrating into the porous substrate increases [22]. As Weber number We decreases, the effect of surface tension becomes more important. Capillary forces in the porous substrate increase, and a greater degree of penetration occurs. At the same time, the spread of the drop on the surface of the substrate is reduced due to the larger volume of liquid penetrating the substrate. Decreasing the value of the contact angle promotes wettability of the surface and greater penetration. The higher the wettability, the greater the liquid penetration, and the capillary pressure tends to draw the liquid more into the porous substrate. To monitor the kinetics of the spread of droplets on a porous surface, image analysis can be used, enabling the quantification of the outline of the droplets over time (see Fig. 10).

A MATLAB program (name DROP) was created to identify real contours. Equivalent perimeters P_i and areas S_i were calculated from contour coordinates. The equivalent radius of a spread water droplet RP_i based on the assumption that the real contour is replaced by a contour of a circular shape with the same circumference is given by the relation $RP_i = P_i/(2\pi)$ and the equivalent radius of a spread water drop RS_i assuming that the real contour is replaced by the contour of a circular shape with the same area, is calculated from the relation $RS_i = \sqrt{(S_i/\pi)}$. For illustration, Fig. 11 shows the time dependence of the equivalent areas of water drops on samples of

polyester textiles from Coolplus fibers and fibers with a circular cross-section.

It has been confirmed that the cross-sectional shape of the fiber in the fabric has a significant effect on the kinetics of water droplet propagation due to microcapillary distribution. The ANSYS system and an idealized structure with regular cylindrical holes were used to simulate the spread of water droplets on the surface of a porous substrate associated with penetration into the pores. The results were compared with real structures containing regular cylindrical holes [22]. It was found that water droplets falling on a flat surface with small diameter drilled holes penetrated the holes on a time scale that was significantly longer than the droplet impact time. Liquid penetration into the holes was initially rapid, driven by the inertia of the impinging liquid. When the droplet reached its maximum extension and began to bounce, the inertia-driven motion was stopped. The subsequent flow of liquid into the holes was much slower, caused by capillary forces drawing the liquid in. A simple model accounting for fluid pressure, surface tension, and viscous forces predicted fluid velocity in both inertial and capillary-driven regimes [22].

PROTECTIVE FIBROUS STRUCTURES

Protective fibrous layers that are truly effective for trapping viruses are significantly different from conventional textile layers that trap liquid aerosols. These are mostly nano assemblies prepared by electrospinning (Fig. 12(a)) or non-woven textiles created by a combination of melt blown and electrospinning techniques (Fig. 12(b)) used for masks for prevention - RP and for masks for environmental protection – RO [2]. The improvement of filtration characteristics of these layers can be achieved by the appropriate choice of their structural parameters, which include fiber diameter, ratio of micro and nano fibers, thickness, porosity and areal mass.
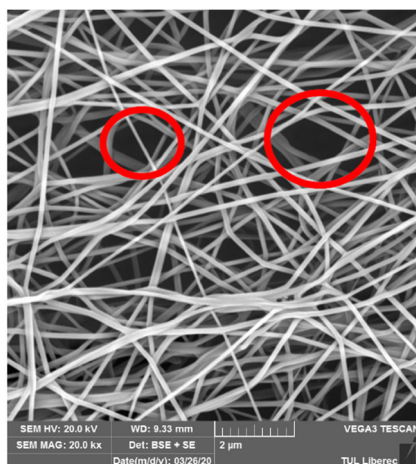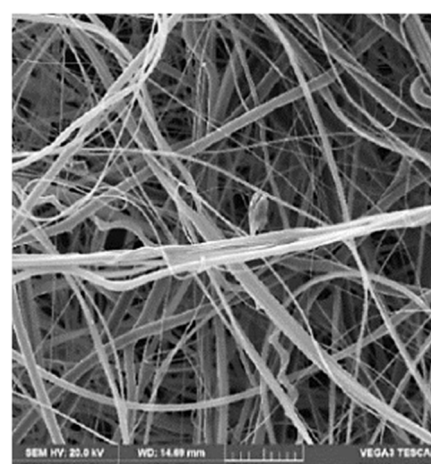
A wide distribution of pore sizes is evident although the average pore size is acceptably small. To optimize such structures, the pore structure needs to be controlled, which includes not only the overall porosity and pore size distribution, but also their 3D shape and tortuosity. A number of experimental techniques such as scanning electron microscopy (SEM), pycnometer, mercury porosimetry, micro-computed tomography (micro-CT) [24] and, most recently, 3D confocal laser microscopy [25] are available to evaluate the pore structure.

Fig. 13 shows for illustration the procedure of analyzing the pore distribution from real SEM images of one nonwoven structure using the image analysis toolbox of the MATLAB program system. It uses adaptive thresholding (Otsu) and the regionprops() function.

The advantages and disadvantages of experimental approaches are examined in detail in [25]. Theoretical models can predict the pore structure of fiber structures with some morphological and structural parameters determined from real materials. For nanostructures forming short fiber sections, the average section length can also be easily determined experimentally and used in a geometric model.

The following idealized assumptions were used in the work [26] to construct the geometric model of the nanofiber entanglement:

1. All fibers (or fiber sections) are approximated as straight cylinders with diameter $d = \omega$ and length $l = \lambda$.
2. The probability that a point in the network plane has coverage c corresponds to the Poisson distribution.
3. The segments in the tangle of nanofibers are placed in arbitrary positions in the XY plane, neglecting the orientation in the direction of the Z axis.
4. The location of the fibers in the XY plane follows a Poisson random process.

(a)

(b)

Figure 12. Structures for face masks (a) classic nano mesh (b) combination of micro fibers and nano fibers (melt blown and nano mesh) [2].
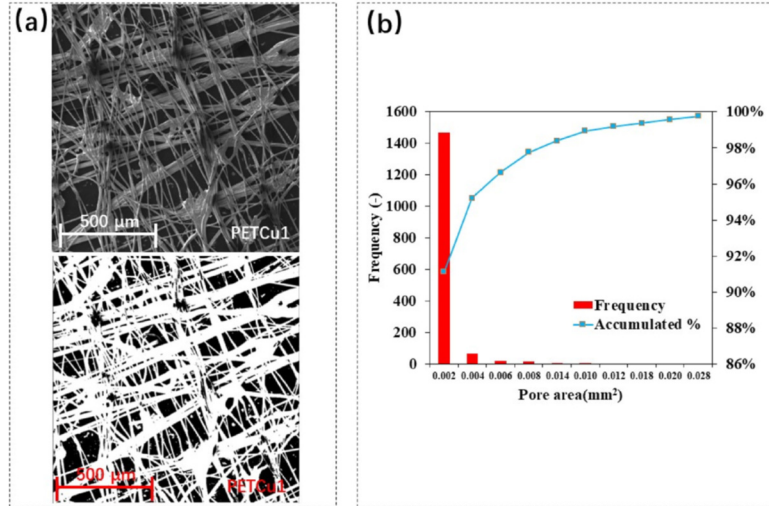
Figure 13. Pore distribution analysis (a) conversion of SEM image to binary image to display pore shape (b) pore size frequency plot.

By knowing the structural and morphological parameters of the nanofibrous structure, including the mean fiber diameter ω, porosity ε and thickness t, its expected average number of fiber contacts can be determined and the mechanical properties, pore size, and their distribution can be calculated. For mean value and variance of the pore radii in the elementary layer, the following relations can be derived [26]:

$$\bar{r} = \frac{\omega\sqrt{\pi}}{4}\left(\frac{1}{4\log\left(\frac{1}{\varepsilon}\right)} + \frac{2A}{\pi}\right) \qquad (14)$$

and

$$\delta^2(r)\left(\frac{1}{\pi} - \frac{\pi}{16}\right)\left[\left(\frac{1}{4\log\left(\frac{1}{\varepsilon}\right)} + \frac{2A}{\pi}\right)\omega\right]^2, \qquad (15)$$

here A is the ratio of the length and thickness of the fiber segments:

$$A = \frac{\lambda}{\omega}. \qquad (16)$$

Assuming that the distribution of pore radii r in an elementary layer can be modeled using a gamma distribution, Sampson [27] derived the probability density and distribution function of the pore radius r in this layer:

$$f(r) = \frac{b^k}{\Gamma(k)}r^{k-1}e^{-br}, \qquad (17)$$

where $\Gamma(k)$ is a gamma function with parameter k.

The probability density of pore radii in a nanofibrous structure formed by the superposition of n layers was derived assuming that each subsequent layer with independent and identical distribution of pore radii is placed over the previous layer such that the centers of the pore pairs in the layers are the same. For such a pair of layers, the radius of the smaller pore is assigned to each pair of pores. With this assumption, the probability density of the pore radii distribution of the multilayer nanofibrous assembly is:

$$f(r,n) = n\left(\frac{\Gamma(k,(br))}{\Gamma(k)}\right)^{n-1}f(r), \qquad (18)$$

where $\Gamma(k,br)$ is an incomplete gamma function with parameters k, br that can be determined from the

relations for mean value and variance of the pore radii:

$$\bar{r} = \frac{k}{b}, \quad \delta_x^2(r) = \frac{k}{b^2}. \qquad (18)$$

The shape factor k characterizes the coefficient of variation CV of the pore radii in percent, i.e. $k = 1/CV^2$, where CV for random structures is usually $CV = \frac{1}{\pi}\sqrt{16 - \pi^2}$. A simple choice is $CV = 3$ based on approximate normality. The scale factor b is then simply calculated from the knowledge of the average pore radius from Eq. (19). To calculate the total porosity ε, a relationship based on the ratio of the density of the nanofibrous assembly (areal weight of the assembly divided by its thickness) and the density of the polymer forming the assembly is usually used. In [28] was nanofibrous assembly simply assumed as solid straight rods having length L (usually more than 10 mm) diameter d and linear density J defined as:

$$\bar{r} = \frac{k}{b}, \quad \delta_x^2(r) = \frac{k}{b^2}. \qquad (19)$$

The shape factor k characterizes the coefficient of variation CV of the pore radii in percent, i.e. $k = 1/CV^2$, where CV for random structures is usually $CV = \frac{1}{\pi}\sqrt{16 - \pi^2}$. A simple choice is $CV = 3$ based on approximate normality. The scale factor b is then simply calculated from the knowledge of the average pore radius from Eq. (19). To calculate the total porosity ε, a relationship based on the ratio of the density of the nanofibrous assembly (areal weight of the assembly divided by its thickness) and the density of the polymer forming the assembly is usually used. In [28] was nanofibrous assembly simply assumed as solid straight rods having length L (usually more than 10 mm) diameter d and linear density J defined as:

$$J = \frac{\pi d^2 \rho}{4}, \qquad (20)$$

where ρ is (volumetric) density of fibrous elements. The nanofibrous assembly is characterized by porosity Po defined usually as:

$$Po = 1 - \frac{\rho h}{w}, \qquad (21)$$

where h is nanofibrous assembly thickness and w is corresponding areal density. Let in this simplified nanofibrous assembly the location of nanofibrous segments centers follows Poisson process in two dimension and are independent each other. The orientation distribution of nanofibrous segments in selected direction is described by uniform distribution (in details see ([28]). The mean coverage Co of this nanofibrous assembly can be expressed by relation:

$$Co = \frac{wd}{J}. \qquad (22)$$

The probability that a point in this nanofibrous assembly has coverage Co is given by the Poisson distribution with parameter Co. Under these assumptions is porosity related to mean coverage according to relation:

$$Po = \log\left(\frac{1}{Co}\right). \qquad (23)$$

For porosities greater that 0.3, the mean pore diameter R_m of this nanofibrous assembly can be computed from relation:

$$R_m \approx \frac{\sqrt{\pi}}{4}\left(\frac{\pi}{2\log\left(\frac{1}{P_0}\right)} - 1\right) d. \qquad (24)$$

Based on these relations the nanofiber diameter and surface porosity of PAN nanofiber mats were studied ([29]). The results showed that increasing the PAN polymer concentration enhanced the nanofiber diameter but reduced the surface porosity of nanofiber mats. Because the diameter and in surface porosity are parameters that possess mutual effects, a structural parameter (Q) was introduced, and then its relation to some of the physical characteristics, such as the air permeability and surface roughness, was investigated. These simplified models can predict the pore structure and morphology of nanofibrous assemblies prepared by electrospinning. The mean pore diameter and probability density of penetrating particles size can be simply used for prediction of penetration of submicron creatures and as well drops containing viruses (see [30]).

CONCLUSION

The solution of problems related to the protective function of fibrous structures against the penetration of viruses and droplets containing also enveloping liquid water was shown. An overview of appropriate mathematical models and the results of some simulation studies were presented, which allow the assessment of the suitability of these structures for real use. Due to the complexity of the problem, the solution was restricted mainly by a combination of mathematical and stochastic modeling, and the simulation was limited only to strongly idealized situations. The MATLAB software system was used for image analysis and simple analytical models building. The various aspects of antiviral actions and their applications for construction of active fibrous structures were published in book [1] and some articles [36-44] published in proceedings from conference TBIS devoted mainly to these topics.

REFERENCES

1. Militký J., Prince A., Venkataraman M. (eds): Textiles and Their Use in Microbial Protection. Focus on COVID-19 and other viruses, London: CRC Press Boca Raton, 2021.
2. Militký J., Novák O., Křemenáková D., et al.: A Review of impact of textile research on protective face masks, Materials, 14, 2021, 1937. https://doi.org/10.3390/ma14081937
3. Gericke, A., Venkataraman, M., Militky, J.; et al.: Unmasking the mask: Investigating the role of physical properties in the efficacy of fabric masks to prevent the spread of the COVID-19 Virus, Materials 14(24), 2021, 7756. https://doi.org/10.3390/ma14247756
4. Gericke, A., Militký, J., Venkataraman, M., et al.: The effect of mask style and fabric selection on the comfort properties of fabric masks, Materials 15(7), 2022, 2559. https://doi.org/10.3390/ma15072559
5. Chua, M.H., et al.: Face Masks in the new COVID-19 normal: materials, testing, and perspectives. AAS Research, 2020, 7286735. https://doi.org/10.34133/2020/7286735
6. Dobiáš J.: Determination of substances in exhaled air condensate, Diploma Thesis, Hradec Králové: UK Hradec Králové, 2006.
7. Da Costa J.P., et al.: (Nano) plastics in the environment – sources, fates and effects, Sci Total Environ, 566–567, 2016, pp. 15–26. https://doi.org/10.1016/j.scitotenv.2016.05.041
8. Da Costa J.P.: Micro- and nanoplastics in the environment: Research and Policymaking, Current Opinion in Environmental Science & Health, 1, 2018, pp. 12–16. https://doi.org/10.1016/j.coesh.2017.11.002
9. Beaurepaire M., et al.: Microplastics in the atmospheric compartment, Current Opinion in Food Science, 41, 2021, pp. 159–168. https://doi.org/10.1016/j.cofs.2021.04.010
10. Gasperi J,. et al.: Microplastics in air: Are we breathing it in?, Current Opinion in Environmental Science & Health, 1, 2018, pp. 1–5. https://doi.org/10.1016/j.coesh.2017.10.002
11. Lindsley W.G, a kol.: Measurements of airborne influenza virus in aerosol particles from human coughs, PLoS One, 5, 2010, e15100. https://doi.org/10.1371/journal.pone.0015100
12. Zhu S.W., et al.: Study on transport characteristics of saliva droplets produced by coughing in a calm indoor environment. Build Environ., 41(12), 2006, pp. 1691-1702. https://doi.org/10.1016/j.buildenv.2005.06.024
13. Gupta J.K., et al.: Flow dynamics and characterization of a cough, Indoor Air., 19, 2009, pp. 517-525. https://doi.org/10.1111/j.1600-0668.2009.00619.x
14. Villafruela J.M., et al.: Influence of human breathing modes on airborne cross infection risk, Build. Environ., 106, 2016, pp. 340-351. https://doi.org/10.1016/j.buildenv.2016.07.005
15. Liu L., et al.: Short-range airborne transmission of expiratory droplets between two people, Indoor Air., 27(2), 2016, pp. 452-462. https://doi.org/10.1111/ina.12314
16. Riley E.C., et al.: Airborne spread of measles in a suburban elementary school, Am. J. Epidemiol, 107, 1978, pp. 421-432. https://doi.org/10.1093/oxfordjournals.aje.a112560
17. Cermak R., Melikov A.K.: Protection of occupants from exhaled infectious agents and floor material emissions in rooms with personalized and underfloor ventilation. HVAC&R Res., 13(1), 2007, pp. 23-38.
18. Ai Z. T., Melikov A.K.: Airborne spread of expiratory droplet nuclei between the occupants of indoor environments: A review, Indoor Air, 28(4), 2018, pp. 500 – 524.

https://doi.org/10.1111/ina.12465

19. Lee S., Obenorf K.: Use electrospun nanofiber web for protective textile materials as barriers to liquid penetration, Textile Research Journal, 77(9), 2007, pp. 696–702.
https://doi.org/10.1177/0040517507080284

20. Hui L., et al.: Transparent antibacterial nanofiber air filters with highly efficient moisture resistance for sustainable particulate matter capture, iScience 19, 2019, pp. 214–223.
https://doi.org/10.1016/j.isci.2019.07.020

21. Lee K.W., Liu B.Y.H.: Theoretical Study of Aerosol Filtration by Fibrous Filters, Aerosol Sci. Technol., 1(2), 1982, pp. 147–161.
https://doi.org/10.1080/02786828208958584

22. Hosseini S.: Droplet impact and penetration on to the structured pore network geometries, PhD Thesis, Toronto: University of Toronto, 2015.

23. Ok H.: Particle-laden drop impingement on a solid surface, PhD Thesis, Atlanta: Georgia Institute of Technology, 2005.

24. Ho S.T., Hutmacher D.W.: A comparison of micro CT with other techniques used in the characterization of scaffolds, Biomaterials 27(8), 2006, pp. 1362–1376.
https://doi.org/10.1016/j.biomaterials.2005.08.035

25. Bagherzadeh R., et al.: Three-dimensional pore structure analysis of nanomicrofibrous scaffolds using confocal laser scanning microscopy, J Biomed Mater Res Part A, 101A, 2013, pp. 765–774.
https://doi.org/10.1002/jbm.a.34379

26. Bagherzadeh R., et al.: A theoretical analysis and prediction of pore size and pore size distribution in electrospun multilayer nanofibrous materials, J Biomed Mater Res Part A, 101A, 2013, pp. 2107– 2117.
https://doi.org/10.1002/jbm.a.34487

27. Sampson W.W.: A multiplanar model for the pore radius distribution in isotropic near-planar stochastic fibre networks, J Mater Sci, 38, 2003, pp. 1617–1622.
https://doi.org/10.1023/A:1023298820390

28. Eichhorn J., Sampson W.W.: Statistical geometry of pores and statistics of porous nanofibrous assemblies, J. R. Soc. Interface, 2(4), 2005, pp. 309-318.
https://doi.org/10.1098/rsif.2005.0039

29. Borhani S., et al.: Structural characteristics and selected properties of polyacrylonitrile nanofiber mats, Journal of Applied Polymer Science, 108, 2008, pp. 2994–3000.
https://doi.org/10.1002/app.27904

30. Militký J., et al.: Penetration of mites through textile layer, In proceedings of: Int conf. Medical textiles 96. Bolton, 1996,

31. https://en.wikipedia.org/wiki/Severe_acute_respiratory_syndrome_coronavirus_2

32. Wu Z. et al.: Amino acid influence on copper binding to peptides, J Am Soc Mass Spectrom., 21(4), 2010, pp. 522–533.
https://doi.org/10.1016/j.jasms.2009.12.020

33. Van Doremalen N., Bushmaker T., Morris D.H.: Aerosol and surface stability of HCoV-19 (SARS-CoV-1 2) compared to SARS-CoV-1, MedRxiv, 2020.
https://doi.org/10.1101/2020.03.09.20033217

34. Tinoco, I. et al.: How RNA folds, Journal of Molecular Biology, 293, 1999, pp. 271–81.

35. Radke K., et al.: Viral interactions with the cytoskeleton: a hitchhiker's guide to the cell, Cellular Microbiology, 8(3), 2006, pp. 387–400.
https://doi.org/10.1111/j.1462-5822.2005.00679.x

36. Peng Q.-Y., Venkataraman M., Yang K., at al.: Kinetic model for disinfection with photo-oxidation. In: Text. Bioeng. Informatics Symp. Proc. 2020 - 13th Text. Bioeng. Informatics Symp. TBIS 2020, pp. 68-75, 2020.

37. Faheem S., Militky J., Wiener, J.: Characterization, indication and passivation of SARS-CoV-2, In: Text. Bioeng. Informatics Symp. Proc. 2020 - 13th Text. Bioeng. Informatics Symp. TBIS 2020, pp. 76-83, 2020.

38. Mahmood A., Militky J., Pechočiaková M., et al.: Eradicating spread of virus by photo-catalysis process, In: Text. Bioeng. Informatics Symp. Proc. 2020 - 13th Text. Bioeng. Informatics Symp. TBIS 2020, pp. 22-31, 2020.

39. Wang D., Hu S., Kremenakova D. et al.: Virology of SARS-CoV-2, In: Text. Bioeng. Informatics Symp. Proc. 2020 - 13th Text. Bioeng. Informatics Symp. TBIS 2020, pp. 49-55, 2020.

40. Hu S., Wang D., Yang K, et al.: Copper coated textiles for inhibition of virus spread. In: Text. Bioeng. Informatics Symp. Proc. 2020 - 13th Text. Bioeng. Informatics Symp. TBIS 2020, pp. 84-91, 2020.

41. Tan X.-D., Peng Q.-Y., Yang K., et al.: Influence of UV light and ozonization on microbes, In: Text. Bioeng. Informatics Symp. Proc. 2020 - 13th Text. Bioeng. Informatics Symp. TBIS 2020, pp. 159-166, 2020.

42. Khan M.Z., Militky J., Wiener J.: Enhanced disinfection of titanium dioxide, In: Text. Bioeng. Informatics Symp. Proc. 2020 - 13th Text. Bioeng. Informatics Symp. TBIS 2020, pp. 188-196, 2020.

43. Karthik D., Militky J., Venkataraman M.: Eradicating spread of virus by using activated carbon, In: Text. Bioeng. Informatics Symp. Proc. 2020 - 13th Text. Bioeng. Informatics Symp. TBIS 2020, pp.56-63, 2020.

44. Ali A., Militky J., Shahid M.: Copper based viral inhibition, In: Text. Bioeng. Informatics Symp. Proc. 2020 - 13th Text. Bioeng. Informatics Symp. TBIS 2020, pp.32-36, 2020.

This work is dedicated to prof. Izabella Krucińska from TU Lodz, who was not only a prominent scientific personality but also our close friend. A tribute to her memory.

A SUSTAINABLE APPROACH TO SEERSUCKER WOVEN FABRIC PRODUCTION: ELIMINATING ELASTANE AND DOUBLE BEAMS FOR NATURAL MATERIAL-BASED DESIGN

ASMA, AYÇIN[1]; BURGUN, ALPER[2]; DEMIREL, GIZEM[1*] AND BUDUN GÜLAS, SINEM[3]

1   Akın Tekstil AŞ, Design Centre, Kırklareli, Turkey
2   Akın Tekstil AŞ, Sales and Marketing Department, İstanbul, Turkey
3   İstanbul Aydın University, Fine Arts Faculty Textile and Fashion Design Programme, İstanbul, Turkey

ABSTRACT

Nowadays, the increasing social consciousness on the protection of nature and, at the same time, the seeking for comfort and easiness caused by the pandemic, increase the interest in easy-to-use, comfortable textile products produced with natural raw materials. Seersucker woven fabrics are highly preferred in recent years due to their features such as providing wearing comfort and being user-friendly by not requiring ironing. However, in order to provide the three-dimensionality/wrinkle effect in woven seersucker fabrics in the currently used methods, it is necessary to use elastane in the weft/warp or to use double beams during production. At this point, it is not possible to produce completely natural fabric in the method using elastane, and in the other method, a special several warp and machine requirements are emerging. In this study, the literature on seersucker fabrics was reviewed and experimental seersucker weaving applications were carried out. Studies have been carried out in order to produce fabrics using completely natural raw materials (cotton), to improve production efficiency and to increase design possibilities. In this context, instead of the traditional methods used in seersucker fabric creation, seersucker fabric production was carried out with a single beam on the weaving machine by using different weaves in the dobby for fabric design. In this way, it has been provided that the seersucker weaving process can be performed with a single beam on any desired machine by using existing direct warps without the need for a special warp preparation.

KEYWORDS

Woven Fabrics; Seersucker Fabrics; Elastane Free Seersucker Fabrics.

INTRODUCTION

Woven fabrics are generally considered flat (2D - two-dimensional) textile materials. The reason is that their third dimension, thickness, is negligibly small compared to the other two dimensions, length and width. However, there are also woven or knitted fabrics that are considered 3D (three-dimensional) or 2D+. A basic common definition of 3D fabrics is having a third dimension – fabric thickness/voluminosity [1,2].

Seersucker fabrics are thin, lightweight, comfortable fabrics with a striped appearance and a wrinkled, textured surface, usually produced by the combined use of cotton and synthetic yarns [3, 4]. Seersucker fabrics are the fabrics that have a three-dimensional appearance with their raised surface structures and some researchers qualify these fabrics as 3D fabrics [5].

It is possible to produce seersucker fabrics in both knitted and woven fabric production methods, but the subject of this study is woven seersucker fabrics. In Figure 1 and Figure 2, examples of woven and knitted seersucker fabric can be observed.

When their historical background is examined, it is seen that seersucker fabrics were traded by various companies in the East Indies in the 1600s [7]. However, it is understood from the written records of this period that "crimped" fabrics, which were woven with high twisted yarns and had a seersucker-like surface appearance, were traded in Anatolia in 1640 (Figure 3) [8, 9].
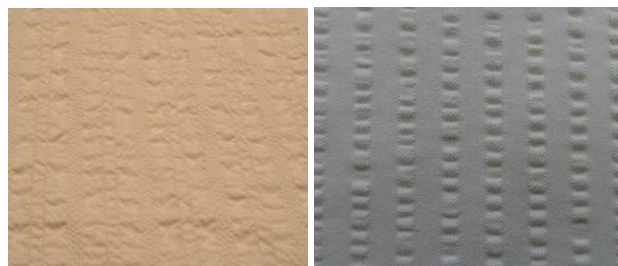

Figure 1. Woven seersucker fabric swatches [5,6].

Figure 2. Knitted seersucker fabrics swatches [2].

| (a) | (b) |

Figure 3. Examples of traditionally woven "crimped" fabrics in Anatolia [9] [10]. (Photograph (a): Servet Senem Uğurlu, 2006, Photograph (b): Dokuma Atlası, 2021).

Seersucker fabrics developed in Eastern countries were introduced to the Western world by Muslim merchants. When European men realized that seersucker was an ideal fabric for summer, it was quickly adopted in this region. It was very popular in the British colonies as it was a comfortable and lightweight fabric in hot climates and exuded elegance. After crossing the oceans, seersucker fabrics began to be accepted in America as fabrics that could be used by the workers after a while [7]. These fabrics, which were initially used for workers' clothes, started to be worn/preferred by people belonging to the upper class since the 20th century. Seersucker fabrics have become popular again today because of their casualness and good comfort properties. Garments produced with seersucker fabrics are expected to keep the wearer dry and cool, especially in the summer months when the weather is hot and humid. By creating a more modern and wrinkle-free alternative to linen, one of the most popular fabrics of summer, the demand for suit models suitable for comfort after the pandemic is increasing day by day. Seersucker fabrics support air circulation thanks to the fact that the flat parts remain in the air on the wrinkled surface and only the shirred part touches the skin. This characteristic allows the fabric to breathe. Therefore, the fabric has good moisture transport and thermal conductivity, making the wearer feel dry and cool. Another feature that increases its attractiveness is that it does not require ironing due to its wrinkled structure [11].

Since these fabrics are lightweight, have a wrinkled appearance, and in terms of their surface, they are heterogeneous, meaning they contain locally loose and compact sections of weaving, they are generally used in the production of summer clothing. Seersucker fabrics are ideal fabrics for the production of skirts, summer dresses, blouses and shirts [3,12].

The characteristic shirred stripe effect in woven seersucker fabrics is created by controlled tension variations in the warp sections during weaving, the use of yarns with different shrinkage properties or chemical finishes [13].

Numerous academic studies have been conducted to enhance the surface and comfort properties of seersucker fabrics due to their growing demand. The article by Lukazs et al. introduces a method for measuring the surface geometry of seersucker woven fabrics using laser techniques [5]. Fracczak et al. investigate the friction properties of seersucker fabrics based on their structure [16]. Matusiak's studies explore the structural, mechanical, and moisture transport properties of seersucker fabrics, as well as their comfort‐related characteristics [1, 12, 17, 18]. The research conducted by Matusiak and Bajzik focuses on surface characteristics and the effect of seersucker repetition on fabric parameters [14]. Furthermore, Matusiak utilizes non‐contact optical methods to investigate the surface geometry of seersucker fabrics [15].

Currently, several different methods are used in seersucker fabric production. Typically, a wrinkled effect is achieved on the fabric's surface through the combined weaving of two warp yarns with different tensions or by using weft and warp yarns with varying tensions. This creates tension differences that result in the desired wrinkle effect. [3, 4]. In the method where two warp beams with different tension are used, one beam carries the warp yarns that will form the flat (basic) strip appearance and the other beams carry the warp yarns that will form the shirred strip appearance. During the weaving process, the warp yarns that will create the shirred appearance are adjusted so that they are fed faster than the other warp yarns. This discrepancy in tension among the warp threads leads to localized wrinkling in the fabric, particularly in areas where fast‐feeding yarns are present. Consequently, the fabric surface exhibits both shrinked and flat strips running in the warp direction. This kind of shrinkage on the fabric surface

(a)   (b)   (c)
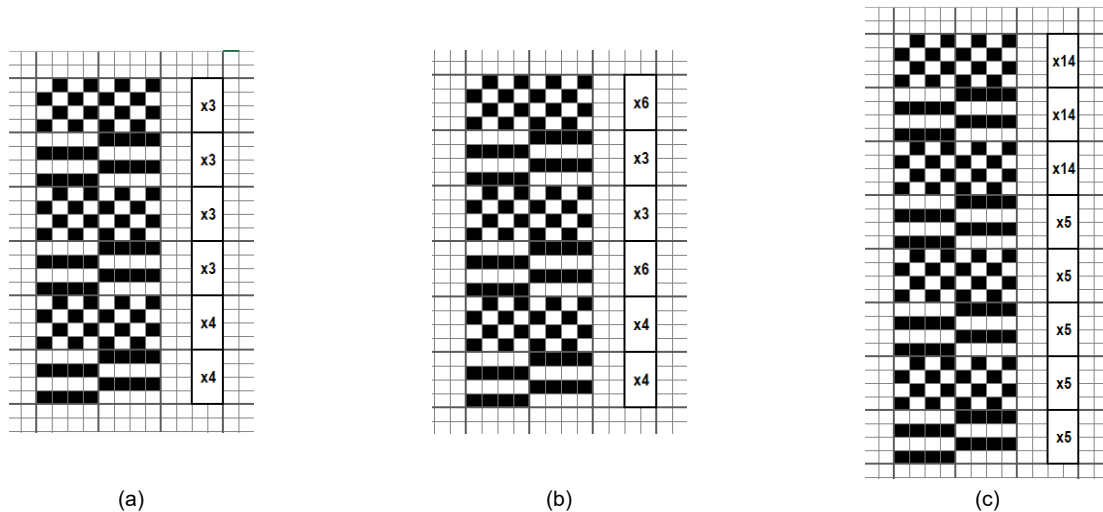
Figure 4. Design trials with different repeat regions: (a) D1, (b) D2 and (c) D3.

Figure 5. Fabric trials with different weave composition (Photograph: Ayçin Asma, 2022).

is called the seersucker effect. This type of fabric cannot be produced on conventional weaving looms with a single beam [4, 12]. For this method, a special weaving loom with two warp beams with separate tension control is required [3]. The use of elastane yarn in seersucker fabric production is also a method that has been widely used in recent years. Apart from these, seersucker effect can be created on fabrics with some finishing and printing processes after weaving [19].

In the study, it is aimed to produce fabrics with seersucker effect with completely natural raw materials without the necessity for double beam and without using elastane. In this context, fabrics using different weave values in dobby were designed, the trials of these designed fabrics on the template loom were carried out in the product design department of Akın Tekstil AŞ., and sample production was carried out for the model study in which the seersucker effect was obtained visually, and post-washing shrinkage, washing fastness, dry/wet rubbing and strength tests were applied.

EXPERIMENTAL STUDY

Design studies and hand loom texture trials

In the study, three different woven patterns were designed to give this effect on the fabric surface in order to create the seersucker effect. Various weaves were combined within the same design to achieve the desired waffle effect. Different repeat numbers were experimented within the design to determine the optimal weaving construction for a stronger puckering effect on the fabric surface. Figure 4 shows the weave plans of the prepared designs.

In the first design (D1), different weave regions have repeat numbers of x3 and x4, while in the second design (D2), the repeat numbers are x4, x6, x3, and x6. The third design (D3) exhibits higher repeat numbers compared to the first two examples, arranged as x5 and x14.

Trials of these three different patterns were produced on hand looms. Figure 5 illustrates the examples of fabric experimentations with different compositions.

As a result of the initial small-scale production, a puckering effect was observed on the fabric, leading to further production of larger samples (Figure 6). The fabrics produced with D1, D2, and D3 from the design trials (Figure 4) were coded as P1, P2, and P3, respectively.

Wrinkle effect was obtained on the fabric surface in all experiments. However, in one of them (P3), the weave pattern combination provided the most optimal waffle effect and a surface appearance having the surface appearance of the fabric produced by other conventional methods was obtained.

Industrial Development of Fabric

The fabric P3 (Fig. 6), which achieved the best result in terms of the desired seersucker effect, was industrially produced. It was woven using 12x1 tex
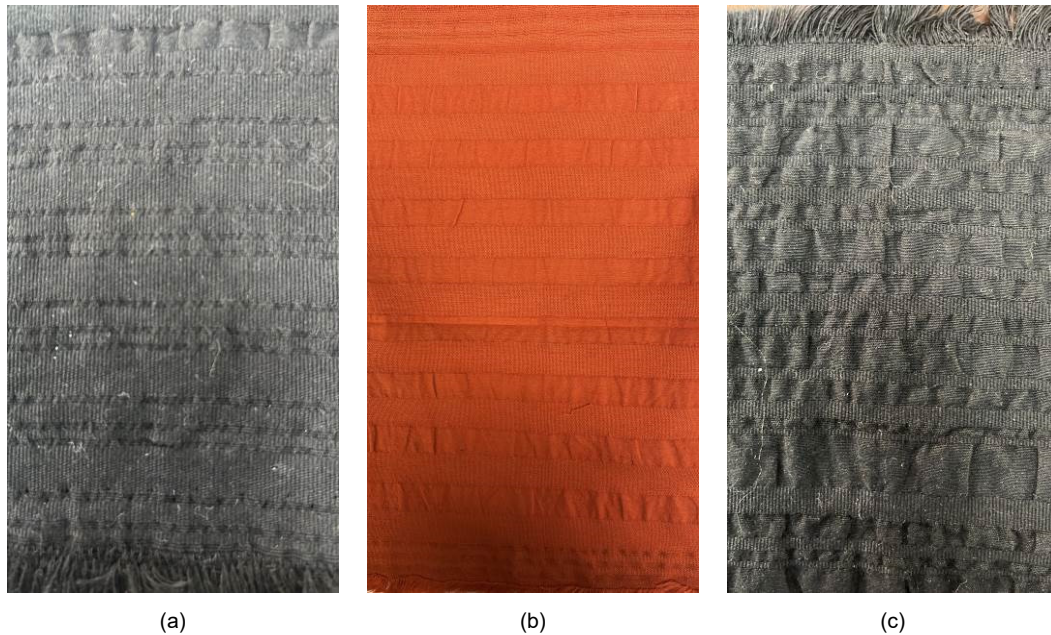
Figure 6. Different proto trials on hand loom: (a) P1, (b) P2, (c) P3. (Photograph: Ayçin Asma, 2022).

and 20x1 tex combed cotton yarns as indicated in Table 1, on a 2022 model Picanol OptiMax weaving machine equipped with a single beam. The machine operated at a speed of 440 rpm during production. The warp density was 68 threads per cm, and the weft density was 37 threads per cm. Figure 7 shows the image of the machine during production.

The information regarding the yarns used in fabric production is provided in the following table (Table 1).

The raw fabrics were processed through various stages including singeing, cold mercerization, causticizing, ram drying, dye padding, dye washing, super touch drying, intermediate inspection, super touch finishing, steaming, and final inspection to transform them into finished fabrics. Figure 8

presents visual representations of both the raw fabric samples (a) and the finished fabric samples (b).

Tests were applied to the fabrics in order to measure the suitability and mass production of these seersucker-like fabrics.

Post-washing dimensional change, washing fastness, dry and wet rubbing fastness, rupture and tear strength tests were performed on the produced fabrics. Dimensional change measurements of the samples were made by washing under "delicate" conditions and "line drying" application in accordance with AATCC 135 standard [20]. Tensile strength test was performed on James Heal Tinius Olsen apparatus in accordance with ASTM D5034 [21]

Figure 7. Seersucker fabric production on the machine. (Photograph: Ayçin Asma, 2023).

Table 1. Information on combed cotton yarns used in fabric production.

	Warp	Weft
Yarn Number [tex]	12x1	20x1
Yarn Twist [TPM]	1142	905
Yarn Twist Direction	Z	Z

Table 2. Declared values and test results.

Property	Direction	Declared Value	Test Results
Fabric Mass per Unit Area [g/m^2]		180 ± 5	185
Dimensional Stability (After Washing) [%]	Warp	-5.5	-4
	Weft	-3	-2.5
Washing Fastness Grade		4/5	5
Rubbing Fastness Dry Grade		5	4/5
Rubbing Fastness Wet Grade		5	4/5
Tensile Strength [N]	Warp	312.8	615.9
	Weft	560	603.1
Tear Strength [N]	Warp	19.43	16.43
	Weft	12.66	13.04
Extension [%]	Warp	4	4
	Weft	7.2	7
Growth [%]	Warp	0.4	0.8
	Weft	1.6	0.2
Air Permeability [mm/s]		73	30
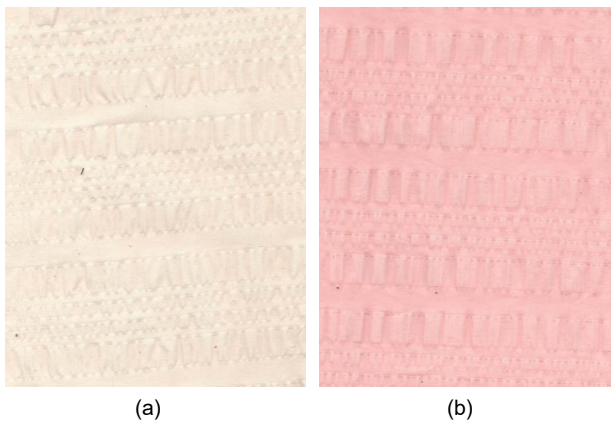
Figure 8. (a) Raw seersucker fabric swatch, (b) Finished seersucker fabric swatch. (Photograph: Ayçin Asma, 2022).

standard and tear strength test was performed on James Heal ElmaTear apparatus in accordance with ASTM D1424 [22] standard. The washing fastness was evaluated using the James Heal Gyrowash 1615 device following the AATCC 61 [23, 24] standard. The fabric stretch properties test was conducted according to the ASTM D3107 standard [25]. Additionally, the fabric air permeability test was performed on the SDL ATLAS air permeability tester device in accordance with the ISO 9237 standard [26].

RESULTS

In the study, three different fabric structure designs were made to obtain the seersucker surface appearance. Through the experiments conducted in line with the design studies, it was possible to achieve a wrinkled effect on the fabric surface by utilizing the tension differences created by the combination of various weaving structures in the fabrics. However, one of the fabric swatches (referred to as P3 in Figure 6) successfully exhibited the typical seersucker appearance. The focus of the study was specifically on this design, and the fabric was produced in its finished form. After dyeing and finishing processes, there were no alterations in the seersucker appearance of the fabric. The results of the washing, rubbing, and strength tests complied with the standards, and the fabric weight obtained fell within the desired values. The numerical values corresponding to the test results are provided in Table 2.

In a double warp beam loom, a traditionally woven 180±5 g/m^2, 100% cotton seersucker fabric exhibited dimensional change ratios (%) of -5.5 in the warp and -3 in the weft. Considering these values, it can be observed that the fabrics produced using the newly developed method within the scope of this study exhibit better dimensional stability.

In a commercially produced 180±5 g/m^2, 100% cotton seersucker fabric mentioned above, the washing fastness was rated 4/5, and the rubbing fastness averaged at 5. Upon examining the washing and rubbing fastness results of the fabrics produced using the new method, it is observed that they exhibit the same values as the fabrics produced using the traditional method.

When compared with fabrics produced using the traditional method, the tensile strength value of the fabric is significantly higher, while the tear strength result is slightly lower. However, the test results obtained for the fabric produced in this study are still within acceptable values.

When the results of fabric stretch properties are examined; in the warp direction, it is seen that the results are within the required value ranges as in the other tests. In the weft direction, it is seen that the growth value of the new fabric is better.

In addition to all this, when the air permeability properties are compared, it is observed that there is a difference between the traditional fabric and the new fabric. The reason for this is the difference between the production methods and fabric structures. However, this situation can be improved with further studies.

CONCLUSION

Seersucker fabrics have been in increasing demand in recent years due to their features such as being light, having good comfort properties, not requiring ironing thanks to their wrinkled surface appearance and thus being user-friendly. However, the increasing level of consciousness in the society about sustainability and the desire of consumers to return to natural lifestyles lead to the preference of products produced with natural raw materials in textile products. Seersucker fabric production is currently possible with different methods. However, in these methods, it is required either to use elastane yarns produced with synthetic raw materials or to have a special machine park that can work with double beam. In this study, it is aimed to produce seersucker fabrics without elastane and without the need for double beams. For this purpose, different fabric compositions were designed and sample productions of the designed fabrics were carried out. As a result of the experiments, it was seen that the seersucker effect was realized to the expected extent in the designed fabrics. The fabrics designed with the use of completely natural raw materials can be produced and commercialized. At the same time, seersucker production can be carried out on every machine when necessary with the method put forward in the study and the designed fabric weave compositions, and thus production efficiency can be increased. As such, the study offers an alternative method and design proposal to the methods currently used in seersucker fabric production. It is believed that the study will be a source for future academic and sectoral studies.

REFERENCES

1. Matusiak, M.: Manufacturing and Investigation of Seersucker Woven Fabrics, Buletinul AGIR nr. 1/2018
   https://www.agir.ro/buletine/2985.pdf
2. Basra, A.S., Azam, Z., Asfand, N., et al.: Development of interlock structural seersucker fabric for better comfort properties, Journal of Engineered Fibers and Fabrics, 15, 2020, pp.1-8.
   https://doi.org/10.1177/1558925020963009
3. Maqsood, M., Nawab, Y., Javaid, M.U., et al.: Development of seersucker fabrics using single warp beam and modelling of their stretch-recovery behaviour, The Journal of The Textile Institute, 106(11), 2015, pp. 1154-1160.
   https://doi.org/10.1080/00405000.2014.977542
4. Matusiak, M., & Frączczak, Ł: Influence of kind of weft yarn on properties of the seersucker woven fabrics, AUTEX Research Journal, 16(4), 2016, pp. 214-221.
   https://doi.org/10.1515/aut-2016-0021
5. Frączczak, Ł., Rafał, D., Piotr, Z., et al.: Parameterization of seersucker woven fabrics using laser techniques, Autex Research Journal, 19(3), 2019, pp. 243-249.
   https://doi.org/10.1515/aut-2018-0042
6. Kumaş Fırsatı Web Sitesi, Gofre Kumaş Örneği, (2022, December 28). Retrieved from:
   https://www.kumasfirsati.com/tr/gofre-kumas-bej/u/37194
7. Asma, A., Kanberoğlu, E., Kadınkız, N., et al.: A Study of different types of seersucker fabric design by industrial scale production line, Journal of Design Sciences and Applied Arts, 4(1), 2022, pp. 26-33.
   https://dx.doi.org/10.21608/jdsaa.2023.167494.1228
8. Kütükoğlu, M. S.: 1640 Tarihli Narh Defteri, 1983, Enderun Kitabevi, İstanbul.
9. Uğurlu, A., Uğurlu, S.S.: Yörenin Kültürel Kimliği Olarak Buldan Bezi, Buldan Sempozyumu, 23-24 Kasım, 2006.
   http://buldansempozyumu.pau.edu.tr/kitap/7.oturum/2.pdf
10. Türkiye Dokuma Atlası, Anadolu'nun Miras Kumaşları Kataloğu, Haziran 2021.
11. Kanberoğlu, E., Asma, A., Kadınkız, N., et al: Design and characterization of tencel-based seerscuker fabrics, Tekstilna Industrija, 70(4), 2022, pp. 14-21.
    https://doi.org/10.5937/tekstind2204014K
12. Matusiak, M.: Comfort-related properties of cotton seersucker fabrics, AUTEX Research Journal, 23(1), 2021.
    https://doi.org/10.2478/aut-2021-0049
13. Özgen Keleş, B., Yılmaz, E.: Dokuma Teknolojileri ve Uygulamaları, 2022, İksad Publications, Ankara.
14. Matusiak, M., Bajzik, V.: Surface characteristics of seersucker woven fabrics, 2021, Autex Research Journal, 21(3), pp. 284-292.
    https://doi.org/10.2478/aut-2019-0079
15. Matusiak, M.: Investigation of surface geometry of seersucker woven fabrics, AUTEX Research Journal, 2022.
    https://doi.org/10.2478/aut-2022-0023
16. Frączczak, Ł., & Matusiak, M.: Influence of the structure of seersucker woven fabrics on their friction properties, Autex Research Journal, 21(1), 2021, pp. 85-91.
    https://doi.org/10.2478/aut-2019-0063
17. Matusiak, M.: Moisture management properties of seersucker woven fabrics of different structure, FIBRES & TEXTILES in Eastern Europe, 27, 3(135), 2019.
    https://doi.org/10.5604/01.3001.0013.0741
18. Matusiak, M., Zielinski, J., Kwiatkowska, M.: Measurement of tensile properties of seersucker woven fabrics of different structure, FIBRES & TEXTILES in Eastern Europe, 27, 2(134) 2019.
    https://doi.org/10.5604/01.3001.0012.9988
19. Ghahraman, F. G., Tavanai, H., Hosseini, S. A.: A qualitative assessment of seersucker effect through spectral density and angular power spectrum function algorithms, The Journal of The Textile Institute, 101(3), 2010, pp. 276-281.
    https://doi.org/10.1080/00405000802399536
20. AATCC 135. Test Method for Dimensional Changes of Fabrics after Home Laundering, 2018t.
21. ASTM D5034. Standard Test Method for Breaking Strength and Elongation of Textile Fabrics, 2021.
22. ASTM D1424-21. Standard Test Method for Tearing Strength of Fabrics by Falling Pendulum (Elmendorf Type) Apparatus, 2021.
23. AATCC 8. Test Method for Colorfastness to Crocking: Crockmeter, 2016e.
24. AATCC 61. Test Method for Colorfastness to Laundering: Accelerated, 2020.
25. ASTM D3107-07. Standard Test Methods for Stretch Properties of Fabrics Woven from Stretch Yarns, 2019.
26. TS 391 EN ISO 9237. Textiles-Determination of Permeability of Fabrics to Air, 1999.

THE INFLUENCE OF LOW-TEMPERATURE PLASMA ON PERMANENCE OF ANTIMICROBIAL NANO-FINISH

ŠČASNÍKOVÁ, KATARÍNA[1]*AND DUBEC, ANDREJ[2]

1   VÚTCH - CHEMITEX, spol. s r.o., Rybníky 954, 011 68 Žilina, Slovak Republic
2   FPT - Púchov, Ivana Krasku 491/30, 020 01 Púchov, Slovak Republic

ABSTRACT

This paper describes the effect of low-temperature plasma on increasing permanence of surface finish of textile materials using an antimicrobial nanosol. Selected textile materials (polyester and polyamide woven fabrics, polypropylene non-woven fabric) were pre-treated by surface activation with low-temperature plasma at atmospheric pressure and subsequently finished using an antimicrobial (AMB) nanosol with a concentration of 60 ppm Ag^+, 120 ppm Ag^+ in the application solution. The goal was to increase the permanence of AMB nano-coating of textiles after washing and drying. To verify the effect of low-temperature plasma on increasing the permanence of the nanolayer, washing and drying was performed in accordance with the STN EN ISO 6330 standard. To determine antibacterial activity and effectiveness of the nano-coated textile materials, a quantitative test method was used in accordance with the technical standard AATCC TM 100. Evaluation of the antibacterial activity of the textile materials was performed before washing and after 20 washing cycles.

KEYWORDS

Antibacterial effectiveness; Antimicrobial nanosol; Antibacterial textiles; Low-temperature plasma.

INTRODUCTION

Plasma treatments are gaining popularity in the textile industry due to many advantages over traditional wet finishing technologies. However, plasma can be used also in combination with wet finishing technologies, enabling to achieve new or modified properties, or to increase or extend desired properties of the application [1].

Low-temperature plasma treatment belongs to the environmentally friendly technologies used to modify the surface properties of polymer materials. Interactions between the plasma and the polymer surface lead to surface phenomena such as etching, cross-linking and activation [2]. Atmospheric plasma pre-treatment can add a large number of functional groups to the polymer surface depending on the processing gas in the plasma reactor. Plasma techniques offer far-reaching possibilities, but the technical effort is relatively high, as the processes often have to be carried out at reduced pressure [3]. Diffuse coplanar surface barrier discharge (DCSBD) plasma-based processes in atmospheric air provide sufficient modification of textiles. After plasma treatment, free radicals which settled on the surface of the material, immediately react with atmospheric oxygen to form hydroperoxides [4]. Plasma treatment causes not only chemical but also physical changes. The physical effect of plasma treatment is disruption of the fiber surface, which becomes larger and contains more places for physical connection. Plasma treatment is reported to be an effective technique for surface treatment of textiles to improve their wettability and adhesion [5]. Plasma technology changes the cost structure of textile processing by reducing energy consumption, environmental waste and the amount of chemicals used. The application of atmospheric discharge plasma offers higher production speed, better products as well as better surface finishes on the textiles [6].

Polyester fabrics belong to the most commonly produced fabrics in the textile industry. Polyester polymers have few polar oxygen groups. Low-pressure plasma treatments were designed to modify their surface properties (hydrophobicity and wettability) by introducing polar groups or by increasing surface roughness [7, 8].

Polypropylene textile materials are an interesting field of research as well. Surfaces of these materials are practically free of polar groups and therefore hydrophobic ones. There are many methods for surface treatment of polypropylene textiles, including the low-temperature plasma processing. This

Table 1. Basic structural parameters of the input textile materials.

Designation of the textile materials	Woven fabrics		Non-woven fabric
	PES	**PA**	**PP**
Material composition	100% polyester	100% polyamide	100% polypropylene
Colour	white	white	white
Weave	canvas	twill 2/2	-
Mass per unit area [g/m²]	106	99.7	40
Thickness [mm]	0.95	0.89	0.38

modification method is becoming more and more popular because it does not require a large amount of conventional chemicals, what is beneficial not only for the economy but also for the environment [9]. Currently, the results of finishing polypropylene non-woven fabric produced by spunbond technology with hydrogen fluoride using plasma are known as well. It was found that a fabric modified this way shows 99,04 % bacterial reduction, representing an effective barrier against penetration of the micro-organisms [10].

In recent years, an increased interest in antibacterial finish of fibers and textiles for practical application has been observed. Most textile materials used, e.g. in hospitals, can cause transmission of diseases caused by bacteria. Textile materials made from natural fibers provide an excellent environment for the growth of micro-organisms due to their large surface area and ability to retain moisture [11]. Today, the textile users demand textiles showing a number of performance characteristics, regardless of whether they are intended for the production of clothing, home textiles or materials for outdoor use. The decision to use them is often based on functional aspects of the fabric. Antimicrobial finish can offer added value to many different types of textiles [12]. Bacteria and fungi can degrade textiles in several ways, their decomposition causes odors especially in underwear and sportswear, they multiply especially in medical environment and are responsible for deterioration of a product due to its decomposition. The growth of microbes affects negatively also some other properties of textiles, such as change in color and/or permanent degradation of, for example, awnings, tents, etc. [13].

The aim of the paper is to verify the effect of low-temperature plasma on the permanence of antimicrobial nano-finish applied to the surface of selected textiles, pre-treated with low-temperature plasma under atmospheric pressure and subsequently finished with antimicrobial nanosol AMB-9. Antibacterial activity of these textiles was evaluated against selected strains of bacteria before and after washing [14].

EXPERIMENTAL PART

The experimental part describes pre-treatment of selected textile materials - polyester woven fabric

(PES), woven fabric made from polyamide 6 (PA) and polypropylene non-woven fabric (PP) using the progressive technology of applying low-temperature plasma under atmospheric pressure and subsequent application of AMB nanosol. Consequently, their antibacterial activity and permanence of the AMB finish after washing were evaluated.

Specification of the input textile materials

Basic structural parameters of the input textile materials used in the experimental part are listed in the Table 1.

Activation of the textile material surface with low-temperature plasma

As part of the research, conditions for activating the surface of textiles with low-temperature plasma under atmospheric pressure were verified. Surface of the textile material was activated by low-temperature plasma with DCSBD (Diffuse Coplanar Barrier Discharge) on a quarter-operation finishing line ZUP 400 (Figure 1) under specific conditions as follows:

- power of plasma electrodes: 350 W,
- time of plasma surface activation: 150 s,
- line shift speed: 0,98 m.min⁻¹.

ZUP 400 device is designed for double-sided continuous treatment of textile materials; it enables the interconnection of activation of textile surfaces with low-temperature plasma under atmospheric pressure and subsequent chemical finishing of the textile materials. The device has 4 electron systems located on both sides in a working width of 400 mm with the possibility of setting the working speed from 0.67 m/min to 14.7 m/min and the power of the electrode systems 4x 400 W.

Pre-treatment of the textiles with low-temperature plasma under the specified conditions was problem free, passage of the textile materials through the plasma electrodes was smooth, no phenomena appeared during plasma treatment that would negatively affect the technological process of pre-treatment of the textiles.

Application of AMB nanosol to the textiles

The AMB nanosol was applied to textile materials pre-treated with low-temperature plasma, as well as to textile materials without pre-treatment with low-temperature plasma, in order to create an antimicrobial coating (Table 2).

Application solutions of AMB nanosol with a concentration of 60 ppm Ag⁺, 120 ppm Ag⁺ in the solution were used for treatment. The excess solution was removed from the finished fabrics by wringing on Fulard VFM Werner - Mathis AG device. The nanocoated textiles were dried and heat-set under the same conditions in Werner-Mathis AG dryer at a temperature of 100 °C for 2 min.
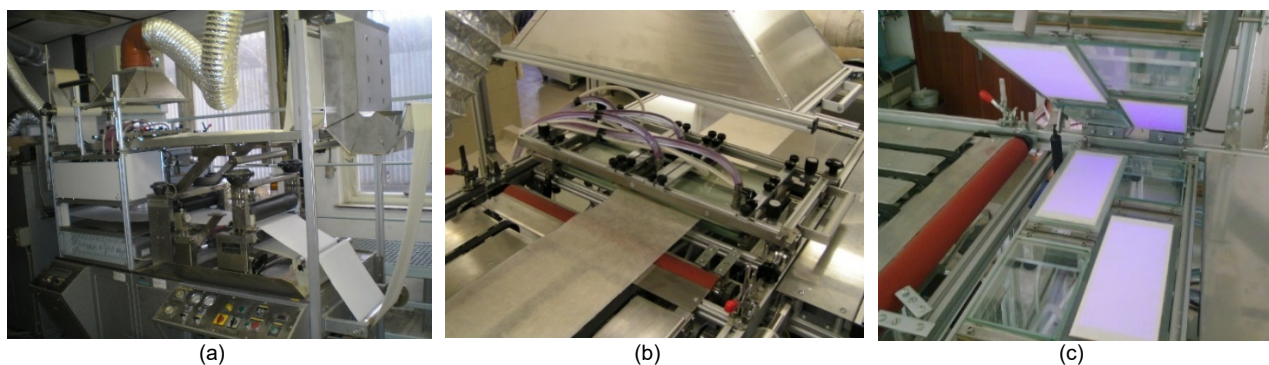
(a)   (b)   (c)

Figure 1. ZUP 400 quarter-operation processing equipment (a), surface activation of a fabric (b), plasma sources in working mode (c).

Table 2. Identification of textiles from PES, PA and PP to verify antibacterial effectiveness, permanence of the nano-coating.

Description of textile samples	woven fabric		non-woven fabric
fabric finished with an **AMB** nanosol application solution with a concentration of **60 ppm Ag⁺**	PES/AMB$_{60}$	PA/AMB$_{60}$	PP/AMB$_{60}$
fabric finished with an **AMB** nanosol application solution with a concentration of **120 ppm Ag⁺**	PES/AMB$_{120}$	PA/AMB$_{120}$	PP/AMB$_{120}$
fabric finished with plasma, application solution of **AMB** nanosol with a concentration of **60 ppm Ag⁺**	PES/150s/AMB$_{60}$	PA/150s/AMB$_{60}$	PP/150s/AMB$_{60}$
fabric finished with plasma, application solution of **AMB** nanosol with a concentration of **120 ppm Ag⁺**	PES/150s/AMB$_{120}$	PA/150s/AMB$_{120}$	PP/150s/AMB$_{120}$

In order to verify changes in surface macrostructure of the AMB finished textile material and prove the presence of the AMB nano-finish, SEM (Scanning Electron Microscopy) analysis of the surface of the PP non-woven fabric was performed with a magnification of 1000 times and 15 000 times respectively (Figure 2, 3). A compact layer of the AMB nano-coating is visible on the surface of PP fibers in the Figure 3.

The modified textile samples (Table 2) were subjected to washing and drying according to the STN EN ISO 6330: 2022 standard by the 4N washing procedure with water temperature of (40±3) °C using a commercial detergent, drying was carried out by the C procedure, i.e. drying in a horizontal position on a flat surface (laid out flat).

Evaluation of antibacterial activity of the AMB nano-coated textiles

Evaluation of antibacterial finishes applied to the textile materials is determined by degree of antibacterial activity required when using such materials. If bactericidal activity is required or assumed, quantitative assesment is necessary. Quantitative assesment will also create a clearer picture of possible applications of the modified textile materials. To determine the requirements for antimicrobial nano-coated textile materials, test method was used in accordance with the technical standard AATCC 100-2019 "Assessment of antibacterial finishes on textile materials" [14].

AATCC TM 100 – 2019 test method evaluation conditions:

- test micro-organism:

  a) gram positive bacterium Staphylococcus aureus CCM 4516,

  b) gram negative bacterium Klebsiella pneumoniae CCM 8853,

- bacterial concentration achieved: $1.0 \times 10^5 – 3.0 \times 10^5$ CFU/ml;

- size and quantity of samples used: circle – shaped samples with a diameter of (4.8 ± 0.1) cm and with a weight of (1.0 ± 0,1) g are cut out of a test fabric;

- amount of inoculum per sample: (1.0 ± 0.1) ml;

- test conditions: 24 h, (37 ± 2) °C, nutrient used: Nutrient Agar pH 6.8.

This test method is a quantitative procedure for comparison and evaluation of the degree of antibacterial effectiveness after 24-hour exposure to the test bacteria on a textile sample. After incubation, the bacteria are eluted from the textile samples and total bacterial number is determined. The method involves actual bacterial counts, with results reported as a percentage or logarithmic reduction in contamination levels. Bacterial reduction of the test sample is calculated in percentages according to the following equation:

$$100 (C – A) / C = R, \qquad (1)$$

where: R is the bacterial reduction in percentages; C is the number of bacteria recovered from the inoculated finished test samples in the vessel, immediately after vaccination (in "0" contact time); A is the number of bacteria recovered from the inoculated finished test samples in the vessel, incubated for 24 h contact time.
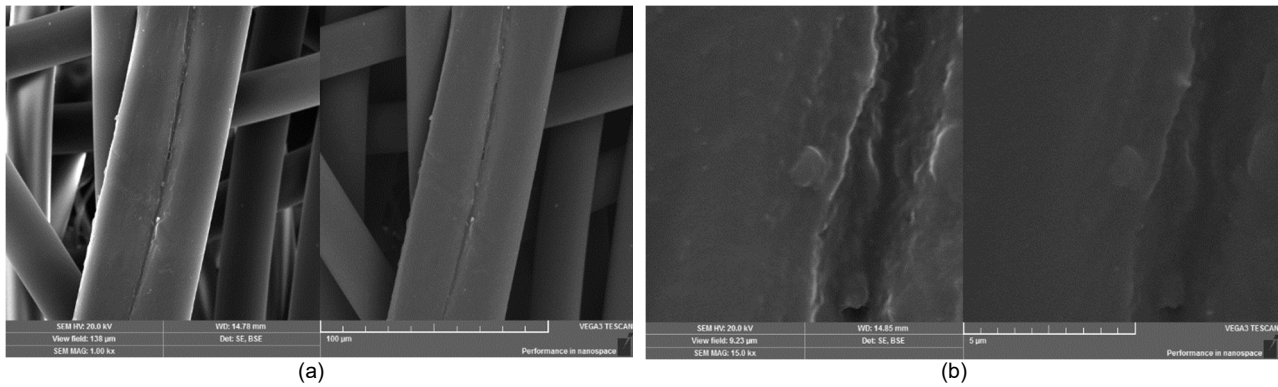
Figure 2. SEM images of the PP non-woven fabric without application of AMB nanosol, maginication: (a) 1000 x, (b) magnification 15 000 x.

Figure 3. SEM images of PP non-woven fabric with AMB nanosol application, magnification: (a) 1000 x, (b) magnification 15 000 x.

Table 3. Results of the antibacterial effectiveness of PES fabrics before and after washing against the bacterium *Staphylococcus aureus* CCM 4516.

	Bacterial reduction R [%]				
Number of washing cycles	0	5	10	15	20
PES/AMB$_{60}$	98.84	24.90	9.09	0.00	0.00
PES/150s/AMB$_{60}$	99.67	99.45	93.17	89.52	83.33
PES/AMB$_{120}$	99.73	54.74	25.00	10.35	0.00
PES/150s/AMB$_{120}$	99.95	99.71	98.27	97.82	91.80

Table 4. Results of the antibacterial effectiveness of PA fabrics before and after washing against the bacterium *Staphylococcus aureus* CCM 4516.

	Bacterial reduction R [%]				
Number of washing cycles	0	5	10	15	20
PA/AMB$_{60}$	99.64	98.69	98.37	98.27	98.09
PA/150s/AMB$_{60}$	99.83	99.65	99.31	98.64	98.89
PA/AMB$_{120}$	99.80	99.73	99.74	98.49	98.40
PA/150s/AMB$_{120}$	99.90	99.69	99.43	99.30	99.17

RESULTS AND DISCUSSION

Antibacterial effectiveness of the finished textiles was evaluated before and after washing and drying (in Tables 3-8).

Antibacterial effectiveness of the nano-coated textiles

On samples of textile materials made of 100% PES, 100% PA and 100% PP with AMB nano-coating (with/without plasma pre-treatment), the antibacterial effectiveness was evaluated before and after washing in accordance with the AATCC Test Method 100-2019 using the test micro-organisms *Staphylococcus aureus* CCM 4516 (Tables 3-5, Figures 4-6) and *Klebsiella pneumoniae* CCM 8853 (Tables 6-8, Figures 7-9), under the above-mentioned test conditions.

From the results presented in the Tables 3-4, it can be concluded that by application of AMB nanosol in a concentration of 60 ppm Ag$^+$ as well as in a concentration of 120 ppm Ag$^+$, a high antibacterial effectiveness ($R > 99$%) was achieved on the

Table 5. Results of the antibacterial effectiveness of PP fabrics before and after washing against the bacterium Staphylococcus aureus CCM 451.

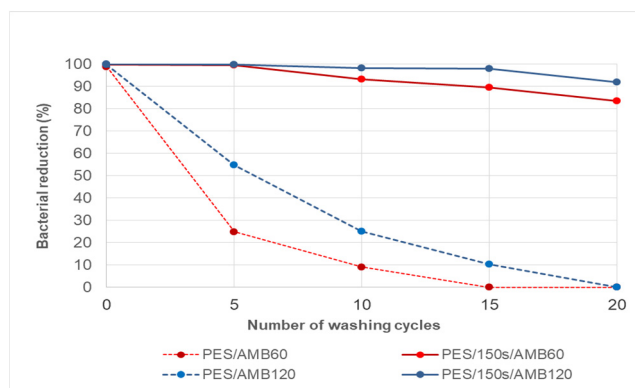|	Bacterial reduction R [%]				
Number of washing cycles	**0**	**5**	**10**	**15**	**20**
PP/AMB$_{60}$	57,52	41.84	3.54	not evaluated	not evaluated
PP/150s/AMB$_{60}$	99.92	98.83	57.97	not evaluated	not evaluated
PP/AMB$_{120}$	70.59	60.00	16.67	not evaluated	not evaluated
PP/150s/AMB$_{120}$	99.92	99.78	58.46	not evaluated	not evaluated

Figure 4. Influence of washing and drying on bacterial reduction of Staphyloccocus aureus CCM 4516 on the AMB finished PES woven fabric.
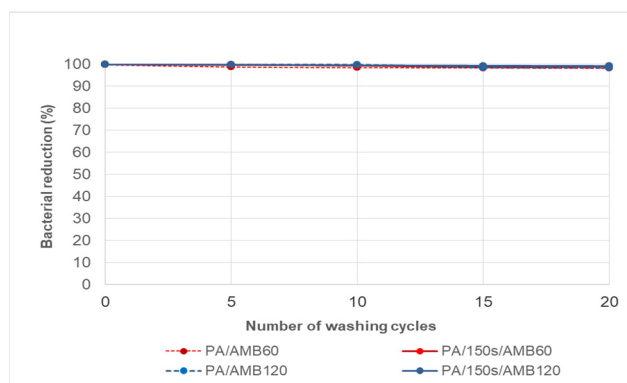

Figure 5. Influence of washing and drying on bacterial reduction of Staphyloccocus aureus CCM 4516 on the AMB finished PA woven fabric.
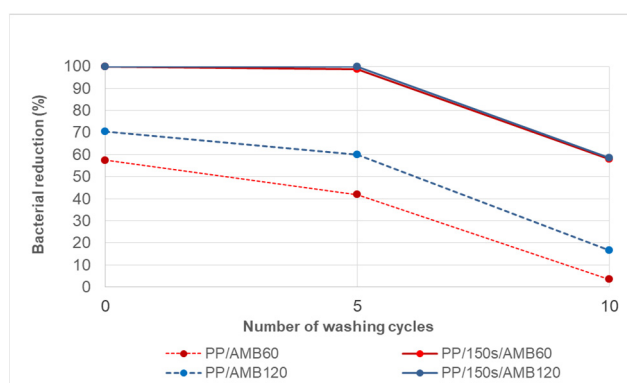

Figure 6. Influence of washing abd drying on bacterial reduction of Staphyloccocus aureus CCM 4516 on the AMB finished PP non-woven fabric.

samples of woven fabrics made from PES and PA before washing at the "bactericidal" level against the test micro-organism Staphylococcus aureus CCM 4516.

The same antibacterial effectiveness was achieved on the samples of woven fabrics with AMB nanosol application without plasma pre-treatment (PES/AMB$_{60}$, PES/AMB$_{120}$, PA/AMB$_{60}$, PA/AMB$_{120}$) as on the samples with AMB nanosol application with plasma pre-treatment and surface activation time of 150s (PES/150s/AMB$_{60}$, PES/150s/AMB$_{120}$, PA/150s/AMB$_{60}$, PA/150s/AMB$_{120}$). It can be seen from the results that time of surface activation with low-temperature plasma has no effect on final antibacterial effectiveness of these materials before washing (Tables 3, 4).

The same high bactericidal effect was achieved on the PP non-woven fabrics with applied solution of AMB nanosol and with surface activation by low-temperature plasma (PP/150s/AMB$_{60}$, PP/150s/AMB$_{120}$), before washing, at the level of bacterial reduction of Staphylococccus aureus CCM 4516 $R > 99$ % (Table 5). Antibacterial finish of the test samples without plasma activation PP/AMB$_{60}$ and PP/AMB$_{120}$ for the micro-organism Staphylococccus aureus CCM 4516, showed bacterial reduction at the level of approximately 60-70%.

In order to verify the effect of plasma on increasing the affinity of the nano-layer to the surface of the textile material, and/or permanence of the antibacterial finish, samples of nano-coated textile materials were subjected to 5-20 washing and drying cycles in accordance with STN EN ISO 6330: 2022 by the 4N washing procedure with water temperature of (40±3) °C using a commercial detergent. Drying was carried out by C procedure, i.e. drying in a horizontal position in a spread state on a flat surface (laid out flat) and then the antibacterial effectiveness was evaluated on them. From a practical point of view, it is important to what extent the applied surface finish of the textiles is stable (permanent), and therefore tests of the finished fabrics by washing and drying were carried out in the frame of the experiments as well. Samples of the material were subjected to 5-20 washing and drying cycles and subsequently their antibacterial effectiveness was re-evaluated to verify the effect of plasma on increasing the affinity of the nano-layer to the surface of the textile material, and/or permanence of the nano-coating on the textile materials. Results of the tests

are shown in the Tables 3-5. The non-woven fabric made of 100 % PP was losing its shape after the 10th washing cycle, therefore washing of the PP fabric was not continued.

From the results shown in the Table 4 it can be concluded that the application of AMB nanosol on PA fabric without/with surface activation by low-temperature showed a high antibacterial effect (approx. 99%) even after 20 washing cycles. Neither effect of low-temperature plasma, nor concentration of AMB nanosol on the antibacterial effectiveness was observed on the PA woven fabric, as bacterial reduction on the PA woven fabric with/without pre-treatment with low-temperature plasma was the same.

A positive effect of low-temperature plasma on the permanence of AMB nano-coating was found both on PES woven fabric and PP non-woven fabric already after the 5th washing and drying cycle. The bacterial reduction of these fabrics, regardless of the concentration of AMB nanosol, was at the level of 99% on the low-temperature plasma pretreated materials (PES/150s/AMB$_{60}$, PES/150s/AMB$_{120}$, PP/150s/AMB$_{60}$, PP/150s/AMB$_{120}$). Bacterial reduction on samples of the fabrics without low-temperature plasma pre-treatment (PES/AMB$_{120}$, PP/AMB$_{120}$), finished using AMB nanosol with a concentration of 120 ppm Ag$^+$ in the application solution, compared to textiles pre-treated with low-temperature plasma (PES/150s/AMB$_{120}$, PP/150s/AMB$_{120}$) decreased by approx. 40 - 45 %. A more pronounced decrease was recorded for textiles without low-temperature plasma pre-treatment (PES/AMB$_{60}$, PP/AMB$_{60}$) finished using AMB nanosol with a concentration of 60 ppm Ag$^+$ in the application solution, which was at the level of approximately cca 60–75 %.

After the 10th washing and drying cycle, the sample of PES woven fabric PES/AMB$_{60}$, compared to the PES/AMB$_{60}$ sample before washing, showed a significant decrease in bacterial reduction to the level of about 90%. A somewhat lower decrease was recorded with the sample PES/AMB$_{120}$, where bacterial reduction after washing decreased by 75% (Table 3). The same course of decrease in antibacterial effectiveness after washing was also recorded for samples of PP fabrics, where bacterial reduction after washing decreased by approx. 95% (PP/AMB$_{60}$) and approx. 75% (PP/AMB$_{120}$). From the results regarding the mentioned PES and PP samples finished with AMB nanosol after plasma pre-treatment of the surface (PES/150s/AMB$_{60}$, PES/150s/AMB$_{120}$, PP/150s/AMB$_{60}$, PP/150s/AMB$_{120}$), it can be seen that in this case time of surface activation of the material by plasma has a positive effect on the resulting antibacterial effectiveness.

A positive effect of low-temperature plasma was demonstrated on PES textile samples even after 15-

20 washing and drying cycles. While the bacterial reduction in the PES fabric PES/AMB$_{60}$ and/or PES/AMB$_{120}$ without plasma treatment already after the 15th washing and drying cycle dropped to 0% and/or approx. 10%, bacterial reduction on the PES fabric PES/150s/AMB$_{60}$ and/or PES/150s/AMB$_{120}$ pre-treated with low-temperature plasma was at the level of approx. 90-98%. While after the 20th washing cycle the PES textile samples at both concentrations of AMB nanosol without plasma pre-treatment (PES/AMB$_{60}$, PES/AMB$_{120}$) lost their antibacterial effectiveness (bacterial reduction of these textiles dropped to the level of 0%), bacterial reduction of the PES textile samples with both concentrations of AMB nanosol, with plasma pre-treatment (PES/150s/AMB$_{60}$, PES/150s/AMB$_{120}$) decreased by only about 10 - 20%.

In general, it can be concluded that the highest antibacterial effectiveness after 20 washing cycles was achieved on the sample of PA woven fabric (PA/150s/AMB$_{120}$) finished with an application solution of the antimicrobial nanosol containing 120 ppm Ag$^+$, whose bacterial reduction for the test micro-organism Staphylococccus aureus CCM 4516 was approx. 99,17% (Table 4).

The performance characteristic - antibacterial effectiveness - was evaluated on the prepared nano-coated samples of PP and/or PA woven fabric and PP non-woven fabric using the test micro-organism Klebsiella pneumoniae CCM 8853. Results of the evaluation are shown in Tables 6-8, Figures 7-9.

The antibacterial effectiveness of PP, PES and PA fabrics against the bacterium Klebsiella pneumoniae was comparable to that of the bacterium Staphylococcus aureus.

PA fabrics pre-treated with low-temperature plasma (PA/150s/AMB$_{60}$, PA/150s/AMB$_{120}$) showed the highest resistance against the bacterium Klebsiella pneumoniae. Their bacterial reduction, regardless of the concentration of AMB nanosol, was even after 20 washing cycles at the level of R > 95 % (Table 7). Despite a small decrease in the reduction of PA fabrics without low-temperature plasma pre-treatment (PP/AMB$_{60}$, PP/AMB$_{120}$) to the level of approx. 80-90%, we do not consider this decrease to be significant. Even with the bacterium Klebsiella pneumoniae, it was confirmed that plasma pre-treatment is not unavoidable for PA fabrics to ensure permanence of the surface AMB finish. By evaluating the antibacterial effectiveness the effectiveness of the nano-coating was again demonstrated, without demonstrating the effect of plasma on the affinity of the nano-coating.

The antibacterial effect of both application solutions of the prepared AMB nanosol without low-temperature plasma pre-treatment as well as with low-temperature plasma pre-treatment was equally high on the PES woven fabric.

Table 6. Results of the antibacterial effectiveness of PES textiles before and after washing against the bacterium Klebsiella pneumoniae CCM 8853.

Bacterial reduction R [%]					
Number of washing cycles	0	5	10	15	20
PES/AMB60	99.74	22.90	8.85	0.00	0.00
PES/150s/AMB60	99.89	88.33	42.92	18.02	0.00
PES/AMB120	99.96	56.93	16.53	0.00	0.00
PES/150s/AMB120	99.96	92.86	61.88	39.02	7.86

Table 7. Results of the antibacterial effectiveness of PA textiles before and after washing against the bacterium Klebsiella pneumoniae CCM 8853.

Bacterial reduction R [%]					
Number of washing cycles	0	5	10	15	20
PA/AMB60	99.31	96.68	90.13	88.39	83.95
PA/150s/AMB60	99.88	99.35	98.27	97.84	95.38
PA/AMB120	99.70	99.26	97.84	96.12	93.03
PA/150s/AMB120	99.93	99.81	99.30	98.71	97.96

Table 8. Results of the antibacterial effectiveness of PP textiles before and after washing against the bacterium Klebsiella pneumoniae CCM 8853.

Bacterial reduction R [%]					
Number of washing cycles	0	5	10	15	20
PP/AMB60	45.31	26.32	0.00	not evaluated	not evaluated
PP/150s/AMB60	99.96	96.31	20.00	not evaluated	not evaluated
PP/AMB120	63.82	34.97	6.19	not evaluated	not evaluated
PP/150s/AMB120	99.95	99.61	37.00	not evaluated	not evaluated

Bacterial reduction on the PES woven fabric before washing was >99% (Table 6). The effect of low-temperature plasma was demonstrated on the PES woven fabric (PES/150s/AMB120) after 5 washing cycles, when the antibacterial effectiveness was at the level of bacterial reduction of approx. 93% and after 10 washing cycles with the bacterial reduction at the level of 62%. AMB nano-coated PES fabric with plasma pre-treatment (PES/150s/AMB120) after 20 washing cycles shows very low antibacterial effectiveness against the test micro-organism Klebsiella pneumoniae CCM 8853, namely at the level of bacterial reduction <8%. Antibacterial activity of the nano-coated textile materials after 20 washing and drying cycles was not demonstrated on the sample pre-treated with plasma (PES/150s/AMB60), on two samples without plasma pre-treatment (PES/AMB60, PES/AMB120).

Results of antibacterial effectiveness of the non-woven fabric from PP with surface activation by low-temperature plasma before washing are comparable to the results measured on the samples of woven fabrics from PES and PA for the two above mentioned test micro-organisms (> 99%, Tables 3-8).

By applying AMB nanosol to PP non-woven fabric activated by low-temperature plasma (PP/150s/AMB60), (PP/150s/AMB120), AMB effectiveness compared to the non-woven fabric without low-temperature plasma activation (PP/AMB60, PP/AMB120) achieved bacterial reduction of Klebsiella pneumoniae CCM 8853 more than 99,9 % (Table 8). The positive effect of low-temperature plasma was demonstrated on PP non-woven fabric

(PP/150s/AMB120) after 5 washing cycles, when the antibacterial effectiveness was at the level of bacterial reduction more than 99% and after 10 washing cycles the bacterial reduction was at the level of 37%. The AMB effectiveness of PP textiles for the Klebsiella pneumoniae strain is nevertheless lower than it was for the Staphylococcus aureus strain. In the PP/AMB60 sample, after the 10th washing cycle, the antibacterial effectiveness of the nano-coated non-woven fabric without surface activation by low-temperature plasma was lost. The sample PP/AMB120 achieved bacterial reduction of 6.19%, which was compared to the sample PP/AMB120 before washing a decrease of about 90%.
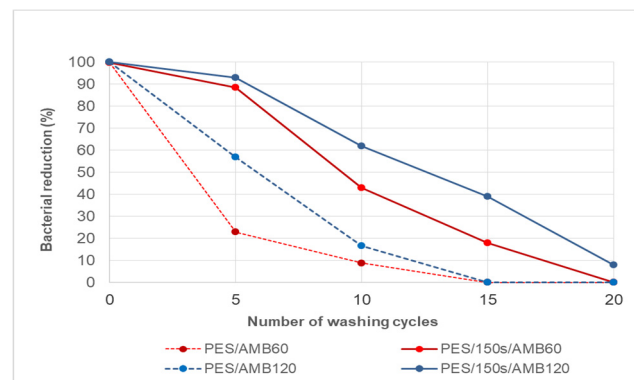

Figure 7. Effect of washing and drying on the reduction of bacteria Klebsiella pneumoniae CCM 8853 of AMB modified PES fabric.
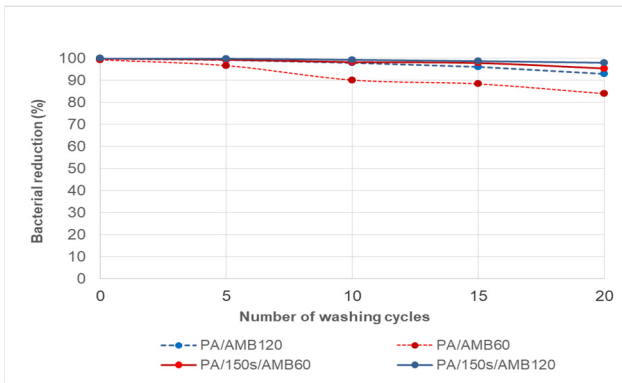
Figure 8. Effect of washing and drying on the reduction of bacteria Klebsiella pneumoniae CCM 8853 of AMB modified PA fabric.
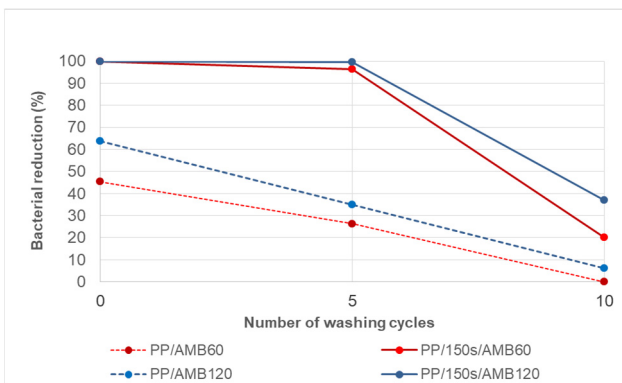

Figure 9. Effect of washing and drying on the reduction of bacteria Klebsiella pneumoniae CCM 8853 of AMB modified PP fabric.

CONCLUSION

Subject of the research was study and investigation of the relationships between the effects induced by low-temperature plasma on the initiated surface of textile materials made of synthetic fibers and the applied type of surface finish of the fabric using AMB nanosol, in order to create the prerequisites for increasing the permanence of the nano-coating of textiles using the antimicrobial nanosol after washing. In the frame of the research aimed at development of antimicrobial nano-coated textiles, the permanence of the AMB nano-coating on PES, PA fabric after 20 washing cycles and on PP non-woven fabric after a maximum of 10 washing cycles has been verified. Conclusions from the achieved results are as follows:

-   the highest bactericidal effectiveness with a high degree of reduction according to the AATCC TM 100 – 2019 method after 20 washing cycles was achieved with the textile sample from 100% PA woven fabric for both test micro-organisms Staphylococcus aureus and Klebsiella pneumoniae,

-   the highest antibacterial effectiveness of the antimicrobial nano-coating was achieved on the sample of PA fabric finished with the application solution containing 120 ppm Ag$^+$, where bacterial reduction of the test micro-organism Staphylococcus aureus as well as Klebsiella

pneumoniae was even after 20 washing and drying cycles at the level of approx. 99%,

-   results of the antibacterial effectiveness of the PA woven fabric do not confirm positive effect of low-temperature plasma on increasing affinity of the AMB nano-coating to the surface of the fabric from 100% PA. Bacterial reduction (Staphylococcus aureus, Klebsiella pneumoniae) of both pre-treated samples without/with plasma surface activation and with subsequent application of AMB nanosol (60 ppm Ag$^+$ and 120 ppm Ag$^+$) is also at the level of bactericidal effectiveness even after 20 washing cycles.

-   with an increasing number of washing cycles, there is a decrease in the antibacterial effectiveness of the PES woven fabric finished with AMB nanosol without plasma surface activation. A higher antibacterial effectiveness after washing and drying was achieved on the sample of PES fabric with plasma surface activation finished with an application solution of AMB nanosol containing 120 ppm Ag$^+$, whose bacterial reduction of the test micro-organism Staphylococcus aureus was even after 20 washing and drying cycles at the level of approx. 92%. A positive effect of surface activation of the PES fabric with low-temperature plasma was demonstrated by increasing the affinity of the AMB nanocoating to the surface of the fabric compared to the fabric finished with AMB nanosol under the same conditions without surface activation with low-temperature plasma.

-   AMB nano-coated PES fabrics with plasma surface activation achieve antibacterial properties with bacterial reduction of 83-92% for the test micro-organism Staphylococcus aureus, compared to the antimicrobially finished PES woven fabric without plasma surface activation, where bacterial reduction is at the level of 0%. A positive influence of the low-temperature plasma on the increased affinity of the AMB nano-layer to the surface of the textile material made from 100% PES can be noted from the above results,

-   for the test micro-organism Klebsiella pneumoniae, a bacterial reduction of only about 8% was demonstrated on the antimicrobially nano-coated PES woven fabric with nanosol concentration of 120 ppm Ag$^+$. No antibacterial properties were detected on PES woven fabric with AMB nanosol application without plasma surface activation. Bacterial reduction was not demonstrated even in the case of the sample with surface activation by low-temperature plasma with a concentration of AMB nanosol of 60 ppm Ag$^+$, no positive effect of plasma was demonstrated in this case.

-   Based on the above results, it is possible to state a positive effect of low-temperature plasma on

increasing the affinity of AMB nano-coating to the surface of textile material made from 100% PES compared to a fabric without surface activation by low-temperature plasma,

- nano-coated PP non-woven fabric with surface activation by low-temperature plasma shows antibacterial effectiveness at the bactericidal level against the test micro-organism Staphylococcus aureus and antibacterial effectiveness at the bacteriostatic level against the test micro-organism Klebsiella pneumoniae compared to the PP non-woven fabric without surface activation by low-temperature plasma. The PES and PA woven fabrics clearly retain higher antibacterial efficiency even after the 10th washing and drying cycle.

Research in the field of antibacterial effectiveness continues and, in the future, will be focused on PP woven fabrics modified by AMB nanosol with/without low-temperature plasma pre-treatment to exclude the influence of fabric construction on the antibacterial effectiveness.

REFERENCES

1. Borcia G., Anderson C.A., Brown N.M.D.: Surface treatment of natural and synthetic textiles using a dielectric barrier discharge, Surf. Coat. Technol., 201(6), 2006, pp. 3074 – 3081.
https://doi.org/10.1016/j.surfcoat.2006.06.021

2. Morent R., De Geyter N., Verschuren J., et al.: Non-thermal plasma treatment of textiles. Surf. Coat. Technol., 202(14), 2008, pp. 3427-344.
https://doi.org/10.1016/j.surfcoat.2007.12.027

3. Cerkez I., Worley S.D., Broughton R.M., et al.: Antimicrobial surface coatings for polypropylene nonwoven fabrics, React. Funct. Polyms., 73(11), 2013, pp. 1412-1419.
https://doi.org/10.1016/j.reactfunctpolym.2013.07.016

4. Cheng J.P., Chiang Y.P.: Surface modification of non-woven fabric by DC pulsed plasma treatment and graft polymerization with acrylic acid. J. Membrane Sci., 270(1-2), 2006, pp. 212-220.
https://doi.org/10.1016/j.memsci.2005.11.015

5. National Textile Center Research Briefs – Materials Competency. 2002. National Textile Center, Blue Bell. Accessed 26 June 2015.
https://www.ntcresearch.org/pdf-rpts/Bref0602/M01-CR01-02.pdf.

6. Špitalský Z., Kováčová M., Žigo O., et al.: Výskum vplyvu nízkoteplotnej plazmy na zvýšenie permanentnosti povrchovej úpravy textilných materiálov s použitím nanosólov - 69. Zjazd chemikov, 11. – 15. september 2017, Vysoké Tatry, Horný Smokovec; ChemZi 13/1, 6P06, str. 107 (2017)

7. Shishoo R. (Ed.): Plasma Technologies for Textiles. 1st ed. London: Woodhead Publ. Ltd., Cambridge, 2007.

8. Li, X.M., Reinhoudt D., Crego-Calama M.: What do we need for a superhydrophobic surface? A review on the recent progress in the preparation of superhydrophobic surfaces. Chem. Soc. Rev., 36(8), 2007, pp. 1350–1368.
https://doi.org/10.1039/B602486F

9. Špitalský Z., Rástočná-Illová D., Žigo O., et al.: Popypropylene fabrics pretreated by atmospheric plasma, In Proceedings of Odpadové fórum 2017: Výsledky výzkumu a vývoje pro prumyslovou a komunální ekologii, volume 12, Prague, Czech Republic, CEMC, 2017.

10. Parthasarathi V., Thilagavathi G.: Development of plasma enhanced antiviral surgical gown for healthcare workers, Fashion and Textiles, 2(4), 2015.
https://doi.org/10.1186/s40691-015-0028-7

11. Gao Y., Cranston R.: Recent advances in antimicrobial treatments of textiles. Test. Res. J., 78(1), 2008, pp. 60-72.
https://doi.org/10.1177/0040517507082

12. Windler L., Height M., Nowack B.: Comparative evaluation of antimicrobials for textile applications. Environ. Int., 58, 2013, pp. 62 -73.
https://doi.org/10.1016/j.envint.2012.12.010

13. Morais S.D., Guedes R.M., Lopes M.A.: Antimicrobial approaches for textiles: From research market, Materials, 9(6), 2016, pp. 1 – 21.
https://doi.org/10.3390/ma9060498

14. AATCC TM 100-2019. Test Method for Antibacterial Finishes on Textile Materials.

ONLINE WEAR ANALYSIS OF CARD CLOTHINGS

Fischer, Holger[1*]; Heilos, Katharina[2#]; Thal, Daniel[1]; Faasen, André[3] and Hofmann, Marcel[2]

[1] Faserinstitut Bremen e.V., FIBRE, Bremen, Germany
[2] Sächsisches Textilforschungsinstitut e.V. STFI, Chemnitz, Germany
[#] Present address: Chemnitz University of Technology, Chemnitz, Germany
[3] Graf Holland B.V., Enschede, Nederlands, present address: Spinning Jenny, Nijverdal, Netherlands

ABSTRACT

The processing of abrasive fibres in the carding process, in particular high-performance fibres such as glass, carbon or aramid fibres, can cause increased wear of the card clothing. In the FutureTex project 'HPF-Garnitur', the wear of card clothing was investigated and an online wear measurement system has been developed. The aim of the project was both, to optimize the clothings to enable gentler processing of the fibres, and to develop a digital monitoring system to observe the degree of wear of the clothings, which offers a new possibility for maintenance prediction and production planning in the sense of Industry 4.0.

KEYWORDS

Online analysis; Digital monitoring system; Industry 4.0; Wear level; Card clothing; Nonwoven; High performance fibres; Abrasion.

INTRODUCTION

Interval replacement of card clothings due to wear is well known. The wear is caused by the processing of fibres and results in loss of sharpness of the teeth, which affects the fibre transport during carding and reduces the nonwoven fabric quality up to the inability to work [1]. The clothing exchange is routinely carried out at certain maintenance intervals. Regardless of the wear of the individual clothings, the clothing of the entire nonwoven line is replaced in order to be able to continue production quickly without any further unexpected interruptions. This leads to unnecessarily frequent maintenance intervals.

Within the frame of the futureTex project 'HPF-Garnitur', a project team consisting of two institutes and four industrial partners considered the wear of card clothing due to the processing of high-performance fibres especially glass, carbon or aramid. Aim of the project was to prevent avoidable clothing changes by developing an online wear measurement system and to take a step towards industry 4.0. Before project start there have been approaches to check and evaluate the wear of clothings [1, 2], but an online analysis had not yet been developed.

The online analysis was developed by the project partner Faserinstitut Bremen e.V. — FIBRE, and was implemented on a pilot scale at Centre of Textile Lightweight Engineering at Sächsisches Textilforschungsinstitut e.V. — STFI. Subsequently it was tested at the nonwovens producers of the project consortium ASGLAWO technofibre GmbH, Hilbersdorf, DE, Norafin Industries GmbH, Mildenau, DE and TENOWO GmbH, Hof, DE, for industrial scale-up. The team was supported by the project partner Graf & Cie AG, Rapperswill-Jona, CH which provided technical support in wear evaluation and derived measures to optimize the clothings for processing of high-performance fibres.

To improve the clothing and make it not only more efficient but also more resistant to wear, optimisation of the profile shape [1, 3] or clothing surface [4] have been considered.

MATERIALS AND METHODS

Card clothing

Besides the number of carding stations (number of worker-stripper pairs), the geometry of the clothing has a major influence on carding process. [5]. Figure 1 shows the most important clothing dimensions. Clothing can be characterized by its tooth geometry, tip shape and tooth density. The angles shown in Figure 1, i.e. the working angle, the front angle and the back angle, are used to describe the tooth geometry, but also the tooth depth or working depth [6]. The working angle enables the fibres
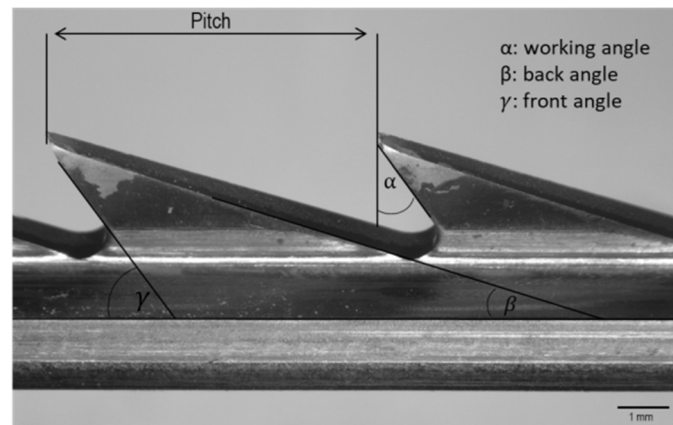
Figure 1. Description of card clothing using the example of VD5030-12 of Graf & Cie AG. Naming convention according to [5, 6, 7, 8].

to be picked up as well as held and thus significantly influences the fibre loading of the cylinder [6]. The back angle is responsible for tooth stability and also influences the tooth depth. The tooth depth mentioned is made up of the length of the back angle, the radius of the tooth root and the distance between the tooth root and the base of the clothing. The tooth depth is decisive for the holding capacity of the tooth, i.e. for the fibre loading of the cylinder.

Besides the tooth geometry, the tip shape is important. It is described by tip width and tip length. Most demanded are pointed tooth shapes that allow targeted penetration into the fibre mass with minimal fibre-metal friction. However, a lacy tip shape also carries the risk that the tooth has lower resistance properties and wears or breaks more quickly [6]. The change of the shape of the tip, e.g. due to wear, can lead to poorer penetration into the fibre flock and therefore also to lower fibre resolution, which massively impairs the working ability of the clothing [6]. This has already been demonstrated in some studies [1, 2], which observed the loss of sharpness of the teeth due to a rounding of the tips.

Based on these investigations, special attention is paid to the tip of the teeth in this study. Another important characteristic of clothing is the tooth density. Depending on the fibre type (especially fibre density) to be processed, different clothings are used. The tooth density can be described with the help of the pitch and base width of the wires. Pitch is defined as the number of tooth tips per inch along the clothing wire. Generally, clothing for fine fibres display high tooth densities [6].

To achieve a good carding result, the tip density increases as the opening of the fibre flock increases. I.e. the number of tips increases in the course of the carding process [5]. Thus, opening cylinders generally have a lower number of points than workers, for example. This leads to different tooth sizes and must be considered for an image analysis.

In the case of clothing for processing glass or (recycled) carbon fibers, clothings with a low tip density are used. I.e. the tip density on the line used

at STFI is approx. 48 tips/inch² [9, 10]. On the one hand, this can be explained by the shape of the CFs, which are available as textile waste (e.g. offcuts) and therefore entangled in comparison to staple fibre. On the other hand, lower tooth tips allow gentler processing of the brittle CF.

During the project different clothing geometries have been considered represented by the diverse carding configurations resp. purposes of application of the partners. One of the regarded clothing is the clothing of the MiniCard unit from Autefa Solutions Germany GmbH, Friedberg, DE at STFI, which is primarily used for processing recycled carbon fibres [11, 12]. In the project the clothing of the first and the last worker-stripper pairs (from a total of 3 pairs) were exchanged to investigate the wear of the clothing (VD5030-12, Graf & Cie AG) shown in Figure 1. Flexible Card clothings were not investigated within the project, as they are not common in the field of producing nonwovens based on high-performance fibres.

Sampling positions

Focus of the project was the wear of card clothing. During the carding process, the fibres are transferred from the cylinder to the worker and via the stripper back to the main cylinder [5, 6]. Particularly the fibre flock disintegration and increasing parallelization between cylinder and worker due to the different cylinder speeds leads to a strong stress on the clothing. The clothings of worker and stripper pairs as well as the main cylinder were examined more intensively, because from experience of the partners the main wear occurs on them. Besides the mentioned cylinders, also opening cylinders, swirling cylinders and transfer cylinders have been investigated in the project.

Offline analysing methods

Three different approaches of analytical methods have been used: offline analysis, semi-online analysis, and finally online analysis. In offline analysis individual clothing pieces are examined more closely using a light microscope (Digital microscope VHX 1000, Keyence Deutschland GmbH, Neu-Isenburg,
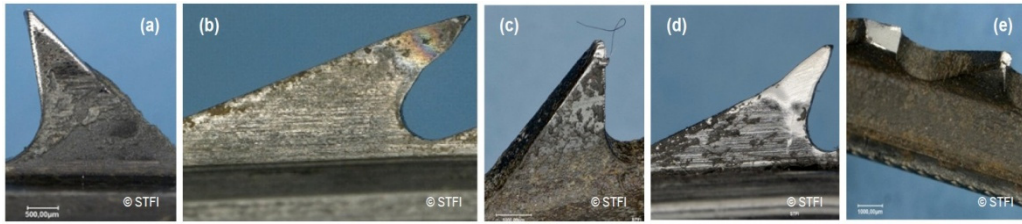
Figure 2. Optical microscopy images of various anomalies of clothing at STF and at partners: (a) polluted tooth, (b) discolored tooth tip, (c) split tooth tip, (d) deformed tooth, (e) missing tooth.

Figure 3. Regrinded tooth tip of a clothing, top view.

DE) or SEM (QuantaTM 250 FEG, FEI Company; Hillsboro, Oregon, US). In semi-online analysis by USB-Microscope (USB2-MICRO-200x USB2.0 microscope, Plugable Technologies, Redmond, US) card clothings were evaluated directly on the carding unit, i.e. non-destructively. Semi-online analysis in particular is used in industry and is currently state of the art. Some companies therefore offer corresponding USB microscopes in their product range [8, 13]. However, trained specialists are needed to assess the condition of the clothing using USB microscopes.

Online analysis

An online analysis was developed at the project partner FIBRE. The aim was to optimize the current semi-online analysis and to take a step towards Industry 4.0. The system was based on a 20 MP industrial camera exo541MGE (SVS Vistek, Seefeld, DE) and MC3-03X lens (Opto Engineering, Mantova, IT) mounted in an IP67 housing to prevent damages by carbon fibre dust. The image area observed is approx 25 x 25 mm² at 4504 x 4504 pixel, corresponding to an edge length of approx 5.5 µm per pixel. This enables the observation of the card clothings in nearly microscopic scale on the one hand, and the observation of slowly moving cylinders on the other hand, if the linear movement is smaller than half of a pixel width per exposure time (i.e. less than 2.75 µm in 500 µs / speed <5.5 mm/s in the configuration reported here). The camera was mounted on a rack constructed from aluminium profiles allowing a positioning over lines up to 3 m working width. The camera holder was movable forward and backward by a stepper motor to enable

focusing by remote control. A Justbright JBBL-0506-WT LED illumination unit (MBJ Imaging GmbH, Ahrensburg, DE) with 800 lm luminous flux was directly attached to the camera holder. The camera holder was connected to the rack by a linear guiding (Kamp & Kötter, Dortmund, DE) to enable easy manual position change in parallel to the observed cylinder. The software was self-developed based on the opencv SDK (https://opencv.org/), using the findContours() function. The function uses the algorithm developed by Suzuki and Abe [14]. Additional details of the development are described in section Online wear analysis.

CLOTHING DAMAGE AND WEAR DETERMINATION

Offline analysis of clothing damage

Offline analysis enables a closer look at the card clothing. It allows determination of the cause and evaluation of the intensity of wear or damage. The analyses were carried out using the above-mentioned methods. During the course of the project, it was possible to identify various anomalies of clothing at STFI and at the partners' lines. These are sorted according to their degree of damage and shown in Figure 2. As displayed in Fig. 2, the teeth of different clothing show contaminations (dust and fibre fragments), tooth discoloration, split and deformed teeth and even missing teeth. Polluted teeth mainly occur on opening cylinders and (as in this case, shown Fig. 2(a)) pre-cylinders. This can be explained by the fact that the fibre flocks are first opened by the opening and pre-cylinders, and the fibre-fibre and fibre-metal friction can deposit lubricants
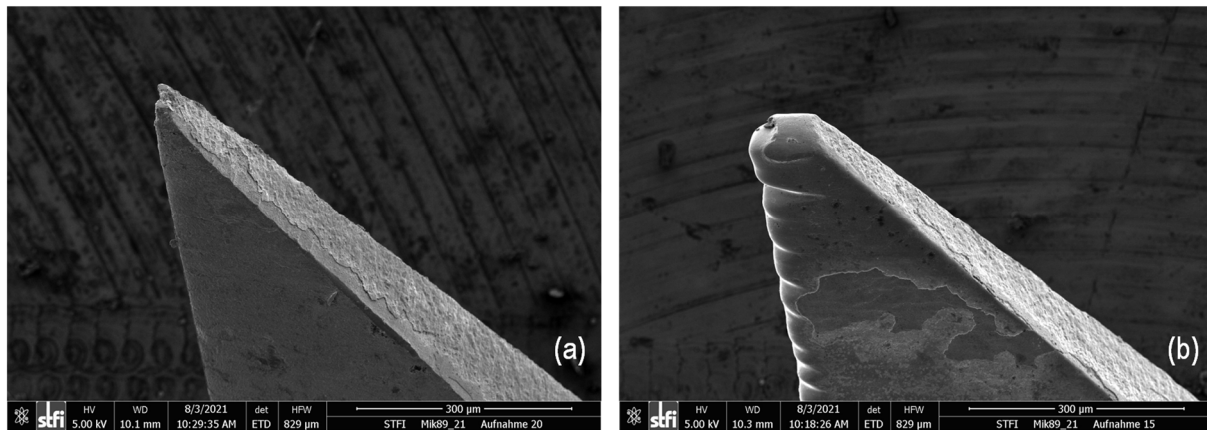
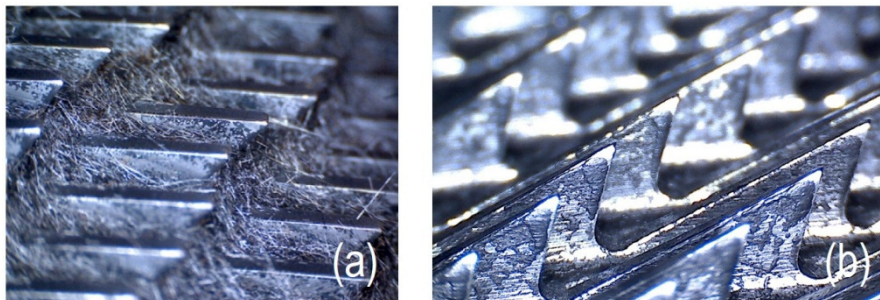**Figure 4.** SEM images of tambour clothings: (a) new and (b) worn.

Figure 5. USB-Microscope images of: (a) Fiber accumulation on the clothing of a feed cylinder and (b) sediments on the clothing of a pre-cylinder.

or sizing agents on the clothing when they first come into contact with them. The lubricant residues may lead to undesirable stickiness, which causes increased adhesion of fibres and contaminants to the clothing. In extreme cases, this can lead to 'clogging' of the cylinders, which makes cleaning of the cylinders unavoidable and thus leads to unwanted maintenance work and unplanned process stops. For this reason, the condition of the clothing must also be examined with regard to possible contamination.

Another anomaly identified was the discoloration of individual teeth, shown in Fig. 2 b; on a tooth of a worker clothing at STFI. Due to a regrinding process, some tooth tips experienced partial overheating, which caused an extreme heat exposure on individual tooth tips and leads to discoloration of the metal. The regrinding process can also be confirmed by Fig. 3, which shows one of the reground teeth and thus clearly the traces of grinding due to the changed tooth tip. All teeth are evenly ground at the tip.

Furthermore, damage to the tooth tips and teeth could be determined. This includes split tooth tips (Fig. 2 c) as well as deformed teeth (Fig. 2 d) and even missing teeth (Fig. 2 e). These damages can be traced back to foreign bodies (metal parts) in the process. Not every conspicuous feature must necessarily lead to a change of clothing. In particular, pollution like dust or fibres can be easily removed by cleaning, so that maintenance is necessary, but there is no need for a replacement of the clothing.

Furthermore, the offline analysis made it possible to investigate where the most wear occurs on the tooth.

As in literature discussed and already mentioned above, the wear of clothing was especially seen on tooth tips and front angles due to the mechanism of the carding process [1, 4]. For this reason, SEM images of new clothing, i.e. clothing before their use in the carding process, and old clothing, which already had to be replaced due to their wear, were to be compared with each other.

SEM images showed both, the extreme case of a rounding of the tooth tips, already described in the literature [1, 4] and deep indentations caused by fibres working into the metal of the teeth occurring before the rounding of the tooth tip. The investigations confirmed that especially the tip of the tooth but also the front angle are affected by abrasion, shown in Figure 4 using the example of a tooth of a clothing of a main cylinder. Due to the role of the main cylinder during the carding process, the abrasion effects were clearly visible. The tip is already completely rounded and clear scoring is visible on the breast angle.

Semi-online analysis of clothing damage

A semi-online analysis using an USB-microscope is a non-destructive method for determining wear. This analysis offers the possibility to evaluate abnormalities, which can only be seen inline. These include, for example, contamination of high fibre accumulation (see Fig. 5), the degree of which must be assessed on the system in order to schedule maintenance rep. cleaning in production.

Such information also makes it possible to assess the interaction between fibre and clothing, i.e. the
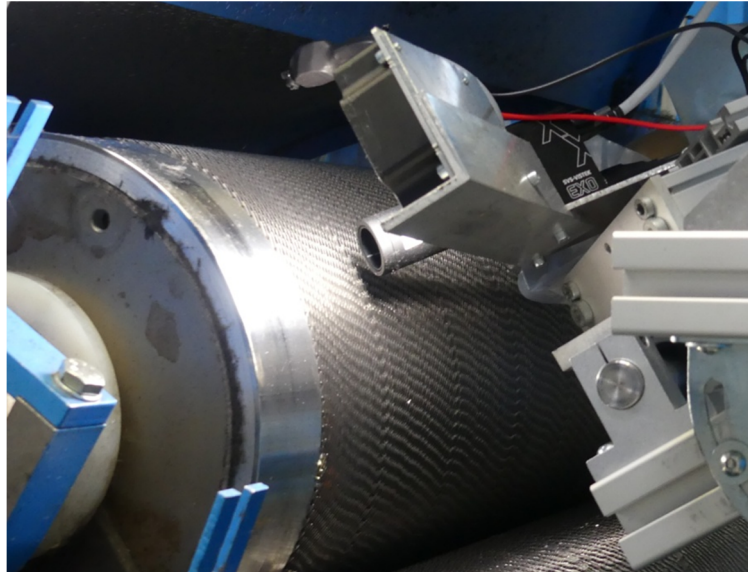
Figure 6. Experimental setup used for online measurement at the carbon fibre pilot plant of STFI.

processability of the fibres used. This for example can lead to fibre changes due to their sizing, as this adheres particularly strongly to the clothing. Furthermore, the number of wear anomalies is decisive. Single damaged teeth do not significantly influence processing, but may indicate further damage or undesirable metal parts in the process, underlining the necessity of considering the entire clothing. The analysis of the card clothing using an USB-Microscope is neither exact, nor it is comprehensive. Main restrictions are the exposure at different angles, which can lead to distortions of the teeth and thus to a false assessment, as well as the varying illumination, preventing a reproducible statement about the condition of the teeth. In addition, it is not possible to observe the complete surface of a cylinder reproducibly.

At the moment, only trained specialists are able to view and evaluate clothing conspicuities appropriately on the basis of many years of experience. Data collection and documentation are done manually and therefore cannot be integrated in the sense of Industry 4.0. Preliminary tests at STFI using an USB-Microscope highlighted the requirements for an online wear measurement:

- preventing distortions by using a constant recording angle,
- development of a suitable illumination concept to prevent unwanted reflections,
- focusing multiple teeth to evaluate larger areas.

ONLINE WEAR ANALYSIS

An online analysis was developed at the project partner FIBRE. The analysis system is essentially based on a digital industrial camera with a suitable lens and a lighting arrangement designed for this purpose (see Figure 6).

The system is mounted on a frame and thus enables the reproducible approach of measuring positions. The camera position is approx. 2 mm above the tooth tips. This distance is sufficient to prevent damages on camera or clothings during operation. Image acquisition is done using a laptop connected to the camera via Gigabit ethernet. The evaluation of the recorded images is carried out by means of analysis software developed at FIBRE. From the original image, the teeth of the clothing in the focus area are marked and evaluated by means of edge detection. For a correct evaluation it is essential that at least three rows of teeth over three teeth are in the focus area. If the cylinder diameter, tooth distance (pitch) and height are known, the front and working angles can be calculated from the image, and edge breakouts or damaged tips can be detected. The side surfaces of the teeth do not have to be completely visible in the image, but the edges must all be recognisable. The lighting is placed to illuminate mainly tip and upside of the teeth, and to a certain extent the side opposite to the camera. The camera is mounted in a 45 degree angle with view to the non-illuminated side of the teeth. Consequently, the side surface of each tooth appears dark, whereas the tips and edges are strongly illuminated and appear in a high contrast to the dark side surface. The optimum image position depends on the cylinder diameter and tooth angles, is therefore cylinder-specific and can only be determined on site on the device if necessary. First orienting experiments to validate the system have been conducted at the lab-scale line (30 cm working width) at FIBRE.

First scale up at STFI

The first step of scale up was done by switching to the dust-proof pilot plant with 1 m working width at the Centre of Textile Lightweight Engineering at STFI, Chemnitz, DE, described in section Card clothing. In Figure 7 the scheme of image analysis used in the
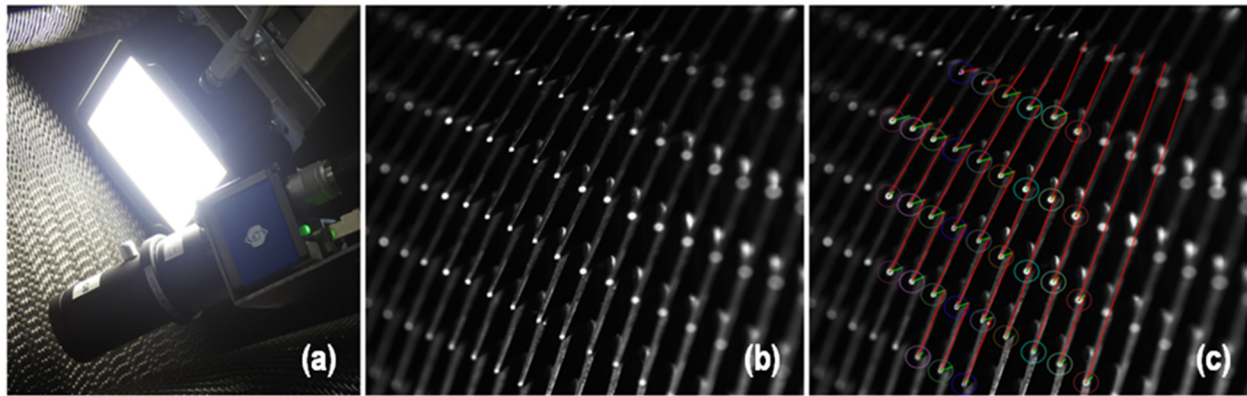
Figure 7. image analysis system with camera & illumination unit (a), original image of worker #3 (b) and clothing with edges marked in focus area after edge detection (c).
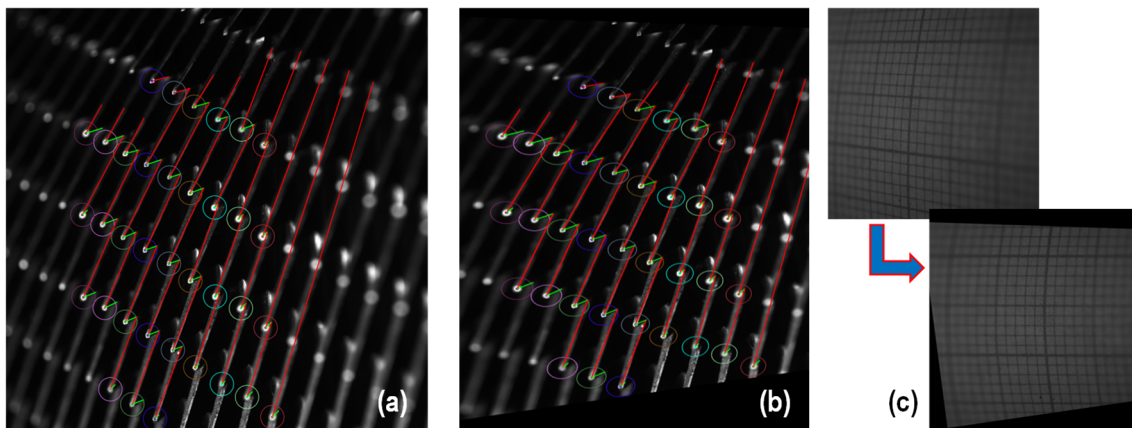

Figure 8 original image after edge detection (a), after perspective correction (b), and assisting grid to visualise the effect of perspective correction (c).

project is displayed with the camera system positioned in the card (a), consisting of industrial digital camera and a LED illumination unit. In (b) an original image recorded on worker #3 is displayed. First step of analysis is to determine the clothing lines within the focus area. For this purpose, the tooth tips are determined by the algorithm using binarisation. This is possible, since the tips appear as spots characterised by the largest gray scale values in the image, typically values exceeding the average by more than 100 (8-bit gray scale, allowing values 0 – 255). Subsequently, the teeth are grouped by wire, as displayed in Fig. 7(c). In the next step a region of interest is defined per tooth and the tooth edges are searched in this region. For all teeth with two edges detected (i.e. back and front edge), the tip is marked by a green circle as valid tooth. The result is shown in Figure 7(c).

Finally, additional information is necessary (i.e. cylinder diameter, clothing teeth distance and tooth height) in order to calculate correct angles from the visible edges in the image. Using this input, a perspective correction can be conducted on the images to bring all visible teeth within the focus area to identical size and geometry. In Figure 8 are displayed: the original image after edge detection (a), the converted image after perspective correction (b) and an assisting grid to visualise the effect of

perspective correction (c). In Figure 8 (b) the tip angles are displayed distortion-free and can thus be used for further evaluation.

Final scale-up to industrial scale

The same measurements have been conducted on the lines of three industrial partners covering processing of aramid, glass and carbon fibres. Corresponding to the variety of the processed materials, each of the lines has a different configuration concerning number of stripper-worker pairs, pre- and post-groups, cylinder geometries and of course in clothing geometries. Thus, each of the systems must be assessed individually in terms of wear level detection. In other words: the database acquired here is too small to derive a general approach for wear level detection of all clothing types. But the results acquired here give a good insight into several wear mechanisms and can be used as base for future developments. As example the wear of a tambour clothing is displayed in Figure 9. The images were recorded before and after exchange of the clothing during a scheduled maintenance to visualise the maximal detectable difference. In Figure 9 (a) the 'old' worn clothing is displayed, compared to the new clothing directly after installation (b). Both parts of Figure 9 comprise a general view on the clothing plus an enlarged section to visualise the details of one of the teeth. In (b) the complete tip with sharp edges
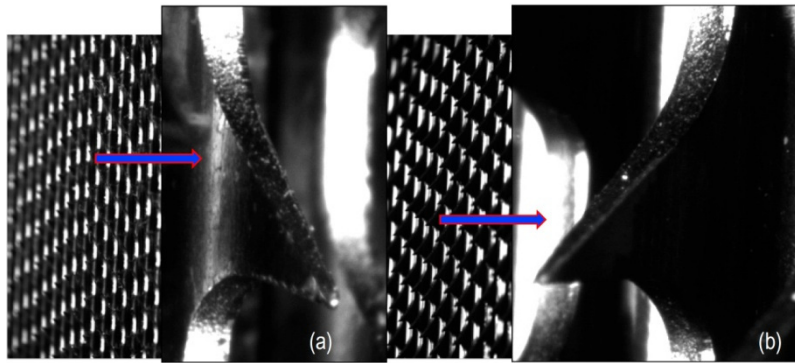
Figure 9. tambour clothing (a) worn, after exchange and (b) new, directly after installation.

over the full tooth is visible, whereas in (a) the worn tip displays the typical signs of wear. It is easy to observe that the worn tool tip is rounded, and several corrugations have been grinded into the front edges by contact with the processed fibres. The intensity of the corrugations increases in direction to the tip. The next step of this wear mechanism would be cutting off the tip completely, i.e. reducing tooth height and tip geometry / tip angle. From this point of wear the product quality would be influenced remarkably.

A microscopic off-line assessment of the old clothing would lead to the result, that the clothing is still usable, but should be exchanged in the near future.

This result is in concordance with the off-line analysis by SEM displayed in Figure 4. The detected wear signs obtained from different lines are identical. This gives evidence, that the resolution of the image analysis system with industrial camera used here is high enough to detect the wear patterns occurring on industrial roller cards. Furthermore, it opens as well the way to analyse and quantify the detected wear.

CONCLUSIONS

Summed up the developed image analysis system is suitable to analyse the wear of card clothings:

- The teeth of card clothings are well-detectable by image analysis.
- BUT: the optimal camera position depends on cylinder diameter and tooth geometry / tooth angles. I.e. the camera positioning is cylinder-specific. Thus, generally it must be determined at the machine.
- Back-, front- and working angle as well as damaged edges and tips are detectable.
- Starting at tip positions, the edge detection in combination with perspective correction (cf. Fig. 7 & 8) enables a reproducible analysis.

The described method of image analysis had been integrated into the pilot plant line at STFI and was tested several times on the lines of three partner companies. Now, at the end of the project it has reached the state of 'proof of concept'. Detailed results of the project have been published in German as final report [15].

Actually, the system described here is a proof of concept. It must be positioned over an existing line while the maintenance doors are opened to enable viewing the card clothings. This makes the analysis possible only during the scheduled maintenance intervals, i.e. approx. each two weeks, which is sufficient to observe the increase of wear. This has the general advantage, that the line is cleaned during the maintenance, thus preventing erroneous measurements caused by remaining fibres on the clothings. For future industrial use, further development of the system will be necessary. This must include building up a database for at least the cylinder geometries and card clothing types to be observed, comprising data about typical wear patterns and limits of clothing usability. This must be combined with data for optimal camera positioning for each occurring combination of cylinder geometry and clothing used on it. Then it will be possible to bring the system to industrial usability.

REFERENCES

1. Atkinson K.R.: Design, function, and applications of high-retention doffer and worker wire, Textile Research Journal, 84(8), 2014, pp. 881–894.
https://doi.org/10.1177/0040517514523179
2. Wu L., Wang W., Ni H.: A view on wear mechanism of metallic card clothing, J. Donghua Univ., 25, 2008, pp. 324–327.
3. Hasler F.: Metallic card clothing with positive influence, Melliand International, 2, 2014, p. 81.
4. Wei D., Li F., Li S., et al.: A new plasma surface alloying to improve the wear resistance of the metallic card clothing, Applied Sciences, 9, 2019, p. 1849.
5. Schlichter S., Rübenach B., Morgner J., et al.: Trockenverfahren - Vliesstoffe: Rohstoffe, Herstellung, Anwendung, Eigenschaften, Prüfung, 2012, pp. 123-228.

6. Brydon, A. G., & Pourmohammadi, A.: Dry-laid web formation (pp. 16-111). Sawston, UK: Woodhead Publishing. In Russell, S. J. (Ed):. Handbook of nonwovens, 2007.

7. Anonymous: Groz-Beckert AG: Carding-card clothing for the nonwovens industry, 2021.
https://www.groz-beckert.com/mm/media/en/web/pdf/Card_clothing_for_the_nonwovens_industry.pdf , accessed 2022-03-03

8. Anonymous: Graf & Cie AG: Carding-Accessoires for setting flat cards, 2017.
https://www.graf-companies.com/fileadmin/graf/Products_new/Carding_new/88001307_Carding_EN.pdf, accessed 2022-03-03

9. Hengstermann M., Raithel N., Abdkader A., et al.: Development of new hybrid yarn construction from recycled carbon fibers for high performance composites. Part-I: basic processing of hybrid carbon fiber/polyamide 6 yarn spinning from virgin carbon fiber staple fibers, Textile Research Journal, 86(12), 2016, pp. 1307 – 1317.
https://doi.org/10.1177/0040517515612363

10. Moebitz C., Cloppenburg F.: Abschlussbericht MAI RecyTape – Prozesslinie zur herstellung von tapes aus hochorientierten Recycling-Carbonfasern. Institut für Textiltechnik der RWTH Aachen, 2017.
https://doi.org/10.2314/GBV:1010765566

11. Fischer H., Heilos K., Hofmann M., Miene A.: Second life for carbon fibers — re-use of recycled carbon fibers in sophisticated composite parts. Kunststoffe International 109(12), 2019, pp. 46-49.

12. Heilos K., Fischer H.; Hofmann M., et al.: Nonwovens made of recycled carbon fibres (rCF) used for production of sophisticated carbon fibre-reinforced plastics, Vlakna a Textil, 27(3), 2020, pp. 65 – 75.

13. Anonymous: Groz-Beckert AG: Accessoires, 2021, https://www.groz-beckert.com/mm/media/en/web/pdf/Accessories.pdf

14. Suzuki S., Abe K.: Topological structural analysis of digitized binary images by border following, Computer Vision, Graphics, and Image Processing, 30(1), 1985, pp. 32 – 46.

15. Fischer, H.; Heilos, K.; Hofmann, M.; et al.: HPF-Garnitur — Verbesserte Qualität für Vliesstoffe aus Hochleistungsfasern bei längerer Standzeit durch optimierte Krempelgarnituren und angepasste online Überwachung. In series: Forschungsberichte aus dem Faserinstitut Bremen 69. Books on Demand GmbH, Norderstedt, DE, September 2022, 48 pp. ISBN 978-3-75624-201-6.

IMPROVE BUILDING DATABASE ON THE OPERATION PROCESS AND PERFORMANCE TIME FOR SEWING OPERATIONS OF KNITTED GARMENT PRODUCTS

THAO, PHAN THANH* AND PHAN, DUY-NAM

Hanoi University of Science and Technology, Hanoi 10000, Viet Nam

ABSTRACT

This paper presents the findings of the study of building and completion of a standard database on the operation process and sewing time for 02 typical products from knitted fabrics, namely Polo-Shirt and T-Shirt. The study process is carried out based on applying MTM (Methods Time measurement) standard time analysis method and predetermined time system GSD (General Sewing Data). In this research, we have inherited the results from previous studies including Classifying the main parts sewing linkages, formulated sewing technology process and theoretical analysis of the process of manipulating sewing of the main parts, linkages of the 02 classical textile products including Polo-Shirt and T-Shirt by MTM standard time analysis method and GSD predetermined time system; The studies work of the group of authors on the experimental research content determines the simultaneous influence of a group of factors: distance to place the sewing element (cm), the rotation angle of the sewing element (˚), the size of the sewing element, the number of element layers involved in the sewing, the light intensity (lux) and the skills of sewing workers (grade worker) to the sewing time of knitting products and research simultaneous influences of a group of technological factors including: seam length (cm) and stitches per centimeter (stitches/cm), experiment on 4 sewing devices such as 1-needle lockstitch machine, overlock machine (1 needle and 3 threads) and (2 needles and 4 threads), coverstitch machine (2 needles and 3 threads); and with 3 kinds of single jersey fabrics, which are thin, medium, and thick fabrics to sewing time on the machine of Polo-Shirt and T-Shirt products. The above research results show that there is a big difference between the actual values and theoretically calculated values according to MTM method, GSD predetermined time system, the authors have determined a set of adjustment coefficients for the former and the latter for two values of sewing preparation operation time and sewing time on the machine. We have tested the above research results in 03 enterprises: Hanoi Star Fashion Co., Ltd., Tinh Loi Garment Company and Ha Nam Hanosimex Company Limited and received a lot of practical comments from businesses.

KEYWORDS

Motion study; Time study; GSD; MTM; Database; Knitted garment products.

INTRODUCTION

Industry 4.0 has been spreading globally, strongly affecting all social life activities, including the textile industry. The application of scientific and technological achievements to production is labor - the most effective solution to increase labor productivity, reduce production costs and increase the competitiveness of enterprises. The introduction of MTM standard time analysis method and GSD predetermined time system marked a new step in improving the time and process in manufacturing. But it is always a time difference between standard sewing operation procedure and actual production. Because the labor level is still low, mainly blue-collar workers, there are many redundant operations in the production process, leading to large processing times and low productivity. Realizing this, the author has built a database on the operation process and sewing time of typical knitted products, namely Polo-Shirt and T-Shirt. This database is a manual to help businesses come up with a reasonable sewing process and time by actual production conditions.

Currently, there have been several research works on this issue. Habibur Rahman et al. [1] has researched analyzing the movements and actions of garment workers. Phan Thanh Thao et al. [2] has studied the factors affecting productivity in garment industry enterprises. Phan Thanh Thao et al. [3] researched and proposed solutions to improve garment workers for operation and working speed. Dinh Mai Huong et al. [4] studied the influence of the sewing process on productivity. Phan Thanh Thao et

---

al. [5] have built a database on the operation process and sewing time of knitted products. Dinh Mai Huong et al. [6] studied and built the adjustment coefficient for preparation and sewing time on the machine of GSD and MTM, sewing products from knitted fabrics in Vietnamese conditions.

In this article, the authors present the research results of building a complete database on the operation process and execution time of sewing two typical knitted products: Polo-Shirt and T-Shirt with the following contents:

- Synthesize the data set on the operation process and sewing time (the preparation sewing tp and the sewing time on machine tm) from previous studies.

- Collecting actual data on the sewing technology process and time of detail assemblies, seams of two products, and conducting a comparative analysis of the operation process and sewing time of data each pair obtained from Hanoi Textile and Garment Joint Stock Corporation in Ha Nam (Hanosimex) and Tinh Loi Garment Company Limited with the results developed by the research team BKG (Bach Khoa Group).

Proposing a complete database on the operation procedure and the sewing time (sewing preparation time *tp* and time on machine *tm*) reasonable to detail assemblies, and seams of Polo-Shirt and T-Shirt products under different manufacturing conditions. From that, progress to complete the database for all detail clusters, seams of two product categories Polo-Shirt and T-Shirt.

EXPERIMENTAL

Research subjects

Theoretical research object

Polo-Shirt and T-Shirt products in theoretical research are inherited from previous research works of the authors [6]. These products have a structure of detailed clusters and seams that ensure the diversity, richness, and universality of all technological structural options of the Polo-Shirt and T-Shirt product categories and are suitable for actual garment enterprises as presented in Table 1.

Experimental research object

Selected subjects for the experimental survey were Polo-Shirt PE19, T-Shirt DHA19-024/OCKS0025 manufactured at Hanosimex and Polo-Shirt with code DC1963, T-Shirt with code 142N212 at Tinh Loi Garment Co., Ltd. To maintain brevity, we refer to Polo-Shirt PE19 and T-Shirt DHA19-024/OCKS0025 as P1 and T1, respectively, and Polo-Shirt DC1963 and T-Shirt 142N212 at Tinh Loi Garment Co., Ltd as P2 and T2, respectively.

Research Polo-Shirt has the following characteristics:

- P1, Figure 1 (a): Closed collar without legs, woven neckband, body fabric neckline, skewed placket, 2-needle chains bottom hem and sleeve opening. Fabric used for sewing is Single fabric with material composition: 55% cotton mixed with 45% polyester, weight: 180 g/m^2, horizontal density: 130 (column loops/100 mm), vertical density: 210 (row loops) /100 mm), fabric thickness: 0.15 (mm), yarn count: Ne = 18 (m/g).

- P2, Figure 1 (b): Closed collar without legs, woven neckband, woven tape neckline, fold of edge placket and skewed placket, 2-needle chains bottom hem and sleeve opening. Fabric used for sewing is Single fabric with 100% polyester material composition, weight: 145 g/m^2, horizontal density: 150 (column loops/100 mm), vertical density: 210 (row loops/100 mm), fabric thickness: 0.15 (mm), yarn count: Ne = 18 (m/g).

Researched T-Shirt T1 and T2, Figure 1 (c) produced at both factories, have the following characteristics: Rib neckline folded in half, back neck binding, sew label to side seam, 2-needle chains bottom hem and sleeve opening. Fabric used for sewing is 1x1 Rib fabric with 100 % polyester material composition, weight: 149 g/m^2, horizontal density: 180 (column loops/100 mm), vertical density: 445 (row loops/100 mm), fabric thickness: 0.146 mm, yarn count: Ne = 19 m/g.

Research methods

To complete the construction of a database on the operation process and sewing time of Polo-Shirt and T-Shirt products, the team used the following research methods [7]:
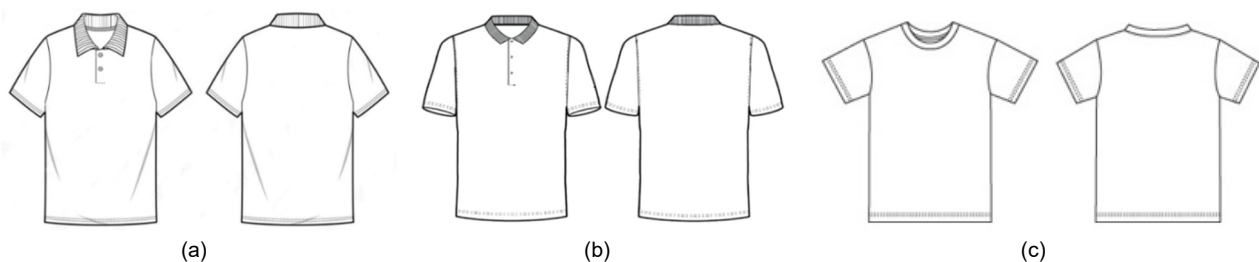
Figure 1. Product description of (a) Polo-Shirt code PE19 – P1, (b) Polo-Shirt code DC1963 – P2, (c) T-Shirt produced at both enterprises T1 and T2.

Table 1. Detailed assembly, seams classification table of 2 Polo-Shirt and T-Shirt products.

Collar assembly	T-Shirt: - Rib neckline folded in half, back neck binding - Neck facing (leg opening) - Neck facing (leg folded) - Collar uses edge tape - Collar uses blind		Polo-Shirt: - Closed collar without legs, woven neckband, woven tape neckline - Closed collar without legs, woven neckband, body fabric neckline - Closed neck with legs, woven neckband - Closed neck with legs, body fabric neckband	
Placket assembly	- Symmetrical placket and fold edge - Symmetrical placket and open edge - Skewed placket and open edge - Skewed placket and fold edge - Placket has zipper		Slit assembly	- Open edge slit - Close edge slit - Slit facing
Pocket	- Pocket with no flap - Double welt pocket		Bottom	- Coverstich bottom
Sleeve opening	- 2-needle cover stitch sleeve opening - Sleeve has cuff facing fold in - Sleeve has cuff facing - Sleeve cuff		Seams	- Shoulder seam - Armhole seam - Side seam, Sleeve seam

To complete the construction of a database on the operation process and sewing time of Polo-Shirt and T-Shirt products, the team used the following research methods [7]:

- Method of building technological process of sewing products.

- Method of document research: inheriting the research results on building a database of the authors sewing technology processes for 27 detailed assemblies, the seams of two the product and determining the set of adjustment coefficients for the actual sewing time value compared to the theoretical calculation time for two values of sewing preparation operation time *tp* and sewing time on the machine *tm*.

- Experimental survey method: recording and taking pictures to record sewing operations performed by workers. After that, analyze, evaluate, compare and collect data on the operation process and reasonable sewing time.

- Using the interpolation method to get a complete data set for all detailed assemblies, seams that have not been implemented experimentally.

The authors conduct data analysis, processing and comparing the operation process and sewing time of the detail assemblies and seams obtained from Hanosimex and Tinh Loi Garment Co., Ltd. to build the research results. From there, a reasonable database on the operation process and sewing time are proposed for four experimental research products, namely P1, P2, T1, and T2.

Due to a large amount of processed data, the article represents the research results analysis of the process theory and the time to perform the armhole seam operation of Polo-Shirt and T-Shirt by MTM and GSD method, applying a set of adjustment coefficients on time values, empirically surveying workers at Hanosimex and Tinh Loi Garment Co., Ltd., compare the theoretical and experimental analysis to propose a complete data set on the operation process and sewing time to perform a reasonable armhole seam of Polo-Shirt and T–Shirt for traditional and modern companies.

RESULTS AND DISCUSSION

The results of theoretical analysis of armhole seam using time value adjustment coefficients of 2 products Polo-Shirt and T-Shirt

Table 2 presents the theoretical analysis result of the operating procedure of armhole seam according to MTM and GSD combined with the application of a set of adjustment coefficients on the time value researched by our team.

Analysis results of the operation process and sewing time to sew Polo-Shirt products at Tinh Loi Garment Co., Ltd and Hanosimex

Table 3 and 4 present the empirical analysis results of the operation process and sewing time of armhole seam following MTM and GSD methods at Hanosimex and Tinh Loi Garment Co., Ltd.

Sum comparing the time value to perform the operations of sewing polo-shirt and t-shirt products at tinh loi garment co., ltd and hanosimex with the research team results

Based on the motion analysis process, companies can be easily divided into two groups:

- Group 1: Traditional company (Hanosimex): using traditional sewing methods, heavily dependent on human factors.

- Group 2: modern company (Tinh Loi Garment Co., Ltd.): using modern equipment, and templates to support production to minimize the dependence of motion on humans.

Table 2. Results of theoretical analysis of armhole seam.

No.	Description	CODE	Freq.	GSD	BKG
1	*Match & get two parts separately*	MG2S	2	107	128
2	*Put to foot*	FOOT	2	38	46
3	*Align & reposition assembly under foot*	ARPN	2	75	150
4	*Sewing 20cm-curved-non visible seam*	S20MA	2	79	104.3
5	*Adjust*	AJPT	2	43	86
6	*Sewing 5cm-curved-non visible seam*	S5MA	2	32.5	53.4
7	*Adjust*	AJPT	2	43	86
8	*Sewing 20cm-curved-non visible seam*	S20MA	2	79	104.3
9	*Adjust parts by pushing*	APSH	2	24	48
10	*Sewing 13cm-curved-non visible seam*	S13MA	2	57.5	80.5
11	*Cut thread automatic*	F	2	9	9
12	*Aside part with one hand*	AS1H	2	23	28
13	*Get part with two hands*	GP2H	2	33	35
14	*Put to foot*	FOOT	2	38	46
15	*Align & reposition assembly under foot*	ARPN	2	75	150
16	*Sewing 20cm-curved- visible seam*	S20HA	2	112	97.3
17	*Adjust parts by pushing*	APSH	2	24	48
18	*Sewing 5cm-curved- visible seam*	S5HA	2	40.5	41.5
19	*Adjust parts by pushing*	APSH	2	24	48
20	*Sewing 20cm-curved- visible seam*	S20HA	2	112	97.3
21	*Sewing 13cm-curved- visible seam*	S13HA	2	78.5	71.2
22	*Cut thread automatic*	F	2	9	9
23	*Aside part with two hands*	AS2H	2	42	50
	Sum (TMU)			**2396**	**3233.6**

Unit: TMU (Time Measuring Unit)

Table 3. Analysis results of the operation process and sewing time to armhole seam at Hanosimex.

No.	Description	CODE	Freq.	GSD	BKG
1	*Get part with two hands*	GP2H	2	33	35
2	*Put to foot*	FOOT	2	38	46
3	*Get part with two hands*	GP2H	2	33	35
4	*Put to foot*	FOOT	2	38	46
5	*Align & reposition assembly under foot*	ARPN	2	75	150
6	*Sewing 20cm-curved-non visible seam*	S20MA	2	79.72	104.32
7	*Adjust*	AJPT	2	43	86
8	*Sewing 5cm-curved-non visible seam*	S5MA	2	32.68	53.42
9	*Adjust*	AJPT	2	43	86
10	*Sewing 20cm-curved-non visible seam*	S20MA	2	79.72	104.32
11	*Adjust parts by pushing*	APSH	2	24	48
12	*Sewing 13cm-curved-non visible seam*	S13MA	2	57.77	80.56
13	*Cut thread automatic*	F	2	9	9
14	*Aside part with two hands*	AS2H	2	42	50
	Sum (TMU)			**1255.8**	**1867.2**

Unit: TMU

Table 4. Analysis results of the operation process and sewing time to armhole seam at Tinh Loi Garment Co.,Ltd

No.	Description	CODE	Freq.	GSD	BKG
1	*Get part with two hands*	GP2H	2	33	35
2	*Put part to work table*	PPAL	2	10	10
3	*Adjust one part (top)*	AJPT	2	43	86
4	*Put to foot*	FOOT	2	38	46
5	*Sewing 20cm-curved-non visible seam*	S20MA	2	87	104.32
6	*Align two parts*	AM2P	2	61	122
7	*Sewing 12cm-curved-non visible seam*	S12MA	2	60.71	77.17
8	*Adjust parts by pushing*	APSH	2	24	48
9	*Sewing 33cm-curved-non visible seam*	S33MA	2	129.71	148.43
10	*Aside-Push away*	APSH	2	24	29
11	*Trim-Cut with scissors*	TCUT	2	50	50
12	*Put part to work table*	PPAL	1	10	10
	Sum (TMU)			**1130.8**	**1521.8**

Unit: TMU

Table 5. Comparison of Polo-Shirt sewing time following GSD with BKG and SAM (Standard Allowed Minute) at Hanosimex company.

No.	Assembly	Class	GSD	BKG	SAM	$k = \frac{BKG}{GSD}$	$k' = \frac{SAM}{GSD}$
1	Collar	*Closed collar without legs, woven neckband, body fabric neckline*	48.32	71.35	70.80	1.48	1.47
2	Placket	*Skewed placket and open edge*	62.50	86.50	85.40	1.38	1.37
3	Sleeve opening	*2-needle cover stitch*	24.80	37.70	37.50	1.52	1.51
4	Bottom	*2-needle cover stitch*	18.35	36.50	37.00	1.99	2.02
5	Seams	*Shoulder seam*	26.10	38.00	37.40	1.46	1.43
		Armhole seam	37.70	56.00	55.80	1.49	1.48
		Side seam and sleeve seam	50.60	76.40	76.20	1.51	1.51
	$\overline{k_{TB}}$, $\overline{k'_{TB}}$					**1.55**	**1.54**

Unit: seconds (s)

Table 6. Comparison of Polo-Shirt sewing time following GSD with BKG and SAM at Tinh Loi Garment Co., Ltd.

No.	Assembly	Class	GSD	BKG	SAM	$k = \frac{BKG}{GSD}$	$k' = \frac{SAM}{GSD}$
1	Collar	*Closed collar without legs, woven neckband, woven tape neckline*	76.5	113.1	99.0	1.48	1.29
		Closed collar without legs, woven neckband, body fabric neckline	80.2	110.3	100.8	1.38	1.26
2	Placket	*Skewed placket and fold edge*	129.3	164.1	150.2	1.27	1.16
		Skewed placket and fold edge, have buttonhole placket	141.6	192.0	181.5	1.36	1.28
3	Sleeve opening	*2-needle cover stitch sleeve opening*	27.4	37.9	36.0	1.38	1.31
		Sleeve cuff	50.0	63.3	61.2	1.27	1.22
4	Bottom	*2-needle cover stitch bottom*	26.9	39.1	28.8	1.45	1.07
		1-needle cover stitch bottom	40.3	63.2	44.4	1.57	1.10
5	Slit	*Close edge slit*	68.8	87.6	85.8	1.27	1.25
6	Seams	*Shoulder seam*	22.7	29.4	21.0	1.30	0.93
		Armhole seam	33.9	45.7	36.0	1.35	1.06
		Side seam and sleeve seam	37.5	48.9	45.0	1.30	1.20
	$\overline{k_{TB}}$, $\overline{k'_{TB}}$					**1.36**	**1.18**

Unit: seconds (s)

$$\bar{k} = \frac{1}{m}\sum_{j=1}^{m} k_j. \qquad (1)$$

In our study, we calculated the *k* and *k'* values, which are the ratios of SAM and GSD, and of BKH and GSD, respectively. After that, the $\overline{k_{TB}}$ and $\overline{k'_{TB}}$ values were determined, the values are the average of *k* and *k'*. From Table 5, comparing the values $\overline{k_{TB}}$ and $\overline{k'_{TB}}$, we see that these two values are approximately equal. The set of adjustment coefficients between the experimental value and the theoretically calculated value of sewing and preparation time is correct for traditional companies.

From Table 6, it can be seen that *k'* of Tinh Loi Garment Co., Ltd. is lower than k of the research group. Therefore, with modern production conditions (modern equipment, application of templates, highly skilled workers), the sewing stages time is shortened. This means that labor productivity is increased, product quality is uniform because the dependence on subjective factors of workers are reduced.

Final: In modern companies, the time value adjustment coefficient set from the study results is not suitable. When applied to this group, we have a new adjustment coefficient which is $\overline{k'_{TB}}$ (Table 6), called K_m:

$$K_m = \overline{k'_{TB}} = 1.18, \qquad (2)$$

$$SAM = 1.18 \sum Y_{GSD} \frac{60}{2000} \quad [s], \qquad (3)$$

where: 1 minute = 2000 TMU, 1 minute = 60s , 1s ≈ 33.33 TMU, $\sum Y_{GSD}$ (TMU) : Time to perform one workstation (including sewing and preparation time) calculated according to MTM and GSD. SAM_m [s]: Standard production time in K_m factor.

Proposing the operation process and sewing time on armhole seam for the two groups of companies

In experimental research, we have built a reasonable operation process and sewing time to detail assemblies, seams of P1, P2, T1, and T2. These are four representative products including detailed assemblies, typical seams. To build a complete database for all theoretical research products of the research team, we use the interpolation method to

Table 7. Table of the operation process and sewing time on armhole seam of traditional companies.

No.	Description	CODE	Freq.	GSD	BKG
1	*Pick up parts to table*	AS2H	1	42	50
2	*Unfold parts*	FUNF	1	23	44
3	*Position large panel to machine foot, add additional panel*	MAP2	2	69	83
4	*Grasp next panel*	MAP2	2	69	83
5	*Slide previous panel*	APSH	2	24	48
6	*Put to foot*	FOOT	2	38	46
7	*Sew to hold*	MS1A	2	17	17
8	*Align two parts*	AM2P	2	61	122
9	*Sewing 15cm – curved – non visible seam*	S15MA	2	52.1	87.35
10	*Align two parts*	AM2P	2	61	122
11	*Sewing 10cm – curved – non visible seam*	S10MA	2	40.4	70.38
12	*Turn shoulder seam*	FUNF	2	23	44
13	*Align two parts*	AM2P	2	61	122
14	*Sewing 5cm – curved – non visible seam*	S5MA	2	28.7	53.42
15	*Push assembly onto table*	APSH	2	24	29
16	*Align two parts*	AM2P	2	61	122
17	*Sewing 10cm – curved – non visible seam*	S10MA	2	40.4	70.38
18	*Align two parts*	AM2P	2	61	122
19	*Sewing 15cm – curved – non visible seam*	S15MA	2	52.1	87.35
20	*Aside-Push away*	APSH	2	24	29
21	*Trim – Cut with scissors*	TCUT	2	50	50
22	*Aside part with one hand*	AS1H	2	23	28
23	*Trim – Cut with scissors (additional)*	TCAT	2	25	25
24	*Obtain & pick up the sewn part*	AS2H	1	42	50
25	*Inspect the sewn part*	E	2	7	7
26	*Place sewn part back onto work table*	PPAL	1	10	10
	Sum (TMU)			**1940.4**	**3089.76**
	Actual production time according to BKG (s)				**92.69**

Unit: TMU

Table 8. Table of the operation process and sewing time on armhole seam of modern companies.

No.	Description	CODE	Freq.	GSD
1	*Pick up parts to table*	AS2H	1	42
2	*Unfold parts*	FUNF	1	23
3	*Position large panel to machine foot, add additional panel*	MAP2	2	69
4	*Grasp next panel*	MAP2	2	69
5	*Slide previous panel*	APSH	2	24
6	*Put to foot*	FOOT	2	38
7	*Sew to hold*	MS1A	2	17
8	*Align two parts*	AM2P	2	61
9	*Sewing 15cm – curved – non visible seam*	S15MA	2	52.1
10	*Align two parts*	AM2P	2	61
11	*Sewing 10cm – curved – non visible seam*	S10MA	2	40.4
12	*Turn shoulder seam*	FUNF	2	23
13	*Align two parts*	AM2P	2	61
14	*Sewing 5cm – curved – non visible seam*	S5MA	2	28.7
15	*Push assembly onto table*	APSH	2	24
16	*Align two parts*	AM2P	2	61
17	*Sewing 10cm – curved – non visible seam*	S10MA	2	40.4
18	*Align two parts*	AM2P	2	61
19	*Sewing 15cm – curved – non visible seam*	S15MA	2	52.1
20	*Aside-Push away*	APSH	2	24
21	*Trim – Cut with scissors*	TCUT	2	50
22	*Aside part with one hand*	AS1H	2	23
23	*Trim – Cut with scissors (additional)*	TCAT	2	25
24	*Obtain & pick up the sewn part*	AS2H	1	42
25	*Inspect the sewn part*	E	2	7
26	*Place sewn part back onto work table*	PPAL	1	10
ΣY_{GSD} (TMU)				1940.4
SAM_m (s)				68.69

Unit: TMU

Table 9. The sewing time results of sleeve opening by the interpolation method.

No.	Assembly	Traditional company (BKG)	Modern company (GSD) K_m=1.18
1	*Sleeve have cuff facing fold in*	76.2 s	58.8 s
2	*Sleeve have cuff facing*	109.2 s	79.9 s
3	*Sleeve cuff*	70.2 s	51 s

calculate the *Km* coefficient for two groups of companies, performed for all assemblies, the seams are shown in Table 1. Due to the limited scope of the article, we only present the results of the operation process and sewing time to the armhole seam and sleeve opening. They give in Tables 7, 8, 9.

CONCLUSION

The results have built a reasonable data set on the operation process, the time to perform the sewing operation of Polo-Shirt and T-Shirt products, contributing to a more standardized process of applying GSD predetermined time system to the reality of production in enterprises, minimizing errors that may be caused by influencing factors. The database has been built systematically and standardized to ensure the diversity, abundance, and universality of all product technology structure options in line with reality in garment enterprises. The database is applied in sewing operation analysis software built by the research team - this is an application-oriented research product that will transfer technology to garment enterprises producing knitwear, supporting the improvement and rationalization of labor methods, building standard processes and optimal technological processes, maximizing existing production conditions in order to improve labor productivity and economic efficiency, creating a premise to apply digital technology to create a breakthrough in Vietnam's garment industry. The authors have built a systematized and standardized database on the operation process and sewing time to perform the reasonable operation of two knitted products. In the future, the team will continue to research and expand with other items to diversify the database on the operation process and the sewing operation time.

REFERENCES

1. Rahman, H., Roy, P K., Karim, R. et al.: Effective way to estimate the standard minute value (SMV) of a t-shirt by work study, European Scientific Journal 10(30), 2014, pp. 196-203.
2. Thao, P.T., Long, T.V., Huong, D.M., et al.: Apply genetic algorithm to solve assembly line balancing problem, In: Proceedings the 2st National Scientific Conference on Textile, Apparel and Leather Engineering. Hanoi University of Science and Technology Publisher, 2021, pp. 254-260.
3. Thao, P.T., Anh, L.T.M., Phan, D.N., et al.: Researching the optimal method of balancing the sewing line with T-shirt product in the garment industry in Vietnam, ECS Transactions 107(1), 2022, pp. 7869-7887. https://doi.org/10.1149/10701.7869ecst
4. Dinh, M.H., Nguyen, V.D., Truong, V.L., et al.: Cycle time enhancement by simulated annealing for a practical assembly line balancing problem, Informatica, 44(2), 2020, pp. 127–138. https://doi.org/10.31449/inf.v44i2.3083
5. Thao, P.T. and Huong, D.M.: Research on apply of polo-shirt assembly line balancing methods in Vietnam garment industry, In: Proceedings the 2st National Scientific Conference on Textile, Apparel and Leather Engineering. Hanoi University of Science and Technology Publisher, 2021, pp. 307-318.
6. Huong, D.M., Long, T.V., Thuan, D.P., et al.: Application of exhaustive search for optimization Assembly Line Balancing in Garment Industry, Journal of Science & Technology Technical Universities 141, 2020, pp. 34-41.
7. Alam, F.B. and Hasan, M.M.: Analysis on SMV to increase productivity in sewing section: a case study on T-shirt manufacturing in Bangladesh, International Journal of Research in Engineering and Science, 6(8), 2018, pp. 18-24.

AIMS AND SCOPES

"Vlakna a Textil" is a peer-reviewed scientific journal serving the fields of fibers, textile structures and fiber-based products including research, production, processing, and applications.

The birth of this journal is connected with three institutions, Research Institute for Man-Made Fibers, Svit (VÚCHV), Research Institute of Chemistry of Textiles (VÚTCH) in Žilina and Department of Fibers and Textiles at the Faculty of Chemical Technology, Slovak Technical University in Bratislava, having a joint intention to provide, utilize and deposit results obtained through the research, development and production activities dealing with the aforementioned scopes. „Vlákna a Textil" journal has been launched as a consequence of a joing of existing magazines „Chemické vládkna" (VÚCHV) and „Textil a chémia" (VÚTCH). Their tradition should provide a good framework for the new journal with the main aim to create a closer link between the basic element of the product - fibre and its fabric - textile.

Since its founding in 1994, the journal introduces new concepts, innovative technologies and better understanding of textile materials (physics and chemistry of fiber forming polymers), processes (technological, chemical and finishing), garment technology and its evaluation (analysis, testing and quality control) including non-traditional applications, such as technical textiles, composites, smart textiles or garment, and nano applications among others. The journal publishes original research papers and reviews. Original papers should present a significant advance in the understanding or application of materials and/or textile structures made of them.

VLÁKNA A TEXTIL
Volume 30, Issue 4, October 2023

CONTENT